Czech Technical University in Prague
Faculty of Nuclear Sciences and Physical Engineering

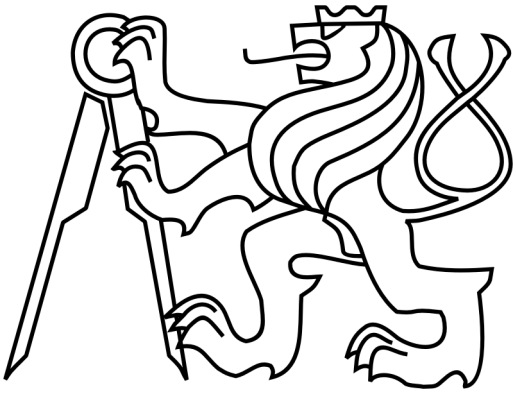

DISSERTATION THESIS

Use of diffractive optical elements in high power fiber lasers

Prague 2021 Ing.Martin Vaněk

Bibliografický záznam

Autor	Ing. Martin Vaněk České vysoké učení technické v Praze Fakulta jaderná a fyzikálně inženýrská Katedra fyzikální elektroniky
Název práce	Užití difraktivních optických elementů ve vysokovýkonných vláknových laserech
Studijní program	Doktorské studium
Studijní obor	Fyzikální inženýrství
Školitel	Doc. Ing. Ivan Richter Dr. České vysoké učení technické v Praze Fakulta jaderná a fyzikálně inženýrská Katedra fyzikální elektroniky
Školitel specialista	Dr. Ing. Pavel Honzátko Akademie věd České republiky Ústav fotoniky a elektroniky Vláknové lasery a nelineární optika
Akademický rok	2020/2021
Počet stran	66
Klíčová slova	difrakční mřížky, fokusovaný iontový svazek, mikroobrábění fokusovaným iontovým svazkem, numerické modelování, vysokovýkonové vláknové lasery, anti-reflexní struktury, vysoce-reflexní struktury, polarizační závislost, fotonické struktury

Bibliographic Entry

Author	Ing. Martin Vaněk Czech Technical University in Prague Faculty of Nuclear Sciences and Physical Engineering Department of Physical Electronics
Title of Dissertations	Use of diffractive optical elements in high power fiber lasers
Degree Programme	Doctoral Degree Study
Field of study	Physical Engineering
Supervisor	Doc. Ing. Ivan Richter Dr. Czech Technical University in Prague Faculty of Nuclear Sciences and Physical Engineering Department of Physical Electronics
Supervisor specialist	Dr. Ing. Pavel Honzátko Czech Academy of Sciences Institute of Photonics and Electronics Fiber Lasers and Non-linear Optics Group
Academic Year	2020/2021
Number of Pages	66
Keywords	diffraction grating, focused ion beam, focused ion beam micro-machining, numerical modeling, high power fiber laser, anti-reflection structure, high reflectivity structure, polarization sensitivity, photonic structure

Acknowledgment

First of all I would like to thank my supervisors Doc. Ing. Ivan Richter Dr. and Dr. Ing. Pavel Honzátko. Their support and guidance were invaluable and I am grateful for all time and energy they spent with me.

Thanks also to the whole Fiber Lasers and Nonlinear Optics team from Institute of Photonics and Electronics and also to other colleagues for their help, feedback and advice during my studies.

Thank you to Ing. Pavel Kwiecien PhD for providing me the aRCWA simulation tool. Also thanks to the whole research group and to the developer community for the MEEP simulation software.

I would like to thank for the support from Czech Science Foundation - GAP15-07908S, SGS Czech Technical University (161-1611311D000, 161-1611617D000 and 161-1611916D000).

And finally, I am incredible grateful to my family for their support.

Martin Vaněk

Team leader declaration

I, Dr. Ing. Pavel Honzátko as a team leader of the Fiber Lasers and Nonlinear Optics group from Institute of Photonics and Electronics, hereby declare that Ing. Martin Vaněk can use the research results of the team connected with his dissertation research in his thesis. The author made simulations by the aRCWA tool developed at Czech Technical University by Ing. Pavel Kwiecien PhD. Dr. Ing. Pavel Honzátko performed FDTD simulations in MEEP tool and contributed by principal ideas on high reflectance structures. Prof. Ing. Jiří Čtyroký, DrSc. performed the 2D/3D simulations using his own UFE FMM tool and contributed by principal ideas on antireflection structures. Development of technological processes, preparation of diffractive structures, their characterizations and measurements in laser setups were performed by the author of the thesis.

Dr. Ing. Pavel Honzátko

Abstrakt

Tato práce prezentuje vývoj a testování difrakčních elementů vyrobených na čele optického vlákna. Nejprve byly struktury studovány pomocí numerických simulací. Použité metody jsou RCWA, aRCWA, FDTD a FMM. Byly provedeny 1D, 2D i 3D simulace struktur a výsledky metod byly porovnány. Struktury byly optimalizované s ohledem na jejich použití a to antireflexní, nízkoreflexní polarizačně selektivní a vysocereflexní polarizačně selektivní struktury. Chování vybraných struktur bylo zkoumáno kolem optimalizovaných parametrů pro hlubší porozumění vyskytujících se jevů.

Fokusovaný iontový svazek je použit pro výrobu optimalizovaných difraktivních struktur na čele optického vlákna. Před procesem výroby pomocí fokusovaného iontového svazku je třeba provést přípravu optických vláken pro tento proces, což zahrnuje zalomení vlákna, přípravu čela pro zápis difraktivní struktury, respektive depozici vysokoindexové oxidické vrstvy případně vodivé vrstvy pro potlačení nabíjení. Pro zmíněné akce byly vyvinuty a optimalizovány pracovní a výrobní procesy. Optimalizace a stabilita procesu výroby pomocí fokusovaného iontového svazku je řešena a diskutována.

Vyrobené struktury byly testovány vzhledem k jejich požadovaným vlatnostem v optickém měřícím setupu nebo přímo ve výkonovém vláknovém laseru. Antireflexní struktury byly testovány v setupu vyvinutém, optimalizovaném a automatizovaném pro toto specifické měření. Byly použity komponenty z telekomunikační oblasti pro jejich dobrou dostupnost. Nízkoreflexní polarizačně selektivní a vysocereflexní polarizačně selektivní struktury byly testovány přímo ve vysokovýkonném thuliovém vláknovém laseru, který byl předem charakterizován, aby mohly být srovnány vlastnosti.

Výsledky uvedené v disertační práci byly průběžně prezentovány ve věděckých časopisech a na konferencích. Hlavními výstupy této práce jsou: numerické modelování a porozumění chování difraktivních struktur na čele vlákna, optimalizace procesu výroby těchto struktur pomocí fokusovaného iontového svazku a jejich charakterizace.

Abstract

The work presents progress in the development and testing of diffractive elements inscribed onto an optical fiber facet. The structures were investigated using numerical modeling tools, namely: RCWA, aRCWA, FDTD and FMM. 1D, 2D and 3D simulations of the fiber facet structures were performed and their results were compared together. Anti-reflection, low reflection polarization sensitive and high reflection polarization sensitive structures were optimized using numerical modeling tools. Behaviours of the selected structures were investigated by varying their parameters around their optimized values. This investigation was performed to understand better the phenomena present.

A focused ion beam was used to directly inscribe the designed diffractive structure onto an optical fiber facet. There are additional steps before the direct inscription of the diffractive structures in the fabrication process, including preparing the fiber facet for the inscription or for the sputtering of an oxide layer with high refractive index or an anti-charging conductive layer. Fabrication processes and preparatory procedures were developed for these actions. Optimization and stability of the focused ion beam process were investigated and discussed.

The fabricated structures were tested in measurement setups or in high power lasers accordingly to their purpose. Anti-reflection structures were tested in the optical measurement setup developed, optimized and automatized for this application. Telecom parts were used due to their availability. Low reflection polarization sensitive and high reflection polarization sensitive structures were tested directly in the high power thulium fiber laser setup. The setup had known parameters and therefore performance was compared.

The results stated in the dissertation thesis were presented continuously in academic journals and at conferences. Main results of this research are: fiber facet diffractive elements numerical simulations and understanding of their behaviour, optimization and development of the prefabrication and fabrication procedures using focused ion beam technique and characterization of fabricated structures.

Contents

Introduction

Photonics is currently being investigated by many scientists and research groups around the world. Not only purely optics groups but also biophotonics groups, medical groups, and sensor groups. Research is focused on structures with dimensions comparable to or smaller than the wavelength of the light used. We now have the opportunity to develop and also fabricate these structures by using state of the art technology. It is possible to fabricate more complex structures like 3D photonic crystals [1, 2].

Photonic structures can be used to achieve various results. We will write about controlling the polarization dependent reflectance and transmittance. The AR structures are widely investigated for use in laser optics and windows [3], to understand the natural moth eye structures [4] or to use random processes to design and produce them [5]. The wavefront output can be manipulated by phase masks to achieve controlled patterns of phase, amplitude and intensity [6]. Fresnel lenses can be inscribed onto the fiber facet to increase the efficiency of the coupling into the fiber [7]. In recent years, optical tweezers have been receiving more attention. Optical elements called axicons are used for trapping particles by a beam of light. An axicon can also be fabricated onto the optical fiber facet [8]. Sensoring applications also need to be mentioned. Optical fiber sensors can be used in dangerous environments. An example for use in daily life is a CO_2 fiber-tip sensor [9].

We will focus on photonic structures for use in high power fiber lasers. A high power fiber laser can be used for various industrial applications, such as laser cutting [10], welding [11], engraving and marking [12]. Photonic structures can be polarization sensitive and therefore are suitable for use in lasers with polarized output beams. Polarized high power laser beams are essential for generating second harmonics [13], and pumping optical parametric oscillators (OPOs) [14, 15]. The brightness of a fiber laser can be scaled by polarization multiplexing [16].

Fiber lasers can be built in various configurations. We will introduce the Fabry-Perot configuration, the ring configuration, and the sigma laser configuration. A Fabry-Perot fiber laser configuration consists of an active fiber, which can be straight or coiled. Coiling the active fiber can introduce polarization dependent losses and polarize the output of the laser. Wavelength division multiplexer (WDM) is used to couple the pump signal from laser diode (LD) to the resonator. There are Bragg gratings at both ends of a Fabry-Perot fiber laser. The cladding mode stripper (CMS) can be introduced into the setup. A polymer UV-glue with refractive index higher than the cladding is used to seal the splice between the active fiber and a low reflecting fiber Bragg grating (LR-FBG). It decouples the unabsored pump signal from the cladding. A highly reflective fiber Bragg grating (HR-FBG) is at one end

and at second end is the LR-FBG, with a reflectance of 5%–10% to achieve steep slope efficiency. This reflectance is comparable with a cleaved fiber facet (reflectance approximately 3.5%) which is also used. The Fabry-Perot fiber laser configuration is shown in Figure 1.

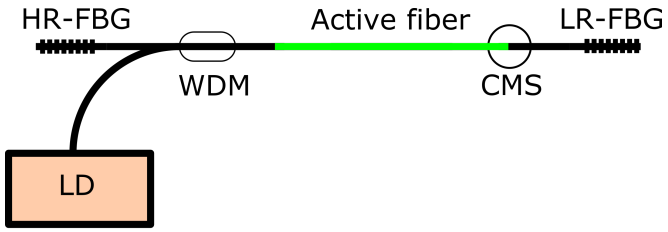

Figure 1: Fabry-Perot fiber laser configuration. Highly reflective fiber Bragg grating (HR-FBG), low reflecting fiber Bragg grating (LR-FBG), wavelength division multiplexer (WDM), cladding mode stripper (CMS), laser diode (LD) and active fiber are used to build the Fabry-Perot laser.

The fiber ring laser configuration is in the shape of a circle, as its name suggests. An active fiber, which is part of the ring, is connected to one of the three ports of the fiber circulator. An HR-FBG is connected to the second circulator port. A polarization maintaining fiber tap-isolator wavelength division multiplexer (PMTIWDM) is connected to the third port. Its input port is connected to the active fiber. A PMTIWDM is a hybrid element which determines the direction of the light in the ring resonator, couples the pump light into the resonator, and also decouples the signal from the resonator. The fiber ring resonator configuration is shown in Figure 2.

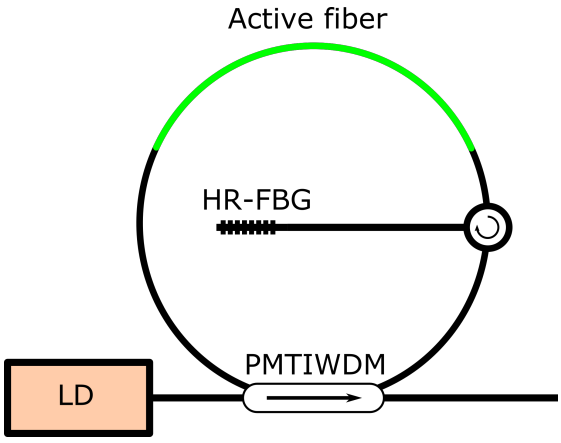

Figure 2: Ring fiber laser configuration. Highly reflective fiber Bragg grating (HR-FBG), polarization maintaining fiber tap-isolator wavelength division multiplexer (PMTIWDM), laser diode (LD), circulator and active fiber are used to build the fiber ring laser.

The sigma laser configuration derives its name from the Greek letter σ, which is similar to its schematics. A sigma laser mixes PM and non-PM components in one

laser setup. We can distinguish the PM branch which consist of a polarization beam splitter (PBS), polarization maintaining tap isolator (PMTI), which also acts as the output of the laser and connection with the fiber ring. The PM branch is connected to the two ports of the PBS. The non-PM branch is connected to the third port of the PBS. The non-PM branch consists of the active fiber, a WDM for coupling the pump signal to the active fiber, and a Faraday mirror (FM). The sigma laser configuration is shown in Figure 3.

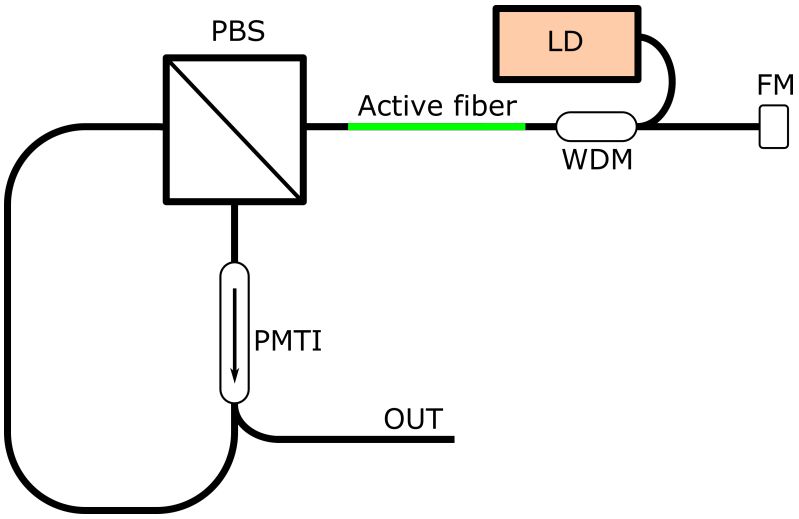

Figure 3: Sigma fiber laser configuration. Polarization beam splitter (PBS) and polarization maintaining tap isolator (PMTI) form the PM branch of the sigma laser. Active fiber, wavelength division multiplexer (WDM), laser diode (LD) and Faraday mirror (FM) form the non-PM branch of the sigma laser.

A polarized output of the fiber laser can be obtained using either a bulk [16] or a fiber polarizer [17], a polarizing isolator, or other hybrid elements which are included into the low power fiber laser resonator [18, 19]. These low power lasers are made of polarization maintaining (PM) fibers. The σ-configuration approach can also be used to mix both PM and non-PM components in one laser setup [20]. It needs to be said that any passive intra-cavity element influences negatively the laser parameters, such as the threshold, slope efficiency and reliability.

We will present structures fabricated directly onto the cleaved fiber facet [21, 22]. This is the rising technology in the fiber optics area. There are many state of the art ways to fabricate fiber facet photonic structures. Two photon polymerization 3D printing [23, 24, 25], electron lithography [26], photo-lithography [27], interference lithography [28], nano-imprint technology [29, 30], direct femtosecond laser inscription [31] and direct focused ion beam (FIB) [7] milling have been demonstrated to be tools for fiber facet patterning. However, many of these techniques are not suitable for high power applications. The best technology to nano-pattern a structure onto the fiber facet for high power applications is etching or milling the structure directly. We will present the FIB direct milling of the structure onto the cleaved fiber facet.

Aims of the dissertation

In this PhD thesis we present our progress and results regarding diffraction fiber facet structures. This work was carried out in the Fiber Lasers and Nonlinear Optics Group in the Institute of Photonics and Electronics of the Czech Academy of Sciences. My PhD studies were carried out in the Department of Physical Electronics of the Faculty of Nuclear Sciences and Physical Engineering of the Czech Technical University in Prague. The Fiber Lasers and Nonlinear Optics team carries out research in optical fiber technology and materials science, focused on fiber lasers and amplifiers, optical fiber components, nonlinear optics, optical waveguide theory, and numerical modeling. Its research activities are focused on the high-power thulium- and holmium-doped fiber lasers for industrial, defense, and metrological applications. We want to improve the all-fiber design of high power fiber lasers. This design should have no external elements outside the optical fiber, so as to be suitable for industrial implementation.

The aim of this thesis is the development of new techniques of integrating various components into all-fiber setups. All-fiber lasers eliminate the need for time-consuming alignment, and offer a more compact layout. The decreased complexity of the laser setup means lower intracavity loss and higher reliability. HR-FBG is a widely used diffraction structure. We will present the design, fabrication and testing of a diffraction structure inscribed directly onto the optical fiber facet. Design phase included analysis of the structures, their numerical modeling and parameters optimization to fulfill desired properties. Fabrication process is described by two phases. Preparatory phase of the fibers and the fabrication itself including optimization procedures. Testing of the fabricated structures is performed in the measurement setups designed specifically for this purpose or in the high power fiber lasers.

Organisation of the dissertation

In this Introduction, the idea of a fiber facet diffraction structure has been introduced. The approach chosen and our motivation for performing this research in the field of diffraction structures for high power lasers has been explained. The aims of the work have been explained, and at the end, the organisation of this work will be presented.

The main part of the thesis is divided into four chapters. Chapter 1 presents the numerical modeling of the fiber facet diffraction structure. The basics of the methods used to compute the behavior of the fiber facet diffraction structure will be introduced. The RCWA, aRCWA, FDTD amd FMM methods will be introduced. The structures which have been designed and optimized will be described at the end of the chapter. The anti-reflection, low reflectance polarization sensitive and high reflectance polarization sensitive diffraction structures will be introduced and their dimensions optimized.

Chapter 2 introduces the prefabrication procedures needed to prepare the optical fibers for the fabrication of the fiber facet structures. A fiber preparation protocol will be presented for the sputtering. The process of sputtering for obtaining a high

refractive index oxide layers will be described.

A process of fiber facet microstructuring using a FIB will be described in Chapter 3. Scanning electron microscopy will be introduced as a necessary tool to investigate the fabricated structures. Sample charging mitigation will be discussed and the investigated ways will be described. The optimization procedure needed to obtain correctly FIB operation will be introduced. Fabrication processes will be described for the anti-reflection gratings, low reflection polarization sensitive gratings, high reflection polarization sensitive gratings and 2D structures.

The optical properties of different fiber facet diffraction gratings will be presented in Chapter 4. The fabricated fiber facet gratings were tested according to their purpose. The anti-reflection gratings were optically tested, measuring the reflectance and transmittance. The low reflection polarization sensitive gratings and high reflection polarization sensitive gratings were tested in the thulium doped fiber laser.

The thesis results are discussed and summarized in the Conclusion.

Chapter 1

Numerical modeling

In this chapter we present the numerical modelling tools used for computing the optical properties of the structures considered. We used a rigorous coupled wave analysis (RCWA) for fast computing and insight. Then we used the modelling tools for an aperiodic rigorous coupled wave analysis (aRCWA) [32] and finite difference time domain (FDTD) [33] for modeling the structure and its behaviour. Note that RCWA is also referred to as Fourier modal method (FMM) in the literature. The in house implementation of the aRCWA for 2D and 3D structures is called UFE FMM [34]. We compared the computational methods used.

By nano-patterning the fiber facet we can achieve different behaviours of the light with simple 1D diffraction grating structures. Polarization insensitive anti-reflection (AR) structures, polarization sensitive low reflecting mirror structures, and also polarization sensitive high reflecting mirror structures can be designed and fabricated. The light propagates through the core of the optical fiber to the cleaved fiber facet where the photonic structure is fabricated. When we used a 1D diffraction grating, the grating grooves are parallel to the slow axis of the PM-fiber. For the non-PM fibers, the orientation of the grating can be random. A schematic drawing of the used smf28 and Nufern PLMA-GDF-25/400-10FA (FUD 3716) fibers is shown in Figure 1.1. [35, 36] These fibers were selected to be used in the experiments.

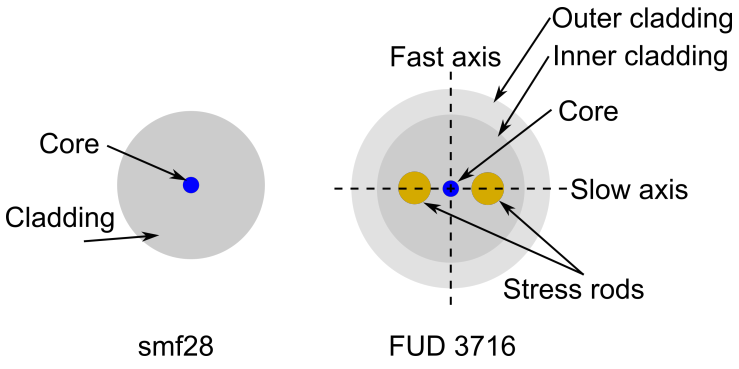

Figure 1.1: Schematic geometry of the fibers used in simulations.

1.1 Numerical modeling tools

In this section we will introduce the RCWA, aRCWA, FDTD and UFE FMM numerical modeling tools used to compute and design the photonic structures of our interest.

1.1.1 Rigorous coupled wave analysis

Rigorous coupled-wave analysis, also referred to in the literature as the Fourier modal method, is a semi-analytical method for computing the electro-magnetic field in photonic structures. Typically the structures are considered infinite, periodic and dielectric. It is a Fourier-space method, which means that the computed electro-magnetic fields are represented as sums of spatial harmonics.

The main idea behind the RCWA is Floquet's theorem, which asserts that the solution to a periodic differential equation can be expanded with Floquet functions or Bloch waves. The structure is divided into the layers in the z-direction, as shown in Figure 1.2. This transforms the wave equation into a set of ordinary differential equations, which can be solved as an eigenvalue problem. The spatial harmonics and their configuration in each layer are described by an eigenvector. This approach describes the behaviour of the electro-magnetic field in the structure in terms of a complex propagation constant and the coupling between the modes. The solution is obtained by applying the boundary conditions and matching the tangential fields at the interfaces of the layers.

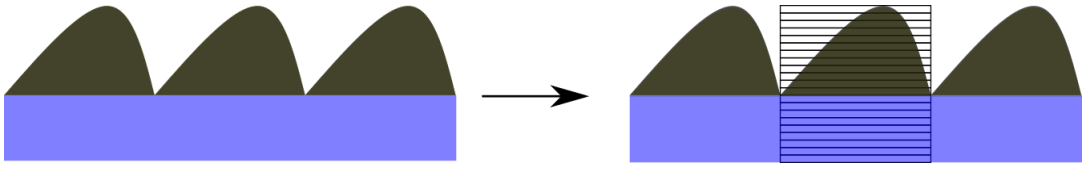

Figure 1.2: Schematic figure of RCWA approach of slicing periodic structure into layers where the electro-magnetic field is computed.

The RCWA is best suited to compute and analyse structures which are layered with minimal volumetric complexity. More complex structures need a stair-case approximation of their geometry and this becomes more computationally intensive because a complete set of eigenmodes have to be computed for each layer. Structures which are described well by a few terms of the Fourier series are fast and easily computed by RCWA. Note that this is for structures with low and medium refractive index contrast. For structures with a sharp index contrast or structures with metals, many Fourier terms are needed to accurately describe the electro-magnetic field. This results in slow computing and very high requirements for the computer memory.

1.1.2 Aperiodic rigorous coupled wave analysis

The aperiodic-RCWA computes the propagation of the electro-magnetic field in wave-guide like structures. It forces RCWA to compute non-periodic structures. Absorbing boundary layers were introduced into the periodic structure to imitate a

non-periodic structure. What are mostly used are perfectly matched layers (PML), which let all the electro-magnetic field pass through them with no reflection. In aRCWA, these layers are also absorbing, due to the forced periodicity. Figure 1.3 shows the implementation of absorbing layer to illustrate the change from a periodic structure to a non-periodic structure.

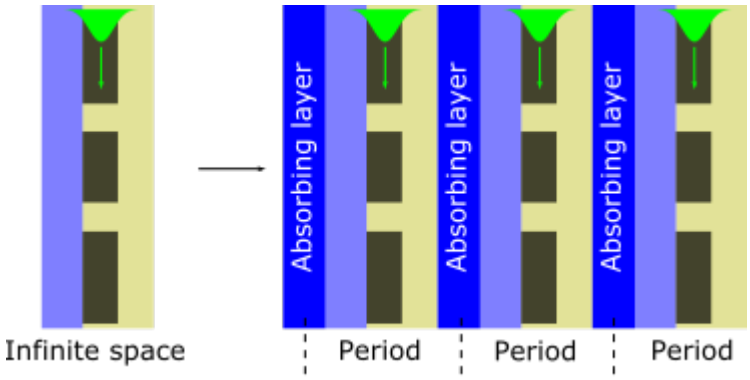

Figure 1.3: The introduction of aRCWA absorbing layers to force RCWA to compute non-periodic wave-guide like structures.

In Figure 1.3 the artificial periodization of the 2D structure is shown. We will mostly use this approach for computing the fiber facets' structures. Later we will show that the 2D computation results are in good agreement with those from 3D computational methods. We have used two implementations of the aRCWA. One was developed by Kwiecien [32], the other was developed in house by Čtyroký [34].

1.1.3 Finite difference time domain

Today, the use of FDTD electromagnetic calculations is very broad, covering the range from the ultra low-frequency geophysics of the Earth-ionosphere through microwaves, such as antennas and wireless communication, to visible light and nearby area covering photonic crystals, nanoplasmonics, solitons and the whole problem of light guiding in structures.

It can be seen from Maxwell's equations that the change in the electric field over time is dependent on the change in the magnetic field over space. This result is the main FDTD time stepping relation: at any point in space, the electric field at that time is dependent on the stored value of the electric field and the change in the local distribution of the magnetic field in space. The magnetic field is time dependent in a similar way. By solving for the electric and magnetic fields we can obtain the evolution over time of the wave propagating through the grid stored in memory. The change in the field across space is called the curl. The FDTD method can be used in 1D, 2D, and even in 3D problems. When we consider more dimensions, the numerical calculation of the curl become more complicated and challenging.

To solve the problem we need to solve simultaneous equations. Yee introduced a lattice to discretize Maxwell's equations [37]. In Yee's lattice the electric and magnetic field are computed in rectangular cells. Each electrical field vector is located midway between pair of the magnetic field vectors, and conversely. The

drawback of this method is that some simulations require thousands of time steps for the result. Yee's method is very robust and is widely used nowadays in FDTD simulation software. The area where the electric and magnetic fields are computed cannot be infinite due to the requirements on the computing power and memory. PMLs are used as borders of the area where the electro-magnetic field is computed.

FDTD is widely used nowadays to compute more and more complex structures. There are many commercially available tools with FDTD implemented. MEEP [33] was used to compute the diffraction fiber facet structures.

1.2 1D fiber facet structures

In this section we investigate diffraction gratings with a 1D rectangular shape. We aim to understand the behaviour of the diffraction from sub-wavelength gratings to gratings with $\pm 1^{st}$ diffraction orders. The behaviour of the gratings was investigated in order to determine the reflectance with the diffraction orders, and polarization properties of the reflected and transmitted light. The effect of the excitation of the leaky mode by the guided fiber mode was studied. We are looking for structures with light reflected or transmitted to one diffraction order. Due to the geometry of the optical fiber facet, the 0th diffraction order was mainly investigated. The light diffracted to the other orders was considered as a loss.

Light diffraction is limited to zero order in sub-wavelength diffraction gratings. The optical properties of such gratings can be explained by the effective-medium theory [38]. A sub-wavelength grating behaves roughly as a homogeneous birefringent layer. Its reflectivity varies periodically with the thickness of the grating and depends on the polarization of the incident light. In the effective-medium model for an unstructured fiber facet, the maximum reflectivity can not exceed the value given by Fresnel's equations (approximately 3.5% for fused silica material).

Gratings with longer periods allow achieving zeroth order diffraction efficiency beyond the Fresnel reflection limit, at the expense of introducing losses due to the diffraction into higher reflected orders. The reflection coefficients for both polarization and 0th order are shown in Figures 1.4 and 1.5.

The structures shown in Figures 1.6 and 1.7 show the geometry of the optical fiber facet diffraction gratings inscribed directly on the optical fiber facet and on the dielectric layer sputtered onto the fiber facet, respectively. This structure is an approximation of the 3D structure of the optical fiber. It is sliced in the direction of the propagation of the light and perpendicular to the grooves of the grating. At first we ran a simulation only with the bare fiber and grating on the the cleaved fiber facet. We used the parameters listed in Table 1.1. The zeroth order reflectance for the TE and TM polarized wave is shown in Figures 1.4 and 1.5, respectively. From these results it is clear that we can fabricate an anti-reflection structure and low reflection structure which can be polarization sensitive [21].

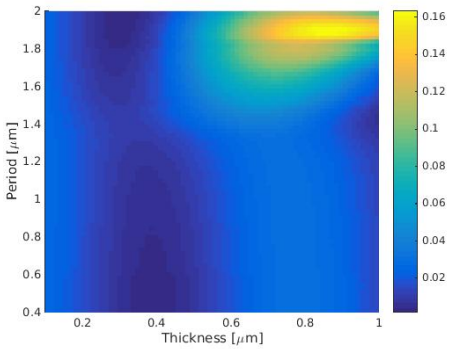

Figure 1.4: The reflectivity of the fiber facet grating obtained by aR-CWA for fill-factor 0.6, wavelength 2040 nm, 0 deg incidence and TE polarization.

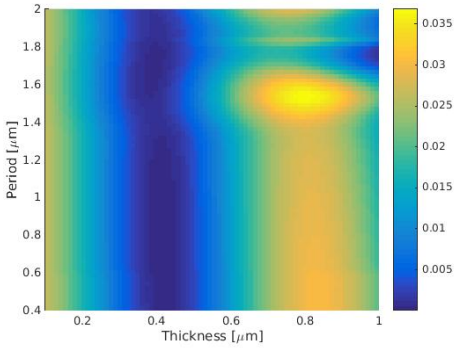

Figure 1.5: The reflectivity of the fiber facet grating obtained by aR-CWA for fill-factor 0.6, wavelength 2040 nm, 0 deg incidence and TM polarization.

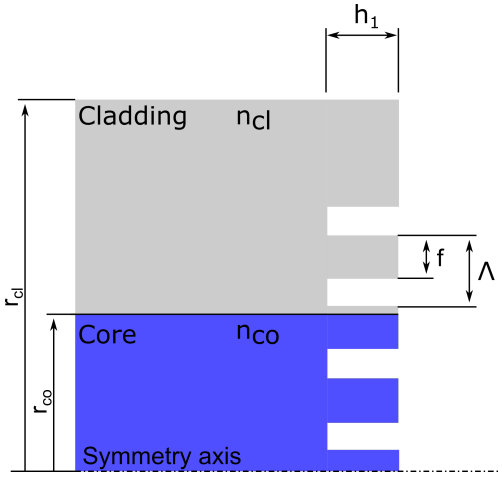

Figure 1.6: Cross-sectional 2D structure of fiber facet grating. Parameters: core diamater (r_{co}), cladding diameter (r_{cl}), core refractive index (n_{co}), cladding refractive index (n_{cl}), grating groove thickness (h_1), grating period (Λ) and grating fill factor (f).

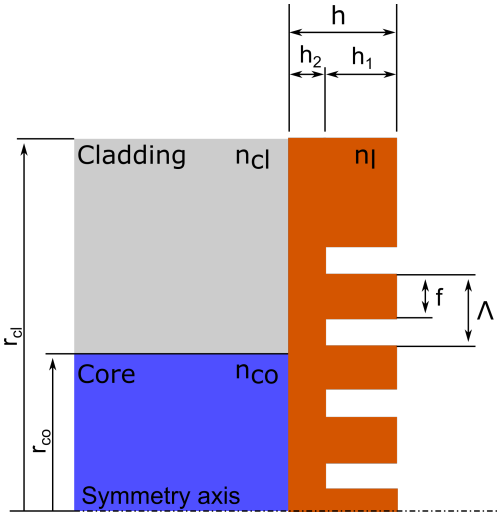

Figure 1.7: Cross-sectional 2D structure of fiber facet grating with high refractive index layer. Parameters: core diamater (r_{co}), cladding diameter (r_{cl}), core refractive index (n_{co}), cladding refractive index (n_{cl}), layer refractive index (n_l), layer thickness (h), grating groove thickness (h_1), wave-guide layer thickness (h_2), grating period (Λ) and grating fill factor (f).

Table 1.1: Parameters of the simulation used for initial insight into the behaviour of the fiber facet grating. Schematic drawing of the structure is shown in Figure 1.6.

Fiber parameters	**Values**
$\mathbf{h_1}$ [μm]	0.1 - 1
$\mathbf{\Lambda}$ [μm]	0.4 - 2
Fill factor	0.6
$\mathbf{r_{co}}$ [μm]	4.5
$\mathbf{r_{cl}}$ [μm]	15
Fiber length [μm]	2
$\mathbf{n_{air}}$	1
$\mathbf{n_{co}}$	1.4428
$\mathbf{n_{cl}}$	1.44
$\boldsymbol{\lambda}$ [μm]	2.04

The higher value of the reflectance for TE polarization is approximately 20%, which is not suitable for the replacement of the high reflecting fiber Bragg gratings used in fiber lasers. This structure also has the drawback that it is not sub-wavelength, which means that there are higher diffraction orders in reflection present. Reflection to the 1^{st} and -1^{st} diffraction order are considered losses in our case. The presence of the 1^{st} and -1^{st} reflected orders is clearly visible from Figures 1.14 and 1.15. These orders are not guided in the optical fiber core but they propagate in the cladding. When we seek for higher reflection and sub-wavelength design of the structure we need to implement a layer with a refractive index higher than 1.7 on top of the cleaved fiber facet [39].

1.2.1 Anti-reflection structures

Anti-reflection coatings change the surface reflection below the standard theoretical values obtained from the Fresnel equations. The simplest one-layer coatings work on specific wavelength. For various uses, also a wider bandwidth is needed. A wider bandwidth of the anti-reflection coating can be achieved by more complex structures.

The idea of an anti-reflection structure is mainly based on the effective-medium theory and the known mechanisms of making anti-reflection coatings, such as refractive index matching and one-layer interference. We focused on a 1D periodic anti-reflection grating but in the literature there can be also be found random structures and moth-eye structures.

As was mentioned above, the numerical simulations of the structure shown in the Figure 1.6 allow us to design an anti-reflection diffraction grating on the cleaved fiber facet. In the experiments we planned to use smf28 and PLMA 25/400 fiber from Nufern. That is why we used the geometry and materials of these fibers in the simulations. The parameters of the fibers used in the simulations are listed in Table 1.2. The optimized parameters of the AR structure for both fibers are listed in Table 1.3. Also the reflectivity obtained from the aRCWA and MEEP simulations is listed. We can see that the results are close and therefore we can be confident about these results.

Table 1.2: Parameters of the PLMA-GDF-25/400-10FA (FUD3716) fiber used in the simulation.

Fiber parameters	**smf28**	**FUD 3716**
$\mathbf{r_{co}}$ [μm]	4.5	12.5
$\mathbf{r_{cl}}$ [μm]	10	40
Fiber length [μm]	2	
$\mathbf{n_{air}}$	1	
$\mathbf{n_{co}}$	1.4428	
$\mathbf{n_{cl}}$	1.44	

Table 1.3: Optimized parameters of the anti-reflection grating.

Fiber	$\boldsymbol{\lambda}$ [nm]	$\boldsymbol{\Lambda}$ [nm]	$\mathbf{h_1}$ [nm]	**Fill factor**	$\mathbf{R_0}$ **aRCWA**	$\mathbf{R_0}$ **MEEP**
smf28	1550	980	330	0.3	4.5×10^{-5}	6.4×10^{-5}
FUD 3716	2400	1300	435	0.3	5.0×10^{-5}	3.7×10^{-5}

In Figures 1.8 and 1.9 the distribution of the electromagnetic field is shown for the cleaved fiber facet of the FUD 3716 and the fiber facet with inscribed anti-reflection grating. The direction of the propagation is from the top to the bottom of the figure. The reflection of the light for the perpendicularly cleaved fiber facet is approximately 3.5%. This is demonstrated in Figure 1.8 by the visible interference of the incident and reflected waves. The reflections are suppressed by the AR structured fiber facet as is clearly seen in Figure 1.9, where almost none of the light is reflected.

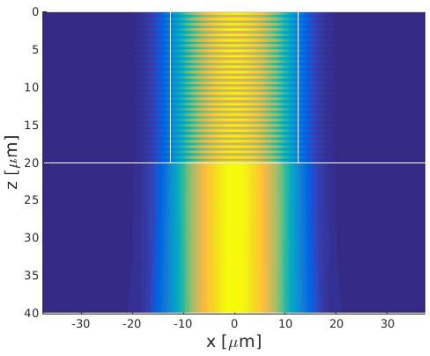

Figure 1.8: E_z component (parallel to the grating grooves) of the field calculated by aRCWA for cleaved fiber facet.

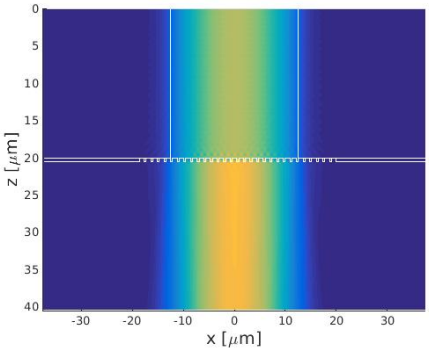

Figure 1.9: E_z component (parallel to the grating grooves) of the field calculated by aRCWA for fiber facet with AR grating.

1.2.2 Low reflecting structures

The idea behind designing the low reflectivity grating is to replace the LR-FBG or cleaved fiber facet as the output of the fiber laser. A typical fiber laser configuration is shown in Figure 1.

There are three main aims in the design of this grating:

- The reflectivity of the grating should be close to Fresnel reflection for the cleaved fiber facet and avoid the diffraction into higher order modes to keep the laser threshold sufficiently low and slope efficiency high.
- The depth of the grating should be as shallow as possible to facilitate the fabrication.
- The difference between reflection of the TE and TM polarization should be maximized to achieve polarized laser output.

This particular kind of grating was designed for a wavelength of 2040 nm. To ensure the first and the last listed aims of the design, we adopted the figure of merit (FOM) in the following equation:

$$\mathrm{FOM} = (R_0^{TE} - R_0^{TM})R_0^{TE}, \tag{1.1}$$

where R_0^{TE} and R_0^{TM} are the zeroth order reflectivity for TE and TM polarized light, respectively. The goal of the optimization process is maximize the FOM while preserving the second listed condition, of fabricability. The reflectivity and FOM were computed by the RCWA method and the results are shown in Figures 1.10 and 1.11. The reflectivity for TE polarization is oscillatory, as expected from the effective-medium theory [38]. The FOM follows the oscillation of the zeroth order reflectivity with its value growing as a result of the increasing difference in the zeroth order reflectivity for TE and TM polarizations. The first maximum of the FOM is at a depth of 590 nm and 0.6 fill-factor. The second maximum is at a depth of 1415 nm and 0.55 fill-factor. The parameters of the grating optimized by the RCWA method are listed in Table 1.4.

Table 1.4: Optimized parameters of the low reflecting polarization sensitive grating. Optimization methods were RCWA and aRCWA.

Grating parameters	**RCWA**	**aRCWA**	**aRCWA**
$\mathbf{h_1}$ [nm]	590	710	700
$\boldsymbol{\Lambda}$ [nm]	1400	1290	1290
Fill factor	0.60	0.70	0.65
$\boldsymbol{\lambda}$ [nm]	2040	2040	2040

To determine the reflection coefficient of the optimized structure, aRCWA, FDTD and FMM analyses were made. The 2D structure was investigated. The structure was a slab wave-guide with dimensions of the optical fiber which are listed in Table 1.2. The geometry of the slab wave-guide is shown in Figure 1.6. The results of

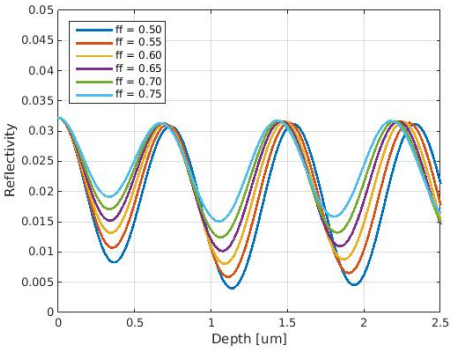

Figure 1.10: Zero order reflectivity of the grating for TE polarization as function of grating depth and grating fill-factor.

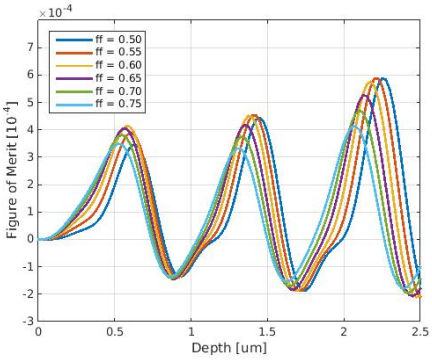

Figure 1.11: FOM as a function of the grating depth.

the zeroth order reflection simulation are compared in Figure 1.12. The RCWA results differ significantly from those of aRCWA, FDTD and FMM. This difference is caused by the approach. The RCWA considers an infinite grating with a plane wave, which is a different structure from the optical fiber as a wave-guide with a grating at the facet. The RCWA method was used to obtain an insight into the problem. The other methods were used for the final optimization.

The $\pm 1^{\text{st}}$ orders of the diffraction have their diffraction angles beyond the critical angle of the total internal reflection and thus represent a source of losses. The losses computed by FDTD and FMM are shown in Figure 1.13. The $\pm 1^{\text{st}}$ orders are shown in Figures 1.14 and 1.15. A short pulse with a broad spectrum was used in the FDTD simulation. The spectral behaviour of the reflectance and transmittance can be extracted from the results when we use a comparison with a reference wave-guide. The reference wave-guide is also shown in Figure 1.15. Known results from the FDTD simulation are F_{1g} and F_{2g}, which are the fluxes at the start and end of the wave-guide with grating at the end of the wave-guide. Similarly we have fluxes F_{1f} and F_{2f} with f referring to the optical fiber without grating at the end. From these fluxes we can compute the reflectance of the grating as in Equation (1.2) and the transmittance as in in Equation (1.3). The flux which is absorbed by the PML on the sides is considered as losses. Equation (1.4) gives the losses.

$$R_g = \frac{F_{1f} - F_{1g}}{F_{1f}} \tag{1.2}$$

$$T_g = \frac{F_{2g}}{F_{2f}} \tag{1.3}$$

$$L_g = 1 - (R_g + T_g) \tag{1.4}$$

Two similar sets of grating parameters were selected after optimization. The parameters are shown in Table 1.4. The parameters computed by the aRCWA method were used in the fabrication explained in Section 3.5.

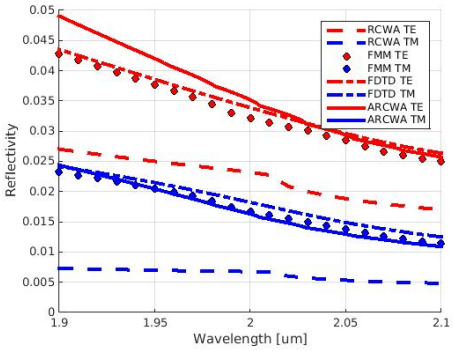

Figure 1.12: Zero order reflectivity of the grating for TE and TM polarizations as a function of the wavelength obtained by RCWA. FMM, FDTD and ARCWA methods.

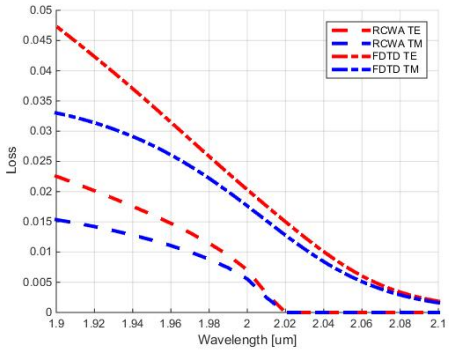

Figure 1.13: Loss of the TE and TM polarizations as functions of the wavelength computed by RCWA and FDTD methods.

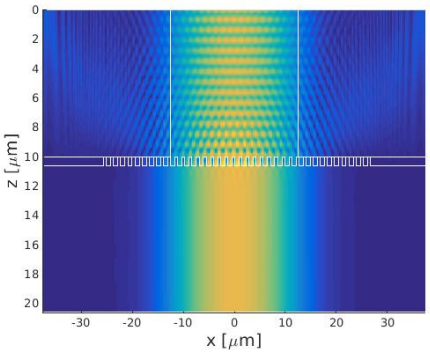

Figure 1.14: E_z component (parallel to the grating grooves) of the field calculated by aRCWA for low reflecting polarization sensitive grating mirror.

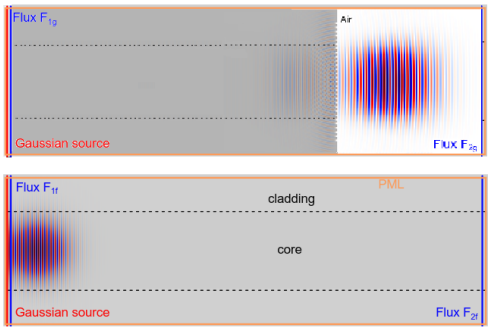

Figure 1.15: E_z component (parallel to the grating grooves) of the field calculated by FDTD for low reflecting polarization sensitive grating mirror.

1.2.3 High reflecting structures

The design of the high reflectivity grating was made especially for the thulium doped fiber laser presented in Section 4.2. The resonator of the laser consists of a large-mode area, double-clad, polarization maintaining thulium-doped fiber, pump–signal combiner, and two mirrors. Laser diodes with multi-mode pigtails are used for pumping the double-clad active fiber over the pump–signal combiner. The low-reflectance mirror is formed by a perpendicularly cleaved output fiber of which the reflectivity is 3.5% in accordance with the Fresnel equations. The high-reflectivity wavelength- and polarization-selective mirror was fabricated on the perpendicularly cleaved pigtail of the pump–signal combiner in the form of a leaky-mode resonant diffraction grating.

The high reflectivity mirror was designed to have a resonant wavelength of 2000 nm, modal reflectivity close to 100%, a high polarization extinction ratio,

and a reasonably narrow bandwidth. These parameters can only be achieved by using a layer with a refractive index of 1.7 or higher [39].

We selected two materials to be tested: Ta_2O_5 and HfO_2. Both are transparent for wavelengths around 2 μm. The Ta_2O_5 have a slightly larger refractive index (2.05) than HfO_2 (1.90). The real refractive indices depend on the thin layer manufacturing technology. The sputtering process used by us is described in Section 2.2. The HfO_2 was selected for the testing process due to its higher laser induced damage threshold (LIDT) [40].

The numerically simulated structure of the fiber facet and high refractive index layer with grating is shown in Figure 1.7. The single mode fiber has a core with radius r_{co} and cladding with radius r_{cl} as well as an oxide layer with high refractive index n_{ox} and thickness h. The fiber parameters are listed in Table 1.5. The grating grooves have a depth of h_1 and the remaining material forms a wave-guide with thickness $h_2 = h - h_1$. The grating has period Λ and fill-factor f. The leaky mode in the wave-guide layer can be excited by the $\pm 1^{st}$ diffracted order. Two leaky modes propagating in opposite directions are excited simultaneously. The leaky modes are diffracted by the grating structure and interfere with the reflected and transmitted orders. The grating is again designed only to have zeroth order in transmission and reflection. The transmission is canceled by the ϕ-phase shifted first-order diffracted mode at resonance. A high reflectivity can be achieved this way. The presence of the leaky modes is shown in Figures 1.16 and 1.17.

Table 1.5: Parameters of the PLMA-GDF-25/400-10FA (FUD 3716) fiber with high refractive index layer used in the simulation.

Fiber parameters	**Value**
$\mathbf{r_{co}}$ [μm]	12.5
$\mathbf{r_{cl}}$ [μm]	40
Fiber length [μm]	2
$\mathbf{n_{air}}$	1
$\mathbf{n_{co}}$	1.4428
$\mathbf{n_{cl}}$	1.44
$\mathbf{n_l}$	1.906

The design was again made using a simulation by the FDTD and aRCWA methods. The FMM method was used to compare the 2D results and to confirm them with a 3D simulations. The laser operates in the CW regime but the simulation performed by the FDTD method used only pulses with excitation of the fundamental mode only. But the results for the FDTD and aRCWA methods are the same. The optimized parameters are shown in Table 1.6. Figure 1.18 compares the 2D and 3D FMM simulations. The results are in good agreement. Figure 1.19 compares the 2D FDTD and FMM results: they are almost indistinguishable.

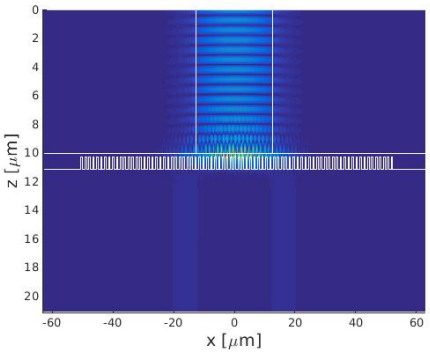

Figure 1.16: E_z component (parallel to the grating grooves) of the field calculated by aRCWA for high reflecting polarization sensitive grating mirror.

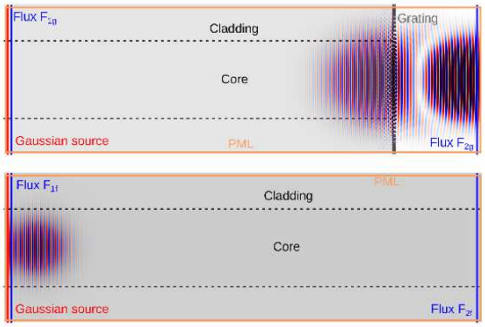

Figure 1.17: E_z component (parallel to the grating grooves) of the field calculated by FDTD for high reflecting polarization sensitive grating mirror.

Table 1.6: Optimized parameters of the high reflecting polarization sensitive grating.

Grating parameters	**Value**
$\mathbf{h_1}$ [μm]	0.860
$\mathbf{h_2}$ [μm]	0.270
$\mathbf{\Lambda}$ [μm]	1.295
Fill factor	0.62
$\boldsymbol{\lambda}$ [μm]	2

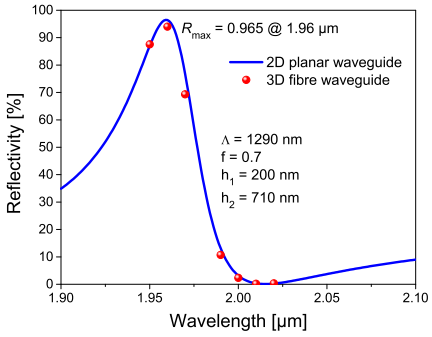

Figure 1.18: Comparison of the 2D and 3D computation performed by FMM.

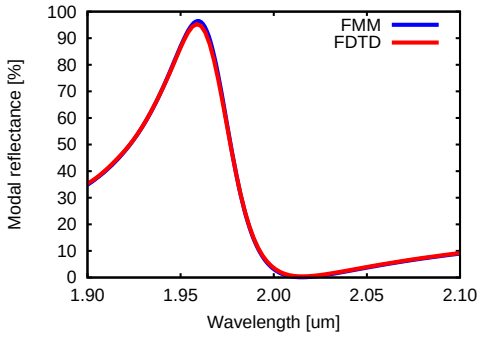

Figure 1.19: Comparison of 2D computation performed by FMM and FDTD.

We studied the grating behaviour around the optimized parameters to obtain a deeper insight. Both TE and TM polarizations were studied although the TM polarization has worse performance and was not used in the experiments. We varied one selected parameter while the others remained fixed at their optimized values. The fill-factor was varied with a step of 0.03 in the interval 0.53–0.80. Figures 1.20 and 1.21 show the results when varying the fill-factor, for both the TE and TM polarizations. An increase in the reflectance for the TE polarization is observed while increasing the fill-factor from the starting point of 0.53 till it hits its maximum at around 0.69, after which it decreases. For TM polarization the behaviour is similar but the maximum reflectivity is shifted towards higher wavelengths. Figures 1.22 and 1.23 show the behaviour of the structure while the period is varied in the interval 1285–1305 nm. The maximum reflectivity is preserved for TE polarization while changing the period of the grating. For TM polarization we can observe an increase of the reflectance with an increasing of the period of the structure, and also the wavelength band is shifted up about 70 nm. While varying h_1 in the interval 750–910 nm we can see in Figure 1.24 a narrowing of the bandwidth and a slight increase of the reflectance with increasing values for the TE polarization. We can not go to larger values of h_1 due to the requirement of the structure's manufacturability. For TM polarization again the wavelength band is shifted up and we can observe a decrease in the reflectance while increasing h_1 together with shifting the central wavelength of the peak towards higher wavelengths. The h_2 parameter was varied in the interval 200–340 nm. Figure 1.26 shows the result of the simulation for the TE polarization. The maximum reflectivity slightly decreases while increasing h_2. For TM polarization we can observe in Figure 1.27 a larger drop in the reflectance while varying h_2. During the manufacturing process we can control the total layer thickness h and h_1. The value of h_2 depends on these. The parameters are connected by the relation $h = h_1 + h_2$. Figures 1.28 and 1.29 show the behaviour of the grating when we tie together the parameters h_1 and h_2. One can see the shift in the wavelength and change in the shape of the peaks for the TE polarization. For TM polarization one can see the shift in the wavelength and small variation in the value of the maximum reflectance. This behaviour was expected for both polarizations from the previous simulation.

The thickness of the wave-guide layer h_2 has a direct impact on the guided mode. The fill factor determines the effective refractive index of the grating layer and has a direct impact on the properties of the wave-guide as well. Variations of either of these parameters have a strong influence on the resonance wavelength and peak modal reflectance. For the optimal parameters, the modal reflectance of the TE polarization reaches 96%, while for the TM mode it remains low: 1.6%. The polarization extinction ratio achieves 17.8 dB.

At the beginning of this section we introduced the numerical modeling methods used for the optimization of the diffraction gratings, namely RCWA, aRCWA and FDTD. Then we used RCWA first to understand the nature of the problem and what behaviour we can expect from diffraction gratings with only 0th real diffraction order. To validate the numerical results we used aRCWA and FDTD to optimize the anti-reflection, low-reflection polarization sensitive and high-reflection polarization sensitive 1D structures on the optical fiber facet.

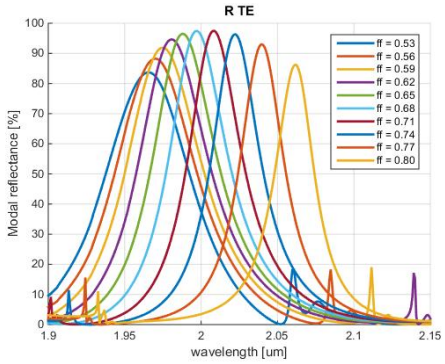

Figure 1.20: Dependence of the spectral shape of modal reflectance on fill-factor for TE polarization.

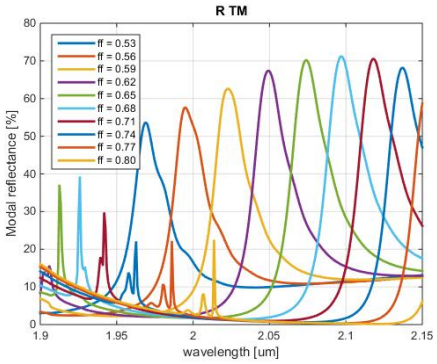

Figure 1.21: Dependence of the spectral shape of modal reflectance on fill-factor for TM polarization.

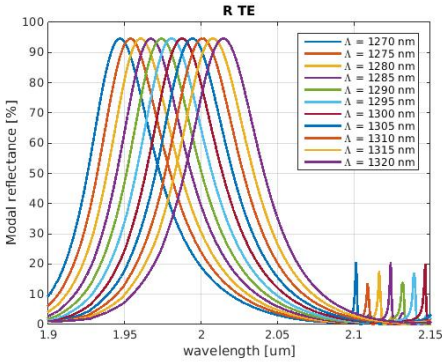

Figure 1.22: Dependence of the spectral shape of modal reflectance on grating period for TE polarization.

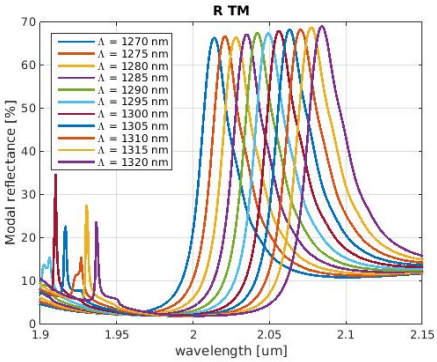

Figure 1.23: Dependence of the spectral shape of modal reflectance on grating period for TM polarization.

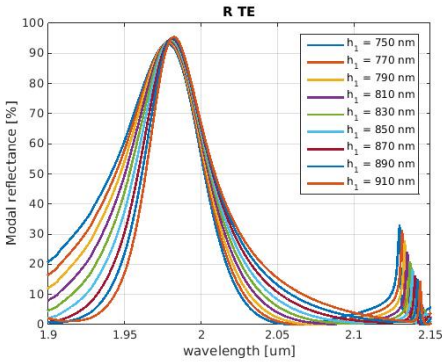

Figure 1.24: Dependence of the spectral shape of modal reflectance on grating groove depth h_1 for TE polarization.

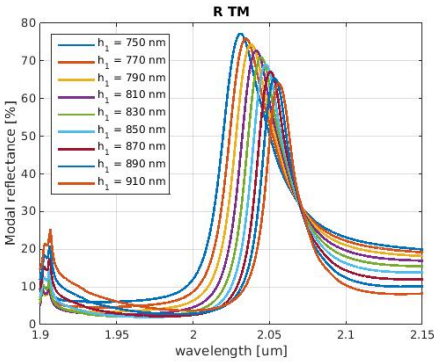

Figure 1.25: Dependence of the spectral shape of modal reflectance on grating groove depth h_1 for TM polarization.

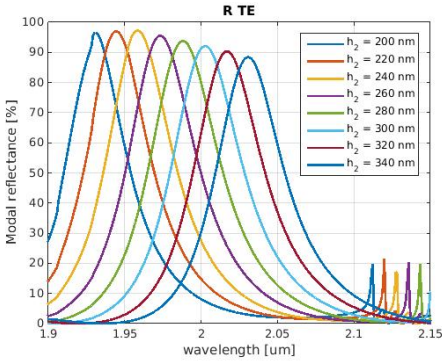

Figure 1.26: Dependence of the spectral shape of modal reflectance on guiding layer thickness h_2 for TE polarization.

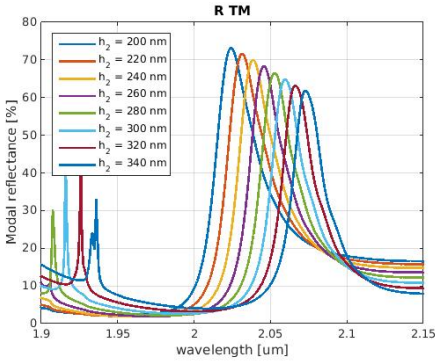

Figure 1.27: Dependence of the spectral shape of modal reflectance on guiding layer thickness h_2 for TM polarization.

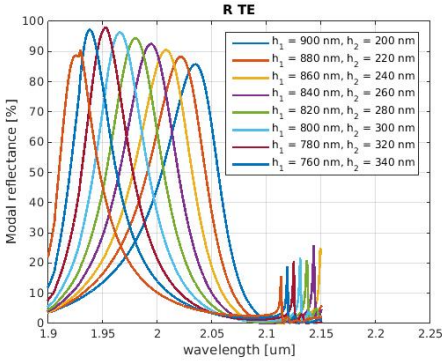

Figure 1.28: Dependence of the spectral shape of modal reflectance on grating groove depth h_1 and guiding layer thickness h_2 for TE polarization.

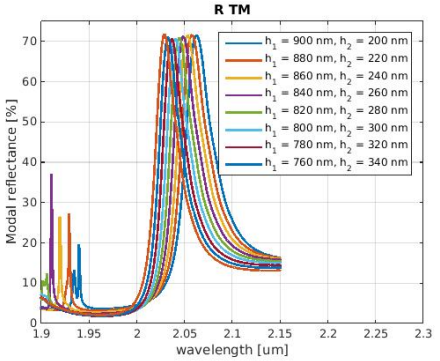

Figure 1.29: Dependence of the spectral shape of modal reflectance on grating groove depth h_1 and guiding layer thickness h_2 for TM polarization.

Chapter 2

Prefabrication procedures

In this chapter we will explain the steps of the procedure before the inscribing of the grating on the fiber facet. First we will introduce the cleaning and preparation steps of the fibers and holder, their cleaving and cleaning. Then we will introduce the process of sputtering the high refractive index material layer.

2.1 Fiber and holder preparation

In this section we explain the process of cleaving the optical fiber and cleaning the optical fiber facet, as well as cleaning and preparing the holder. The last step before sputtering the high index layer or FIB process is inserting the fibers into the holder and connecting them electrically with the holder. This step is essential to overcome the charging issue.

2.1.1 Fiber cleaving and cleaning

We used various fibers for fabricating the diffraction gratings. In this work we will describe the process with the standard communication fiber smf28 and with Nufern PLMA-GDF-25/400-10FA (FUD 3716) fiber. For cleaving we used a Vytran LDC200 cleaver and for inspecting the cleaved fiber facet there was used the Vytran GPX3400 splicing machine. In Figures 2.1 and 2.2 there are shown the cleaver and the splicer machine.

We found that after cleaving the PM fiber (maybe fibers in general) there remain shards on the cleaved facet. For sputtering a layer on the facet or inscribing the diffraction grating directly, there should be no shards, dust or any other contamination. We tried cleaning the fiber facet with isopropyl alcohol and pressured air. After this cleaning step, because it alone was unsatisfactory, we used acetone and ultrasound cleaning for 1 minute. The result was great and no shards or dust were spotted while viewing the fiber facet with an optical microscope. Figures 2.3, 2.4 and 2.5 shows the cleaning process from the start with just the cleaved fiber, then the fiber cleaned with isopropyl alcohol and air, and finally the fiber cleaned with acetone in an ultrasound cleaner, respectively. Then we tried only cleaning the fiber facet with acetone in the ultrasound cleaner and the result was the same even without the additional step of cleaning with isopropyl alcohol, cloth, and pressured air. The results are shown in Figures 2.6 and 2.7.

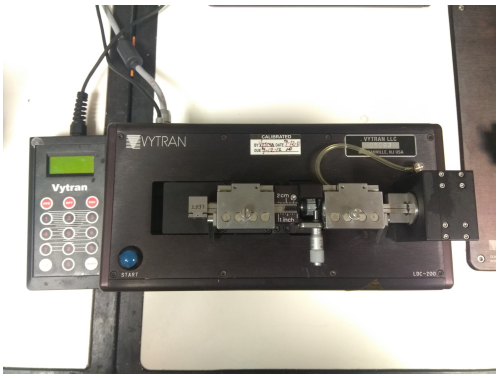

Figure 2.1: The Vytran LDC 200 cleaver.

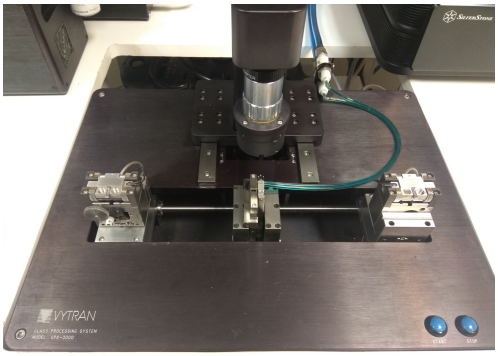

Figure 2.2: The Vytran GPX3400 splicing machine.

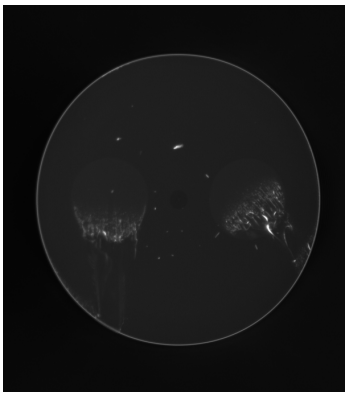

Figure 2.3: The PLMA 25P/400 fiber cleaved by LDC 200.

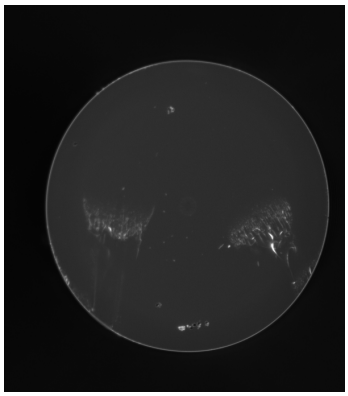

Figure 2.4: The PLMA 25P/400 fiber cleaved and cleaned with isopropyl alcohol and air.

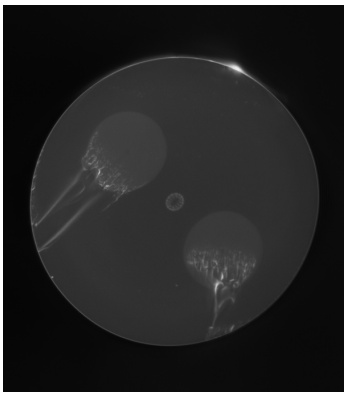

Figure 2.5: The PLMA 25P/400 fiber cleaved and cleaned with acetone in ultrasound cleaner.

The direction of cleaving also affects the quality of the final fiber facet surface. When the direction of the cleaving is the same as the slow axis of the PM fiber, the resulting cleaved surface has minimal surface distortion.

2.1.2 Holder preparation

Before every process, the holder is cleaned with acetone and ultrasound cleaner. This takes approximately two hours. The holder is hexagonal with grooves for 125 μm and 400 μm fibers. The photo of the holder is shown in Figure 2.8. For the smf28 fibers, which can be bent with a diameter of 3 cm without damage, the holder can be loaded into the FIB machine through a load-lock chamber. For thicker fibers, this is not an option: they have a bending diameter around 200 mm and the entirety of the vacuum chamber has to be opened. The loading process is explained in subsection 3.1.2. The whole holder was fabricated at our Institute of Photonics and Electronics of the Czech Academy of Sciences.

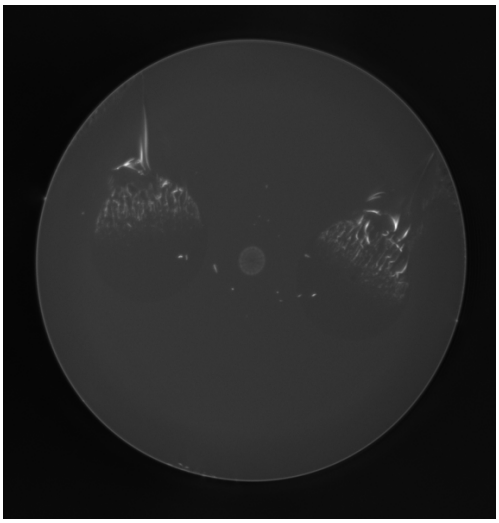

Figure 2.6: The PLMA 25P/400 fiber cleaved by LDC 200.

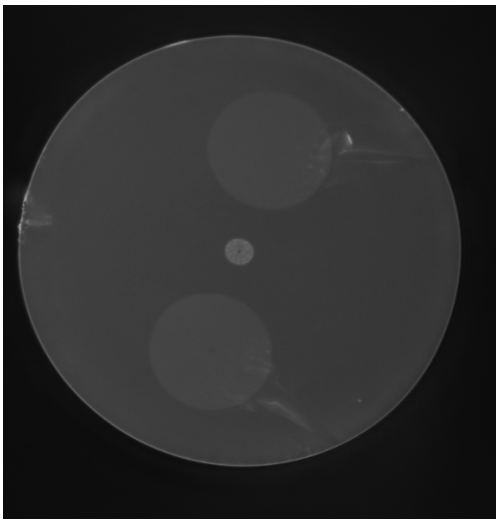

Figure 2.7: The PLMA 25P/400 fiber cleaved and cleaned with acetone in ultrasound cleaner.

Figure 2.8: Photo of disassembled fiber holder.

As preparation for inserting the fiber into the holder, the holder is screwed to a 3-axis stage from Thorlabs. The stage with fiber clamp holder is used to position the fiber in the V-groove. In the V-groove the fiber is held by conductive silver paste and a plate with screws. In the scanning electron microscope (SEM), where electrons are used to probe the sample, charging is present for non-conductive samples. The paths of the electrons are distorted by the charge of the sample which can not be conducted away. Silver paste is used to connect the grounded holder with the fiber facet, where there can be used various ways to mitigate the charging. The methods used for resolving the charging problem are explained in Section 3.2. The silver paste has to cover a little area from the fiber facet. This is done by pulling the fiber facet backwards to position it parallel with the surface of the holder. Due to capillary forces, part of the silver nano-particles and solvent cover, in the ideal case, the edge of the fiber facet. We use two USB microscopes to control the correct position of the fiber in the holder and distribution of the silver paste. One microscope, with a longer working distance and magnification of 90×, is positioned to look from the top, and the other, with magnification 230×, is positioned to look directly at the fiber facet. The top view is shown in Figure 2.9 and the fiber facet view is shown in Figure 2.10.

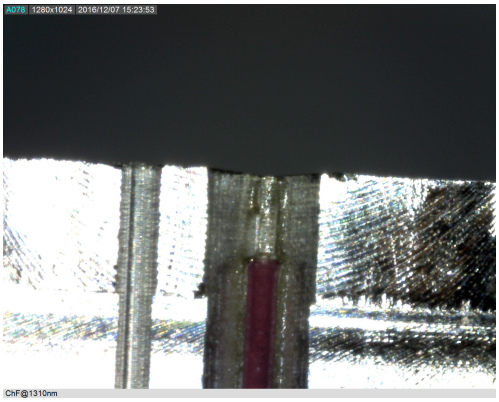

Figure 2.9: Top view of the fiber placed in the holder.

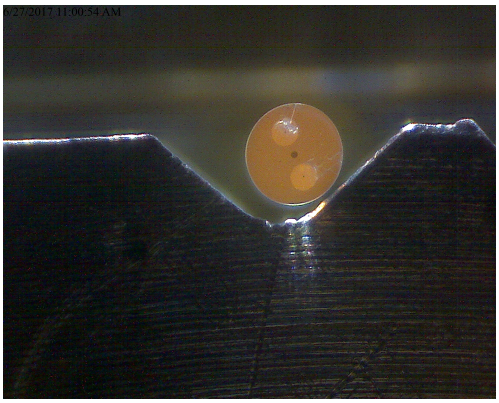

Figure 2.10: Fiber facet view of the fiber holder.

When all 6 fibers are positioned in the holder, a protection cap is mounted to protect the fiber facets during moving and assembling the whole holder. For 400 μm fibers, the whole procedure of holder preparation ended with this step. For smf28 fibers there are more steps. The fibers are twisted inside the holder can and the whole holder is capped. The end of the twisting process is crucial because the fibers need to be positioned properly because it is very easy to crack them.

2.2 Sputtering process

Electron beam physical vapor deposition is the process of sputtering thin films of material onto a substrate. The material thin film is sputtered on the sample for various reasons, such as: to be a thermal shield, protective layer, chemical barrier, reflective or anti-reflective coating, anti-scratch coating, etc. The generated electron beam is directed onto the evaporated material. The material is evaporated into

a cone and covers everything in the way. The growing speed is controlled by an oscillating crystal and changes of its frequency. We used an electron beam sputtering machine to sputter a high refractive index layer on our fiber samples.

Before we put the samples inside the vacuum chamber and started the pumping, we added one additional step to the cleaning process described in subsection 2.1.1. This step is one minute in the plasma etching machine to prepare the surface of the fiber facets for sputtering. Without this step, the layers do not have a good adhesion to the surface. This is shown in Figures 2.11 and 2.12.

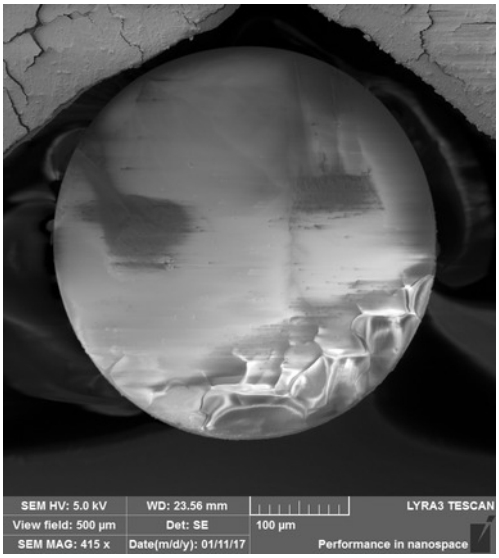

Figure 2.11: Fiber facet with sputtered Ta_2O_5 without plasma etching before sputtering process.

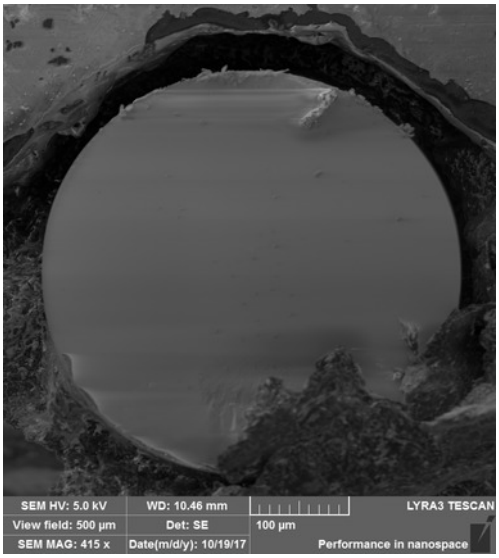

Figure 2.12: Fiber facet with sputtered Ta_2O_5 with plasma etching before sputtering process.

We used a Pfeiffer vacuum sputtering machine PLS 570 with electron gun. First the chamber is pumped to 8×10^{-5} Pa. Normally we let the chamber be evacuated overnight. When the pressure is stable, oxygen is added to the final pressure of 2.4×10^{-1} Pa. We want to sputter two materials Ta_2O_5 and HfO_2. We used 99.99% purity granulated Ta and Hf to achieve that. The oxygen is added to the vacuum chamber to produce an oxide layer. The electron gun with voltage 10.3 kV is used to sputter the material. The sputtering speed is 1.0–1.4 Åper second.

The thickness of the layers was verified after the sputtering process using an AlphaStep stylus profiler and in the electron microscope with focused-ion beam milled structure. The refractive index was measured using a Sentec ellipsometer. The fabricated layers were measured using a fused-silica substrate with a deposited oxide layer. The deposition on this substrate was done during the deposition of the oxide layer onto the fibers. The substrate was glued to the fiber holder during the prefabrication procedure. This ensured that the oxide layer on the substrate had the same thickness as that on the fibers.

2.2.1 Profilometry

A stylus profiler is a device which measures the topography of a surface using a tip which is in contact with the surface of a sample using constant force. The force is driven by a feedback loop. From the data, the surface topography can be visualized and attributes like its roughness and shape, steps, curvature and flatness can be computed. A half-covered fused-silica substrate was positioned in the middle of the fiber holder during the prefabrication procedure. The step from the covered to the not covered part was measured using a profiler to verify the measurement during the sputtering process.

2.2.2 Ellipsometry

Ellipsometry is a measurement technique developed to characterize the dielectric properties of thin film material. Dielectric properties include the complex refractive index and complete dielectric function. Also, the film thickness is derived from the measurement. Even multi-layer structures can be characterized. The measurement process is mainly in a reflective geometry where polarized light falls on the sample at a specific angle of incidence and is reflected to the detector. The response is fitted into a model of the structure and results in values for the thicknesses of the layers and refractive indices or dielectric functions.

In this section we introduce the procedures preceding the fabrication of the diffraction structures onto the optical fiber facet. The fibers need to be cleaved and cleaned perfectly to ensure that the fiber facet has no residual shards or contamination which can be a problem for both a direct inscription and a sputtering process. A special holder was machined to hold the fibers during the plasma cleaning, sputtering and fabrication process. The sputtering process is described and tools for characterization introduced.

Chapter 3

Fabrication procedures

In this chapter we will introduce the FIB machine Tescan Lyra3 and the process of direct inscription of the diffraction grating on the fiber facet. The FIB and SEM system is described and the geometry of this complex system is introduced. The issue of charging of the non-conductive dielectric samples is investigated. The process of optimization of the FIB parameters is described and finally the process of direct inscription of the numerically optimized structures is introduced.

3.1 Focused ion beam process

In this section we will introduce the FIB technique and SEM used to fabricate the diffraction gratings on the fiber facet. We will treat the process of loading the sample into the vacuum chamber and the SEM/FIB system we used.

3.1.1 Electron microscopy

To investigate our samples and fabricated structures we used a SEM. Due to the shorter wavelength of an electron, the resolution of this technique goes to the nm scale, which is essential for imageing sub-μm structures. SEM uses a scanning pattern to probe the sample with a focused electron beam. This is called raster scanning. During the interaction of the electrons with the sample surface, energy is lost by the electrons in various ways (low-energy secondary electrons or high-energy back-scattered electrons (BSE) emission, heat dissipation, as well as the emission of light or X-rays). In our system we have the possibility of using secondary electrons and back-scattered electrons to image the sample surface topography. We mainly used secondary electrons as the information source about our samples.

The system schematics are shown in Figure 3.1. The electrons are emitted from the electron gun and accelerated through the anode. The Tescan Lyra 3 system is equipped with a Schottky type field emission gun (FEG). This emitter consists of a very sharp tungsten tip coated with zirconium oxide. The tip is sharpened to a diameter of around 2 μm. The electron beam comes through a condenser lens. This lens focuses the beam through an aperture which limits the beam size. Then the beam comes through the objective lens, which focuses it onto the sample. The scanning is done by the scanning coils. The back-scattered electrons are detected by the detector, which can be positioned above the sample surface close to the end

of the electron objective. The deployment of a BSE detector limits the working distance of the whole system, e.g. we can not go too close to the sample due to the danger of hitting the BSE detector. The secondary electrons originate from the sample material. They are knocked out by the probing electrons.

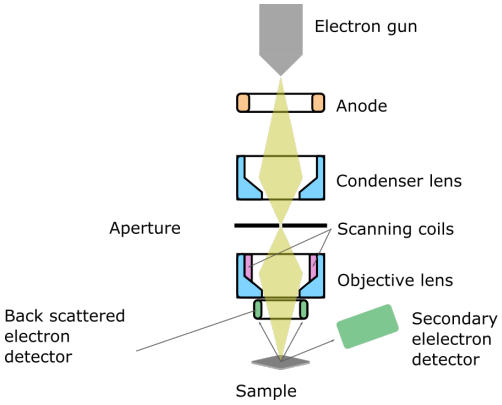

Figure 3.1: Schematic drawing of the SEM.

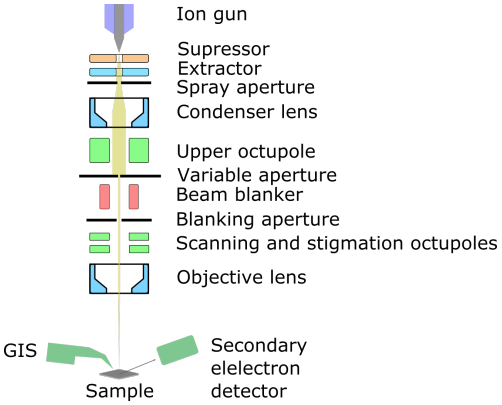

Figure 3.2: Schematic drawing of the FIB.

3.1.2 Focused ion beam technique

A FIB technique uses, as its name implies, a beam of ions which is focused on the sample surface to probe its topography. Mostly it uses a liquid metal ion source (LMIS) made from gallium. In this type of ion gun, the gallium is heated to its liquid form and wets a tungsten needle. A Taylor cone is formed at the end of the tip of the needle by the opposing forces of surface tension and the electric field. The size of the Taylor cone is around 2 nm and, in combination with the electric field, forces the ionization of the gallium and a field emission of the ions. A schematic drawing is shown in Figure 3.2.

A FIB can be used for imaging samples, directly etching structures onto the sample surface, or even the deposition of various materials. A FIB is innately destructive for the sample. Thus, for imaging, the lowest possible current is used, and the beam is blanked while not in use. Blanking the beam while the FIB is running is better for the system than shutting it down repeatedly. Powering up is not instantaneous, and the power up routine wears the gun considerably more than operation for the same time. On the other hand, the destructive attribute is used for direct etching of structures into the sample. The atoms of the material are sputtered out of the sample surface when high energy gallium ions land there. The ions are also used to deposit materials from vapours onto the sample surface. The precursor gas is decomposed by the ions into volatile and non-volatile components. The non-volatile component of the gas remain on the sample surface while the volatile component is pumped out by the vacuum pump. The deposited layer can be used to protect the surface from being damaged by the FIB, or as we used it, to prevent charging. A device called a gas injection system (GIS) provides the vapours of the various precursor gasses and delivers them in front of the sample.

We used a Tescan Lyra3 focus-ion beam and SEM equipped with a GIS and time-of-flight secondary mass spectrometer. Our system combines a field emission

electron microscope with a gallium ion gun. The electron and ion beams are inclined at an angle of 55 degress, which means we can see a cross-section of the fabricated grating and therefore measure the dimensions of the grating grooves (depth, width, period) as well as their shape. Also, the integration of the GIS is very important for us. We can deposit a Pt layer, which can help us prevent charging, and which is essential for measuring the profile of the grating grooves. A schematic drawing of the geometry of the SEM/FIB is shown in Figure 3.3. On the left is shown the operation of the FIB for the inscription of the structures, and on the right is shown the use of the SEM for the investigation of the sample.

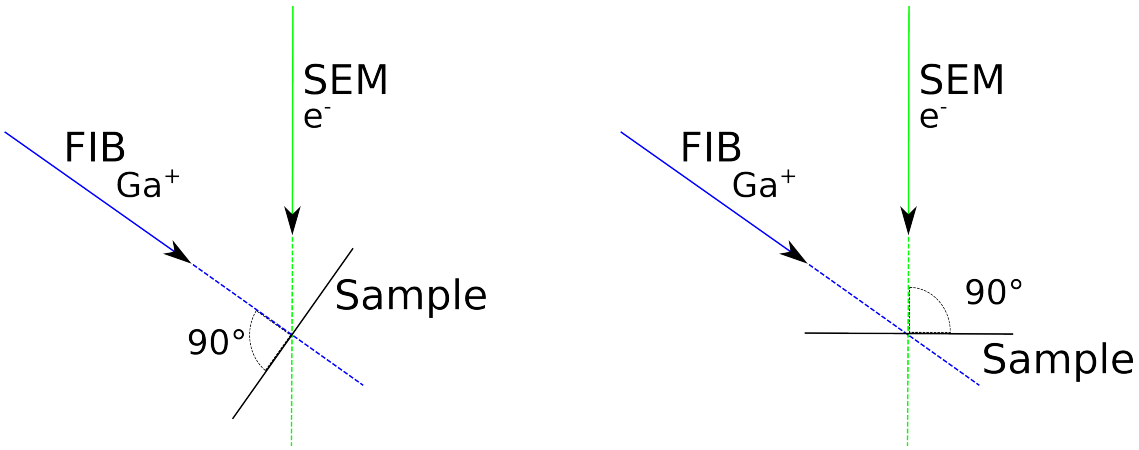

Figure 3.3: FIB/SEM geometry. Left: FIB operation for inscription of the structures. Right: Normal SEM operation.

The Tescan Lyra3 system is equipped with a load-lock chamber. This chamber is connected with the main vacuum chamber by a tunnel which is sealed during normal operation. The advantage of this approach is the fast recovery time of the vacuum after loading the sample. Only a small volume of load-lock is exposed to the outer air. The load lock is pre-pumped and only then is the tunnel opened to the main vacuum chamber. A drawback is the size of the tunnel and load-lock chamber itself. Normally it is enough for various samples to be examined by SEM or the FIB. For our needs, the load-lock chamber can be used only for the smf28 fibers since they can be bent and canned inside our holder. Thicker fibers like the 25P/400 we were using can not be bent to such a small diameter without breaking. For loading 25P/400 fiber samples we need to open the entire main vacuum chamber. The fibers are bent to fit in the vacuum chamber and to touch the detectors, electron and ion gun column or devices and the detectors attached inside. The bent fibers are held on the moving holder by vacuum compatible adhesive carbon tape. A view of the fibers attached to the holder and secured while the vacuum chamber is open is in Figure 3.4.

Stable vacuum conditions are achieved after 15 minutes of pumping when a load-lock chamber is used. This is convenient for fast testing and fabrication of smf28 samples. Achieving stable conditions with a high vacuum after opening the main vacuum chamber is more time consuming. More than 12 hours were needed to achieve stable conditions.

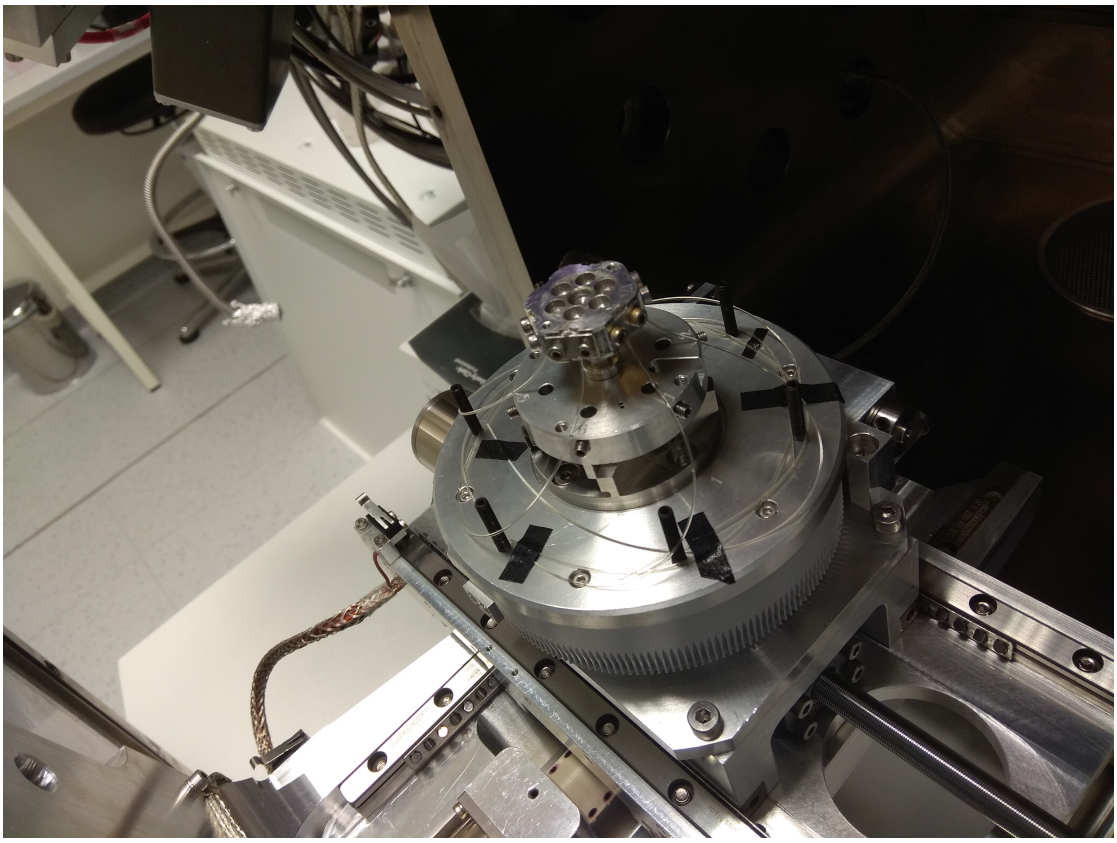

Figure 3.4: Photo of Tescan Lyra3 open chamber with fiber holder.

3.2 Solution of charging issue

In this section we will introduce the issue of sample charging in the SEM. In this system we have to deal with sample charging because the optical fibers are made from silica glass and therefore they are not conductive.

Charging is naturally connected with dielectric samples. In a dielectric, there is no free movement of the electrons and therefore when we put the sample in the electron beam, charging occurs. The electrons of the scanning beam are implanted into the material and they deflect the in-coming and out-coming electrons. The picture is then not clear, but is blurry and even distorted. The same thing happens with gallium ions. The result of the grating fabrication is bent or distorted. We have good electrical contact between the silver paste and the fiber holder, as was described in subsection 2.1.2. Now we need to collect the charge from the fiber facet. Other way to avoid charging during SEM imaging is to lower the acceleration voltage. We ended up using 5 kV for imaging our samples.

There are are a few ways to deal with the charging issue in non-conductive samples. Many of those approaches were developed for biological samples. We can categorize these methods into the following approaches: charge compensation, lowering the vacuum, cutting out a layer affected by the charging from the sample, or sputtering a conductive layer on the sample. We can not cut out an affected layer of the sample or lower the vacuum. Lowering the vacuum is not possible for our

manufacturing process, since a lower vacuum leads to distortions of the fabricated structure. The charge compensation by an electron beam was used during the fabrication process. We also investigated the sputtering method.

We tried the AquaSave conductive polymer [41], carbon evaporation, chromium sputtering and focused-ion beam platinum deposition using a GIS. The sputtered carbon layer was not homogeneous and even spits of carbon were found. Therefore, this method was not reliable for our fabrication purposes. AquaSave conductive polymer, chromium and platinum direct deposition were tested.

3.2.1 AquaSave

AquaSave conductive polymer was dissolved in the water, which makes it easy to handle. A layer of this polymer was applied on the fiber facet by a micro-pipette. Then the whole holder with fibers was put into the spin-coater with the fiber facets perpendicular to the axis of rotation and a thin layer of AquaSave was made. We used three speeds for the spin-coater to test the resulting thicknesses. A groove was milled into the AquaSave layer by a FIB and the thickness of the layer was measured by the SEM. Three thicknesses, 990, 440 and 91 nm, were achieved by spinning the fiber holder at speeds of 500, 1000, and 1500 rpm, respectively.

A focus-ion beam milling test was performed. It is clear from Figure 3.5 that the structure of the polymer is porous. That means the milling process will be inhomogeneous and the grating groove surface will not be optimal. The optimal thickness will be around 100 nm but there is a problem with milling the AquaSave polymer out while scanning the fiber facet by a focused-ion beam for getting the picture. This picture is then used by the DrawBeam software to position the milled structures. Without the correct position of the fabricated structure we can not ensure covering the fiber core and zone around it by the structure.

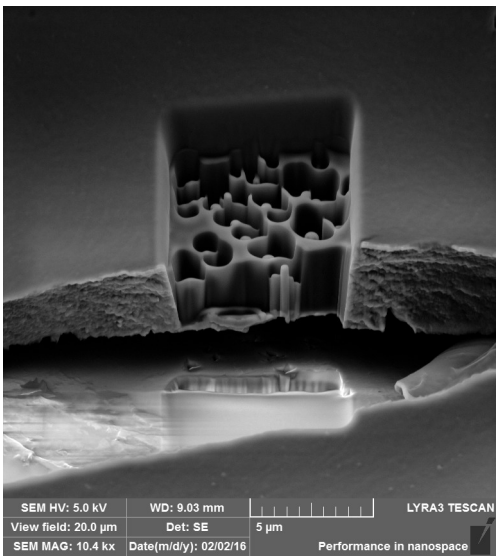

Figure 3.5: AquaSave polymer focused-ion beam mill test.

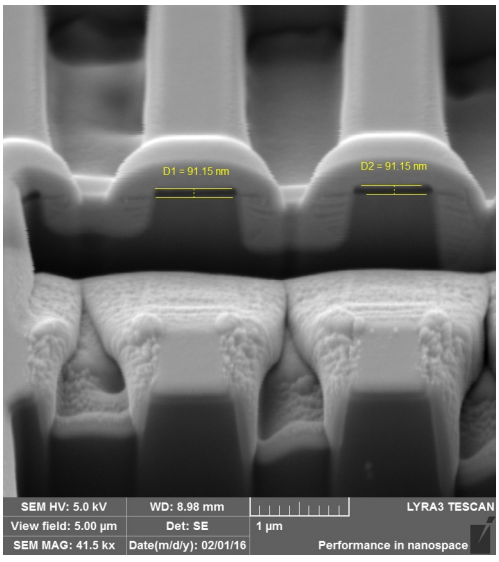

Figure 3.6: The thickness of the AquaSave layer resulting from 1500 rpm.

3.2.2 Platinum

Platinum was sputtered using the GIS with the focused-ion beam to the surface in the selected shape. For the optimization, we covered the whole area with a thin 'layer' of platinum. It is not clear what to write about the 'layer' here. We discovered that the layer will have sub-nm thickness when using the parameters set in the DrawBeam software. We set the thickness parameter to be 1 nm and the time needed to cover the whole area was then computed according to the beam current. The process of the sputtering goes in layers. The focused-ion beam scans the whole area in the selected pattern, which is zig-zag in our case. We stopped the process after $1/5^{\text{th}}$ of the time calculated to deposit a 1-nm platinum layer. This prevents the charging problem completely. The area covered with platinum is shown in Figure 3.7.

For the inscription of the final grating across the fiber core there was used the technique of covering the whole area with platinum or making a platinum fence around the inscription area. The fence with inscribed grating is shown in Figures 3.8 and 3.9. Covering the whole area with platinum works well for low reflecting gratings which are inscribed on the fiber facet without any additional layer [21]. The platinum is then removed by a few scans of the focus-ion beam across the whole area. But there is no proof that the platinum is completely gone. This is the reason we developed the platinum fence technique for the high reflection gratings. Figure 3.8 shows that the image is still distorted for the visualization. Also, a sputtered chromium layer was investigated, and is described in what follows.

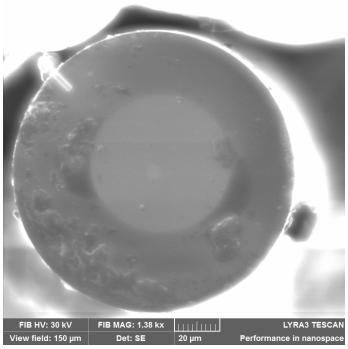

Figure 3.7: The PLMA 25P/400 optical fiber with platinum deposited.

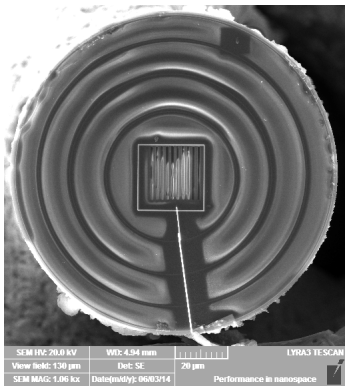

Figure 3.8: The smf28 optical fiber with platinum fence deposited.

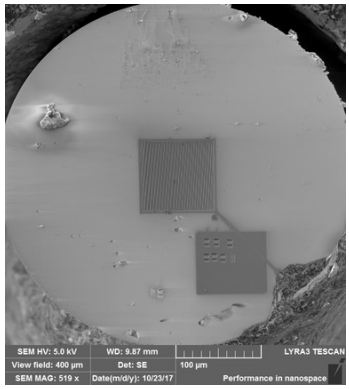

Figure 3.9: The PLMA 25P/400 optical fiber with platinum fence deposited.

3.2.3 Chromium

A chromium layer was deposited using a sputtering process. The technology used was the same as for sputtering layers of Ta_2O_5 and HfO_2. We tested a 50-nm layer of chromium deposited on the smf28 fiber facet. The chromium layer not only prevents the sample from becoming charged, but also prevents the sample surface from being damaged by the FIB. This layer can be called sacrificial due to its purpose and its

etching at the end of the fabrication process. Some back sputtering of the milled material was also spotted during the FIB process. This material was removed with the chromium layer.

The fibers were positioned into the holder. The process is described in subsection 2.1.2. Then the sputtering process follows. The sputtering process and technology is described in section 2.2. Layers with a thickness of 50 nm were deposited. The layer was visualized using SEM while testing the inscription of the circular structures and is shown in Figure 3.10. A strip of platinum is sputtered across the fabricated structure. The platinum has a height of approximately 40 nm, which is enough to fulfill the cross-section of the structure. Finally, we milled a triangular trench in the middle of the platinum strip with a depth equal to 1.5 times that of the grating grooves. A side view of this trench is shown in Figure 3.11 together with the directions of the SEM and FIB beams. Platinum was used due to its good contrast and availability in the GIS system.

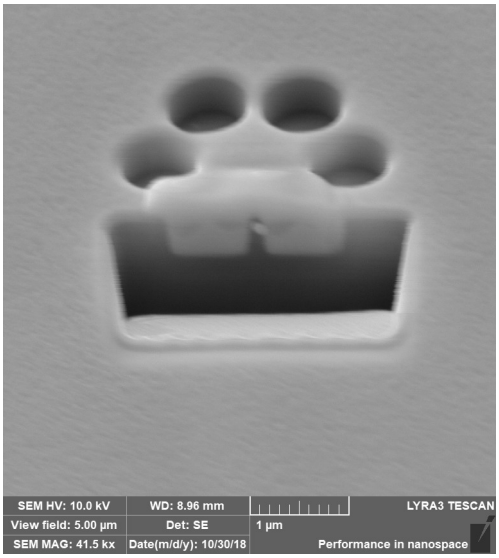

Figure 3.10: SEM visualization of the 50-nm chromium layer which is preventing charging.

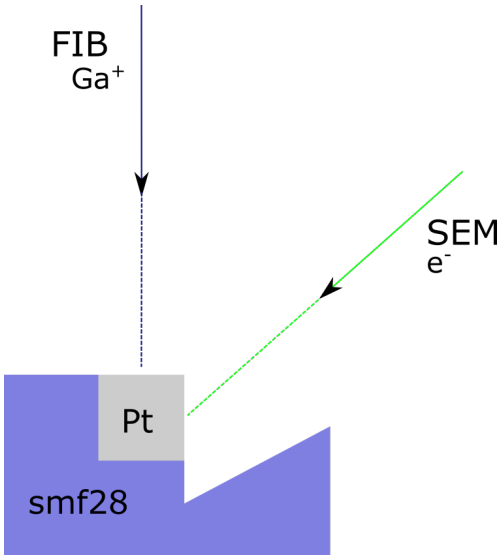

Figure 3.11: Side view of the trench structure for inspecting the fabricated structures.

3.3 Optimization procedure

In this section we will write about the optimization of the shape and dimensions of the grating grooves.

There are many parameters which can be controlled while milling the structures by a FIB. First of all, we need to write about the FIB parameters like the objective voltage, condenser lens voltage, and many more. The first attempts were made by making the best possible focus of the FIB picture. The profiles were reasonable and the result is shown in Figure 3.12.

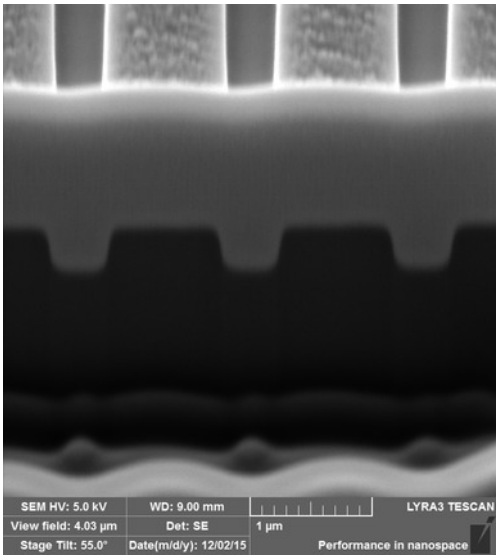

Figure 3.12: The grating milled after focusing optimization.

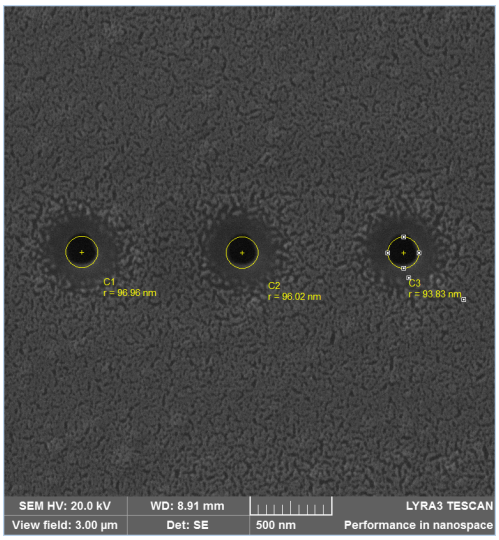

Figure 3.13: Optimized spots for 100 μm aperture with measured radius.

Another approach used by us nowadays is the following. There are presets of the parameters made for every aperture in the system. There are 5 apertures used to shape the beam and control its diameter. The position of this variable aperture in the system is shown in Figure 3.2. For every aperture, a milling test was made by applying pulses on a single spot of the silicon nitride membrane. The best circular shape was found and the parameters of the beam were written in the preset. This makes our structures more reproducible. The aperture sizes are 20, 50, 100, 200 and 400 μm. Larger apertures can be used for quicker milling of larger areas but they are not precise enough for our needs. The FIB spot size depends on the aperture. The diamaters of the spot are approximately 140, 260, 200, 400, and 760 nm. Figure 3.13 shows the final optimized spots for a 100 μm aperture preset, which was selected as good compromise between milling speed and spatial resolution. This preset was also used for the platinum deposition. The presets are numbered 1-5 according to the aperture used. 20 μm aperture is used in preset 1, 50 μm aperture is used in preset 2 etc.

An in-situ calibration procedure was performed for each fiber facet grating. A grating with three grooves with selected parameters and length of 7.5 μm was inscribed close to outer perimeter of the fiber. The procedure of Pt deposition and trench milling described in the subsection 3.2.3 is used to examine the fabricated grooves shape and dimensions. We can see the grating cross-section which is shown in Figure 3.12. We measure the dimensions and shape of the fabricated grating grooves and make corrections. We iterate to selected dimensions. Then we fabricate the final grating and after it we fabricate another testing grating to see how different is the final shape and dimensions.

Another parameter which can be controlled is exp-factor. This factor means how much overlap the the beam with another point of impact. The value of 1 means that trace is touching by its edge, the 0.5 means that the edge of the one trace is in

the middle of second trace. The Figure 3.14 shows the meaning of the exp-factor. Optimization process shows that value of 0.5 is best for our structures.

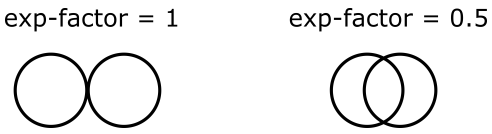

Figure 3.14: The exp-factor explanation drawing.

The procedure of milling has two possibilities called milling and polishing. During the milling process the layers from top of the groove to the bottom are milled out. During the polishing process the slices from the start of the groove to the end are milled out. There should be better shape of the groove by using polishing process. But we experienced a lot of the back-sputtering of the milled material. Then we tried to combine these two milling methods together but the result was not satisfactory and we ended by using milling process.

Last parameter we tested is beam trace path during the milling. There are four possible traces. Zig-zag, lines with fly-back, spiral-in and spiral-out. The traces are demonstrated in Figure 3.15. The zig-zag trace produced the best results and it was selected for our fabrication purposes.

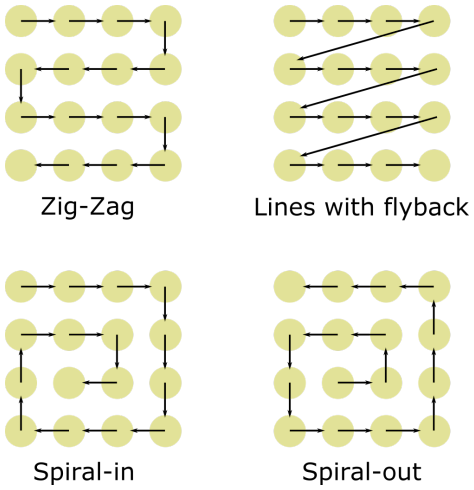

Figure 3.15: The FIB traces while fabricating structures.

In summary after testing various parameters we ended up using 100 μm aperture preset, 0.5 exp factor, milling process and zig-zag beam trace. Starting point of the milling parameters optimization is shown in Figure 3.16 and final grating structure is shown in figure 3.17.

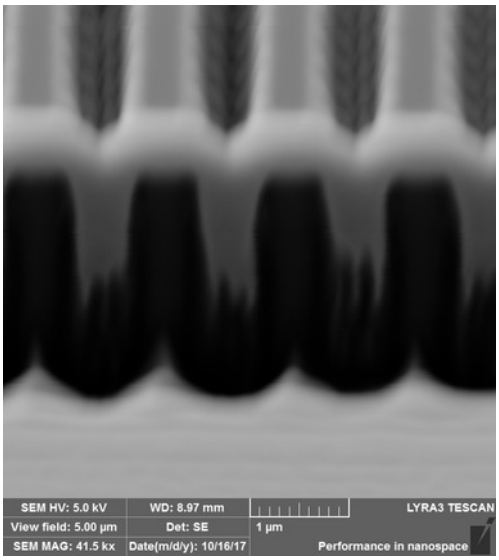

Figure 3.16: Starting point of the milling iterations.

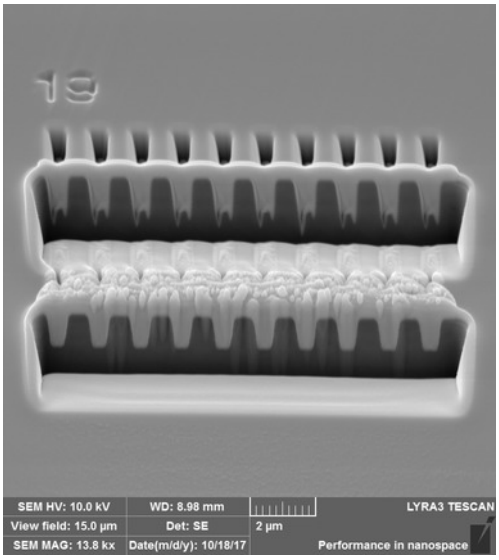

Figure 3.17: Grating structure after milling parameters optimization (lower of the milled structures).

3.4 Anti-reflection structures

In this section we will explain the fabrication of the AR structure described in the subsection 1.2.1. The optimized parameters of the structure are shown in Table 1.3. For the easier fabrication and consecutive measurement we used smf28 fibers. There is no need to open whole vacuum chamber to load smf28 fiber samples into the Tescan Lyra 3 machine which shortens the process. Also the fabricated structures can have smaller area because the core of the smf 28 fiber is smaller than the one in the FUD 3716. The measurement process after fabrication is also easier because we can use many devices from telecom industry. The measurement devices for smf28 fibers at central wavelength 1550 nm are widely available.

We fabricated structures optimized in the subsection 1.2.1. We also tested fabrication of the 2D periodic structures. We used smf28 fibers for fabrication process testing because it was less time demanding than using FUD 3716 fibers.

Table 1.3 lists the numerically optimized parameters of the AR gratings we fabricated. As mentioned above, we fabricated a grating for the smf28 fiber. Table 3.1 gives the designed parameters and Table 3.2 gives the measured parameters of the fabricated grating. The area of the grating is designed to be 20 μm x 20 μm with its centre in the centre of the fiber core.

Table 3.1: Designed parameters for milling the low reflecting structure.

Grating	**Λ** [nm]	**h_1** [nm]	**Fill factor**	**Width** [nm]
AR smf28	980	330	0.3	686

Table 3.2: Measured parameters of the low reflecting structure before and after fabrication. Fiber notation 2.1 refers to the fabricated parameters of the test grating before the fabrication and 2.2 refers to the test grating fabricated parameters after the fabrication.

Grating	**Fiber**	**Λ** [nm]	**h_1** [nm]	**Width** [nm]
AR smf28	2.1	982	344	683
AR smf28	2.2	976	312	768

The sputtering anti-charging technology was not used in this fabrication process. Only compensation with the electron beam was used. The current from the electron beam was set by the limiting aperture to its maximal value. This setting can not be used for imaging but it works for our purpose. During the operation of the FIB we let the electron beam probe the sample to compensate for the positive charge of the gallium ions. The schematic drawing in Figure 3.3 shows the geometry where both the FIB and SEM were operating at the same time while inscribing the grating. This resulted in a shift between the starting and ending grating parameters. This shift was caused by the system instability, mainly the ion gun. This grating was fabricated before the ion gun was replaced by the new Cobra ion gun. The grating profiles before and after the inscription of the grating are shown in Figures 3.18 and 3.19 respectively.

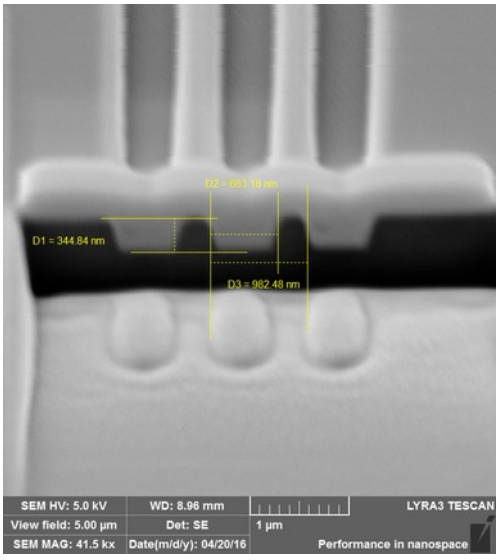

Figure 3.18: Cross-section of the calibration grating before inscription of the AR grating.

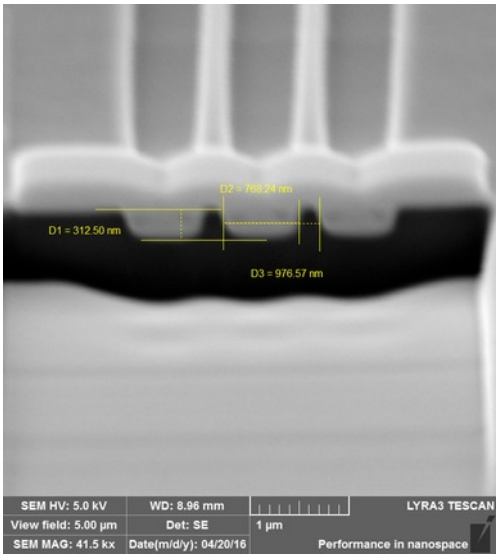

Figure 3.19: Cross-section of the calibration grating after inscription of the AR grating.

Figure 3.20 gives a top view of the fabricated AR grating with the measured dimensions. We can compute the period of the fabricated grating to double check the measurements of the testing gratings. The result is 978 nm, which is in good agreement with designed value. The whole fiber facet with inscribed AR grating

is shown in Figure 3.21. To achieve the stability of the ion gun before replacing we needed to run the FIB for approximately one hour and then we had stability for another hour to the fabricate the designed structures. An illustration of the instability is shown in Figure 3.22, where the AR grating was fabricated. The fabrication process went from left to right with the same parameters entered into the system. The non-uniformity of the grating is revealed by milling the wedge trench along the bottom edge of the structure.

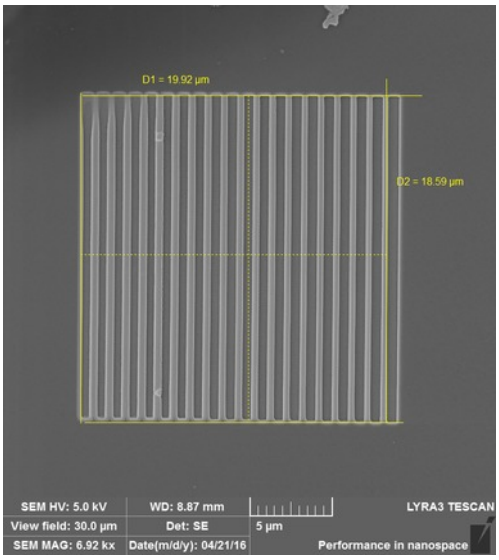

Figure 3.20: Top view of the smf28 fiber facet with inscribed AR grating. The dimensions show good agreement with the wanted 20 μm $\times$ 20 μm area and period of the grating 980 nm.

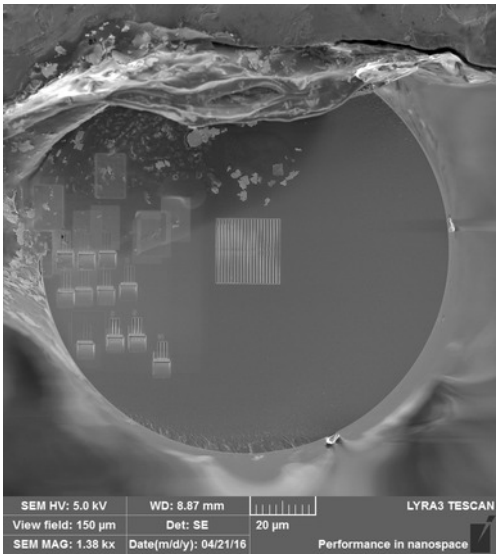

Figure 3.21: Top view of the smf28 fiber facet with inscribed AR grating and area with calibration gratings.

We also performed a test to investigate the FIB induced damage to the surface of the fiber facet. The fabricated structure is just a simple circular hole with centre corresponding with the centre of the fiber core. The test was run on the fiber with 50 nm of chromium deposited. The diameter of the fabricated structure was 40 μm and its depth was 330 nm to simulate the AR grating fabrication process and to be sure all the chromium was milled out. A view of the fabricated structure is in Figure 3.23. The results from this test are discussed in Section 4.1.

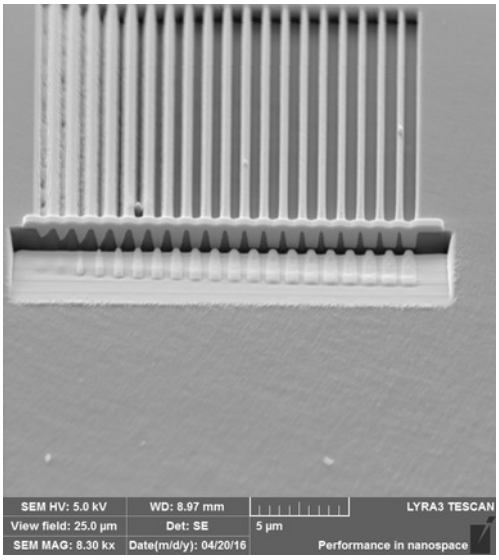

Figure 3.22: AR grating fabricated during unstable operation of the ion gun.

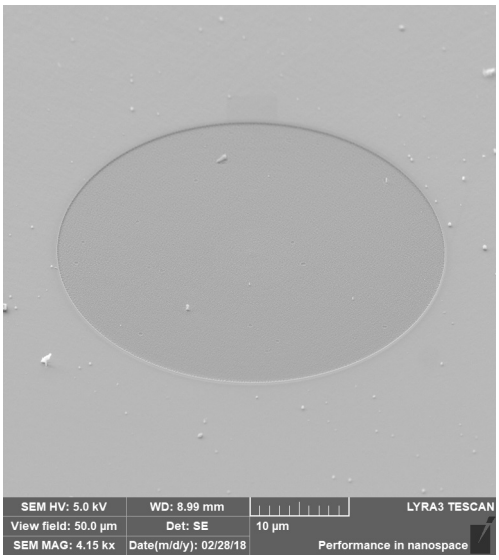

Figure 3.23: Circular structure inscribed on the smf28 fiber facet to investigate FIB induced damage.

3.5 Low reflecting structures

In this section we will explain the fabrication of the structure with low reflectance described in subsection 1.2.2. The structural design parameters are shown in Table 3.3. We used the optimized FIB parameters that were described in Section 3.3. The fibers used for the fabrication were Nufern PLMA-GDF-25P/400-10FA (FUD 3716). They can not be bent in the same radius as smf28 (which are thinner). This results in the need to open the whole vacuum chamber to load the holder with the fiber in the Lyra3 machine. The holder with the fibers secured by conductive vacuum adhesive tape is shown in Figure 3.4. The chamber was then pumped overnight to a working chamber pressure of around 7×10^{-5} Pa.

Table 3.3: Designed parameters for milling the low reflecting structure. Grating names E11 and E14 refers to two set of optimized parameters of the low reflecting polarization sensitive grating.

Grating	**Λ** [nm]	**h_1** [nm]	**Fill factor**	**Width** [nm]
E11	1290	710	0.7	387
E14	1290	700	0.65	451

First of all, the fibers were checked by the electron microscope and photos were taken. This was in order to see whether the fiber facets had electrical contact with the silver paste and whether the platinum could be deposited. Also we checked for any damage or problems with the fibers.

Table 3.4 shows the test grating parameters before and after milling for the final grating across the fiber core. To position the grating directly across the core one

Table 3.4: Measured parameters of the low reflecting structure before and after fabrication. Grating names E11 and E14 refers to two set of optimized parameters of the low reflecting polarization sensitive grating. Fiber notation 2.1 refers to the fabricated parameters of test grating before the fabrication and 2.2 refers to the test grating fabricated parameters after fabrication. Fiber notation 5.1 and 5.2 use the same naming convention.

Grating	**Fiber**	**Λ** [nm]	**h_1** [nm]	**Width** [nm]
E11	2.1	1280	710	390
E11	2.2	1290	690	390
E14	5.1	1300	700	460
E14	5.2	1300	700	470

can use FIB imageing. The core is clearly visible in image produced by FIB. The fabricated grating E11 was selected to test in the thulium doped fiber laser. The testing procedure will be described in Section 4.2.

3.6 High reflecting structures

In this section we will write about the fabrication of the high reflection grating in the Ta_2O_5 and HfO_2 layer. There is an additional step in the preparation: after the deposition of the oxide we have to make contact between the fiber facet and the silver paste. The designed dimensions of the structures are listed in Table 3.5.

Table 3.5: Designed parameters for the milling the high reflecting structure.

Grating	**Λ** [nm]	**h_1** [nm]	**Fill factor**	**Width** [nm]
HighR 25P/400	1280	840	0.62	490

Table 3.6: Measured parameters of the low reflecting structure before and after fabrication. Fiber notation 2.1 refers to the fabricated parameters of test grating before start of the fabrication and 2.2 refers to the test grating fabricated parameters after fabrication process.

Grating	**Fiber**	**Λ** [nm]	**h_1** [nm]	**Width** [nm]
HighR 25P/400	2.1	1280	840	480
HighR 25P/400	2.2	1290	840	490

First of all the fibers have to be checked for cracks at the layer and how they can be put into electrical contact. Figures 3.24 and 3.25 show a layer in good condition and a layer with a crack.

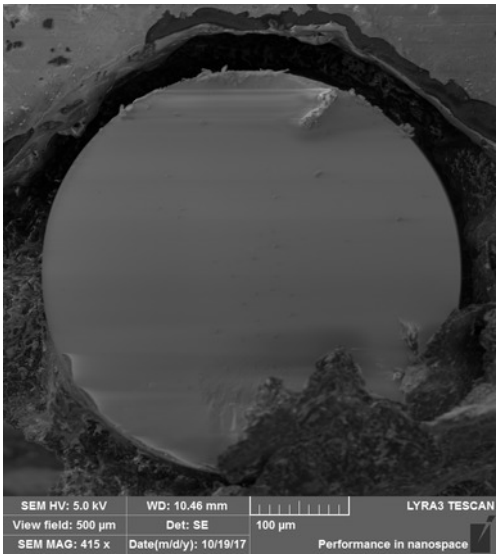

Figure 3.24: Top view of the fiber facet with Ta_2O_5 layer.

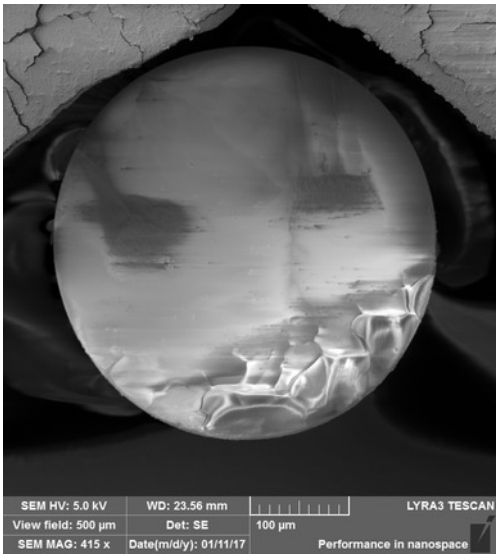

Figure 3.25: Top view of the fiber facet with cracked Ta_2O_5 layer.

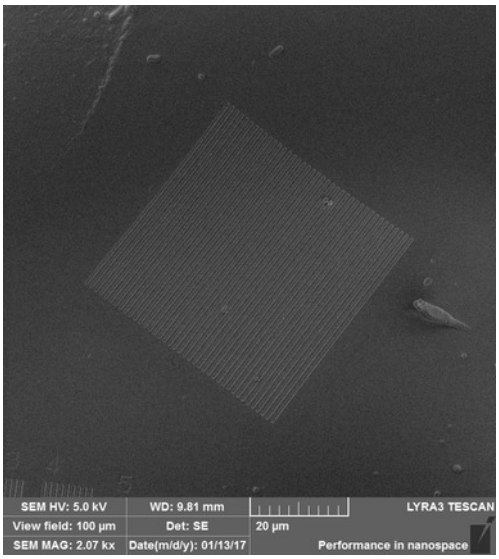

Figure 3.26: Top view of the fiber, holder position 2, view field 100 μm.

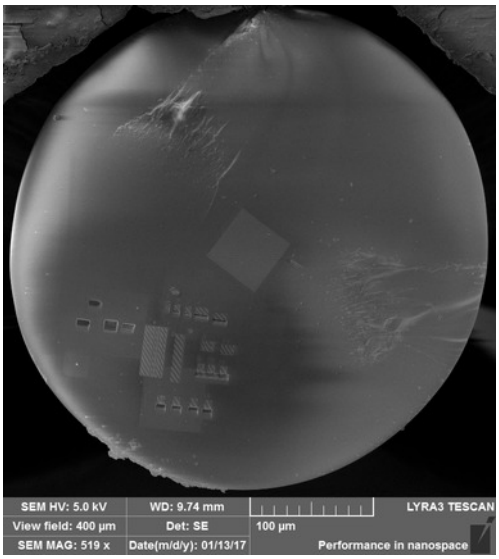

Figure 3.27: Top view of the fiber, holder position 2, view field 400 μm.

Then the optimization of the dimension of the grating grooves must be carried out. The dimensions of the fabricated grating are shown in Table 3.6. The average current was around 155 nA (using preset 3). Only weak charge compensation by the electron beam was used (300 pA, speed 1, beam intensity 14). Electron microscope photos of the fabricated grating are shown in Figures 3.26–3.28. An optical microscope photo is shown in Figure 3.29.

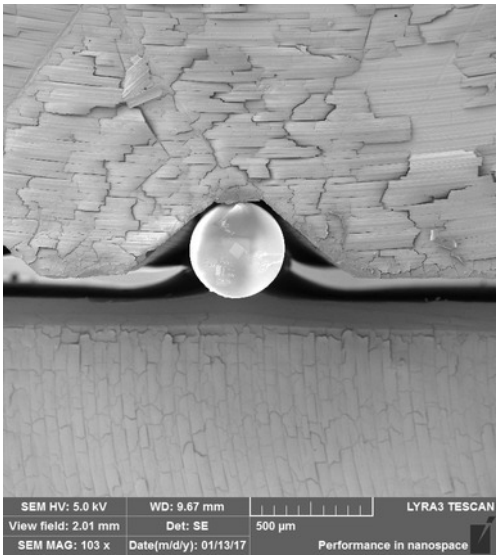

Figure 3.28: Top view of the fiber, holder position 2, view field 2009 μm.

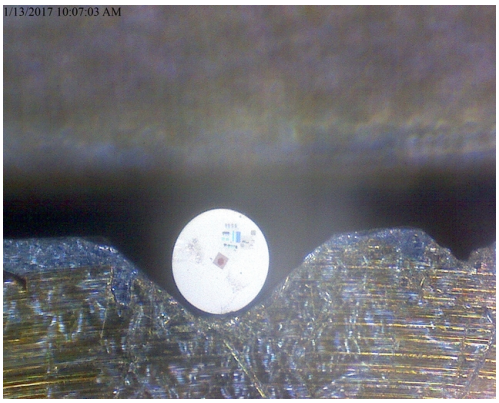

Figure 3.29: Top view (optical microscope) of the fiber, holder position 2.

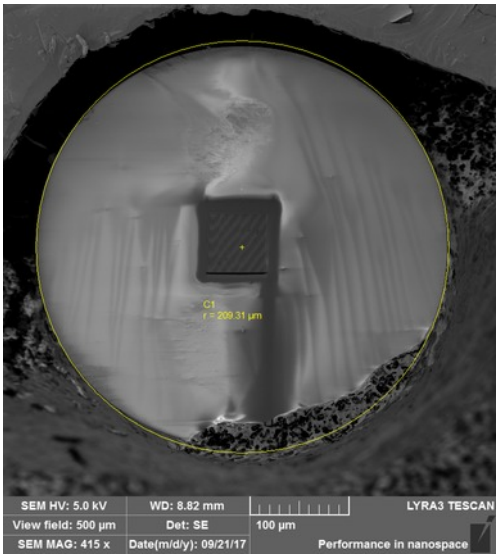

Figure 3.30: Top view of the optical fiber facet with measured radius using circle tool to measure.

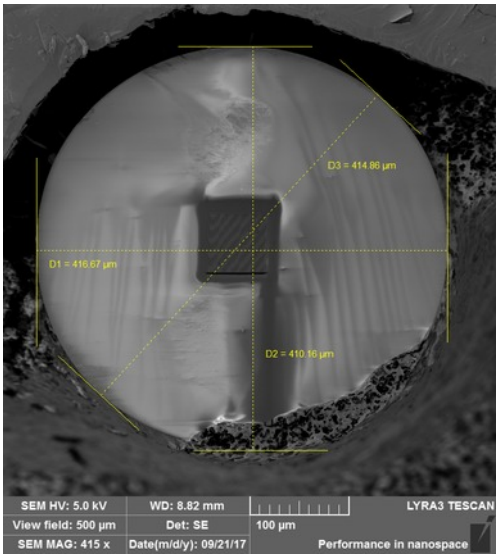

Figure 3.31: Top view of the optical fiber facet with measured diameter using linear tool to measure.

Finding the correct position for milling the grating is much more challenging because the core is not visible under the deposited layer. We can use only a 400 μm view field by the FIB, and while the fiber should have the same diameter, it can vary depending on the tolerances, so there can be a problem getting the whole fiber in the picture. We measured the fibers we are using and discovered they have a

diameter larger than 400 μm, which is shown in Figures 3.30 and 3.31.

Fabrication of one grating takes approximately 1 hour 45 min plus the time needed to find the proper settings. These gratings have dimensions 40x40 μm. There were a few gratings that did not cover the entire fiber core. All the following gratings were fabricated in the dimension of 80x80 μm which takes approximately 7-8 hours. This imposes huge requirements on the stability of the FIB. We could not achieve this stability until our gallium ion source was replaced by the new Cobra ion gun. The Cobra source can achieve the stability for the time needed to fabricate the gratings. The fabricated gratings were tested in the thulium fiber laser. The test is described in Section 4.3.

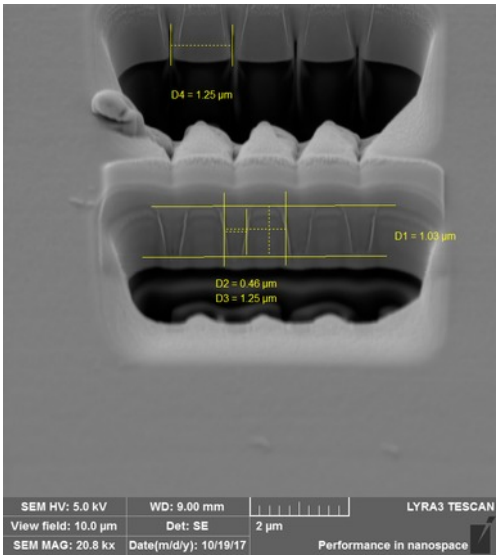

Figure 3.32: The first calibration grating cross-section.

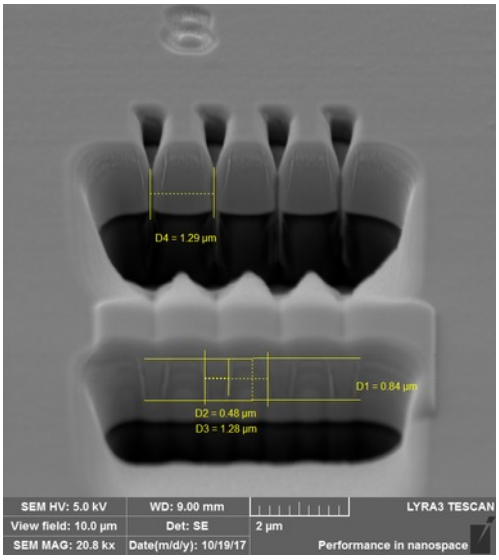

Figure 3.33: The last calibration grating cross-section.

The profile of the gratings with parameters optimized in subsection 1.2.3 were fabricated and the calibration profiles are shown in Figures 3.32 and 3.33. The figures present a comparison between using platinum for groove shape measurement and not using it. There is a huge difference and there is a visible re-deposition of the milled material and distortion of the shape. According to the tests, the gratings and their damage described in Section 4.3 and charging testing, we used the platinum fence around the final grating area. The testing of the shape was performed at the place where the charging was overcome by the platinum layer. The result of the grating fabrication is shown in Figures 3.34, 3.35 and 3.36. One can easily see that we found the period is lower then we set, and the compensation was not enough. The resulting period is approximately 1250 nm. The grating used for the tests was fabricated with period of 1280 nm.

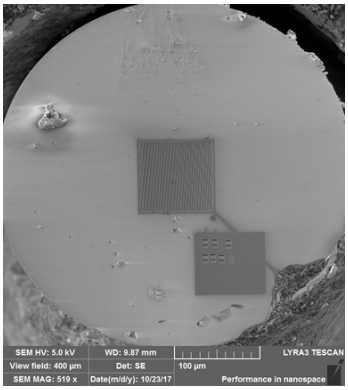

Figure 3.34: Top view of the fabricated grating, view field 400 μm.

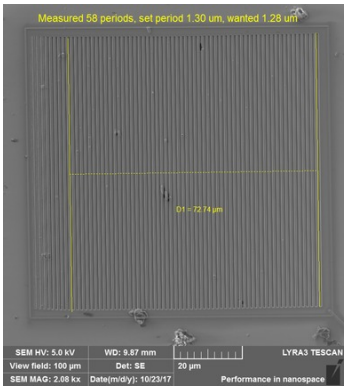

Figure 3.35: Top view of the fabricated grating, view field 100 μm.

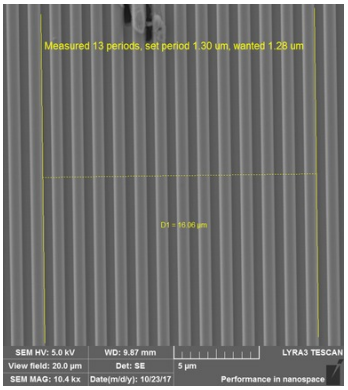

Figure 3.36: Top view of the fabricated grating, view field 20 μm.

3.7 2D structures

In this section we will present the fabrication of the 2D structure using chromium deposition to prevent charging. The structure is a 2D rectangular grid of circular holes. The weak spot of this structure are the walls between holes. They can collapse when the circular holes are too close. We used the same period of the structure as for the 1D AR diffraction grating, namely, 980 nm, and optimized the diameter of the circular holes to achieve solid walls between the holes. When we used a diameter larger than 500 nm, the walls collapsed in the X- and Y-directions of the fabrication, which resulted in the structure of the standalone pillars shown in Figure 3.37.

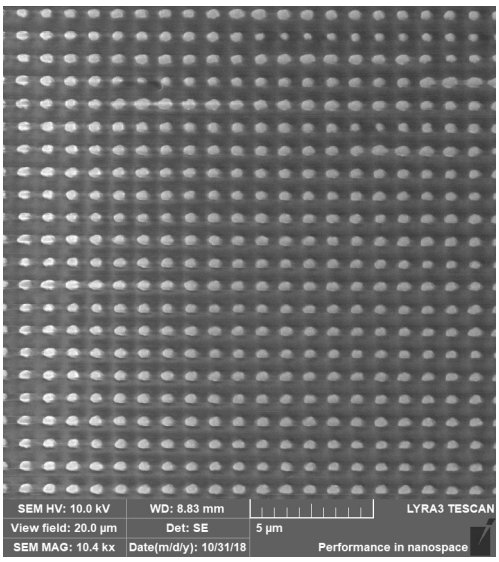

Figure 3.37: Top view of the smf28 fiber facet with inscribed 2D structure without walls between holes. Final structure consists of standalone pillars.

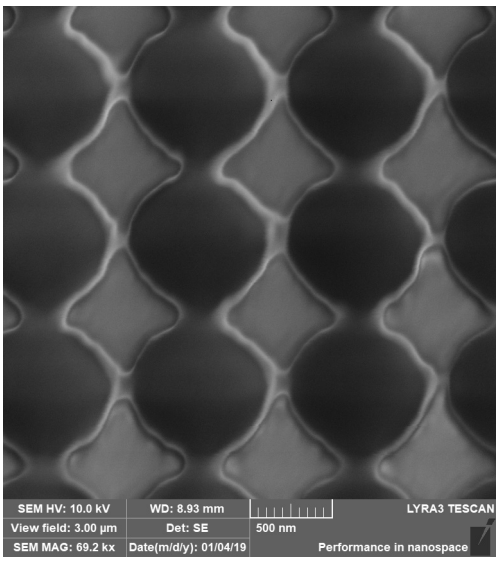

Figure 3.38: Top view of the smf28 fiber facet with inscribed 2D structure with partial walls between holes. Only walls in the Y-direction are collapsed.

Decreasing the diameter of the fabricated structure to 400 nm resulted in solid walls in the X-direction but collapsed walls in the Y-direction. The fabricated structure is shown in Figure 3.38. We investigated the behaviour of the FIB system in the X- and Y-directions, because the set period of the structure was identical in these perpendicular directions. A correction factor for the Y-axis needs to be implemented to achieve symmetrical behaviour.

The rectangular grid structure shown in Figure 3.39 was not the only one fabricated. We also tried a hexagonal structure with a hole in the centre of hexagonal grid, which is shown in Figure 3.40. The diameter of the circular holes is 340 nm. The area of the fabricated structures is approximately 40 μm $\times$ 40 μm. The rectangular structure is shown in Figure 3.41 and the the hexagonal structure is shown in Figure 3.42. The whole fiber facet with inscribed rectangular structure is shown in Figure 3.43 and with hexagonal structure is shown in Figure 3.44. We demonstrated the capability of FIB technique to fabricated complex 2D structures. More optimization is needed to examine the different behaviour in the X- and Y-directions. There is still open possibility to use this technique in the research further.

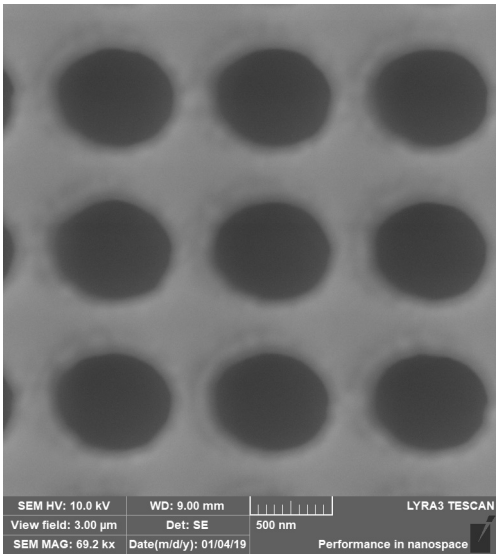

Figure 3.39: Top view of the rectangular 2D structure with view field 3 μm.

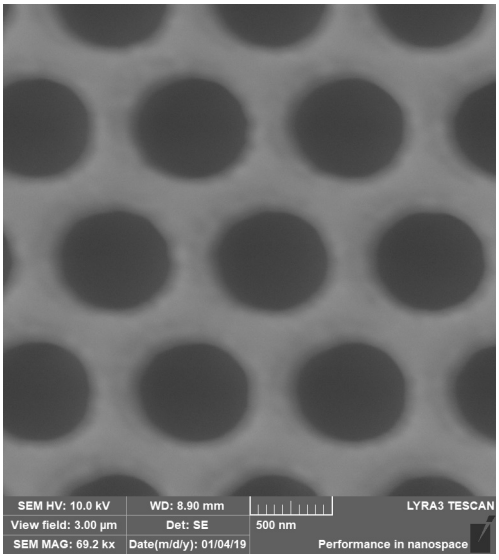

Figure 3.40: Top view of the hexagonal 2D structure with view field 3 μm.

In this section we introduced the fabrication process of the fiber facet diffraction structures. First, the electron microscopy and FIB processes were described. Then we investigated ways to solve the charging issue by the use of AquaSave conductive polymer, direct Pt deposition in the FIB-SEM machine, and chromium layer sputtering before the fabrication. We described in detail the optimization procedure we used to determine the design parameters for the structure. At the end we described the fabricated anti-reflection, low reflecting, high reflecting and 2D structures.

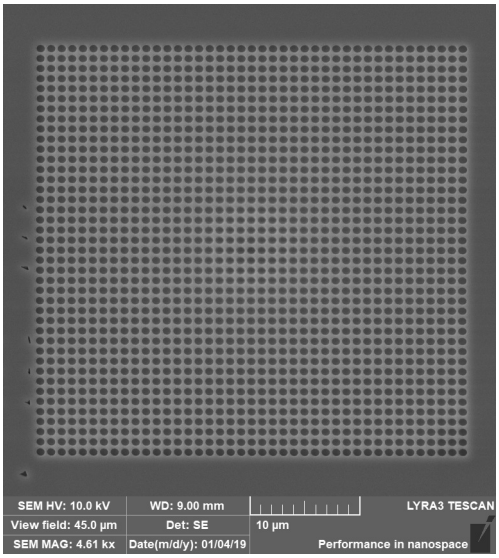

Figure 3.41: Top view of the rectangular 2D structure with view field 45 μm.

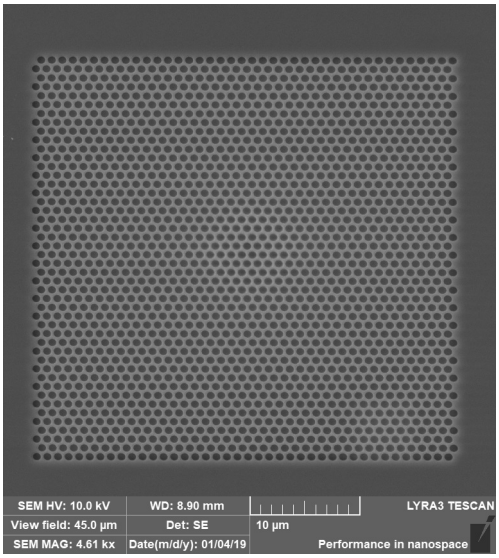

Figure 3.42: Top view of the hexagonal 2D structure with view field 45 μm.

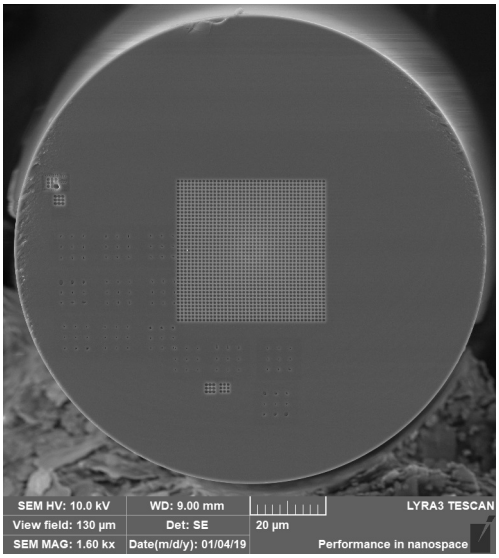

Figure 3.43: Top view of the rectangular 2D structure with view field 130 μm.

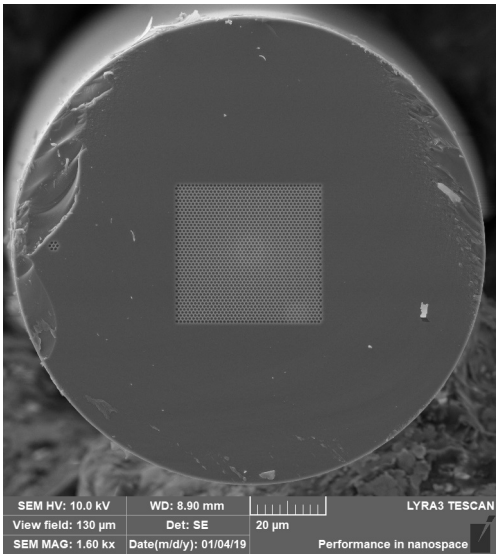

Figure 3.44: Top view of the hexagonal 2D structure with view field 130 μm.

Chapter 4

Testing the fabricated structures

In this chapter we will introduce and explain the measurement and testing of the fabricated diffraction gratings.

4.1 Anti-reflection structures

The anti-reflection structures were tested using telecommunication wavelength 1550 nm and therefore the fibers used were SMF28. A scheme of the setup is shown in Figure 4.1. The Agilent 8164B lightwave measurement system with tunable laser source and three detectors was used. The Agilent 81600B laser source can be tuned from 1495 nm to 1640 nm. The detectors fitted into the mainframe of the lightwave measurement systems were 81634B denoted by det 1 and 81635A double channel denoted by det 2.1 and det 2.2. Lastly, we used a Thorlabs integration sphere S148C with PM100A laser power meter console. The fibers with fabricated AR structures were approximately one meter long and were spliced to patch-cords with FC-APC connectors. FC-APC connectors were used in the whole setup to suppress back-reflection in the connectors. Det 1 was used to measure the back-reflected power from the AR structure. This detector is very sensitive and is capable of detecting signals of -110 dBm. The det 2.1 and 2.2 detectors are not that sensitive, only up to -80 dBm. Therefore, det 2.1 was used to monitor the output power of the tunable laser source.

The whole measurement setup from Figure 4.1 is automatic using Labview code to drive the measurement. The wavelength step was set to 1 nm resolution. Including delays to let the wavelength and power stabilize after tuning, the time needed to measure one sample exceeds one hour. The measurement setup was tested one component at a time to determine its transfer function, which is necessary for data analysis. Firstly we investigated the laser power over the whole range of wavelengths. We set the laser power to 0.1 mW and 1 mW respectively. The results of this investigation are in Figure 4.2. For every later measurement, we set the power to 1 mW. Figure 4.3 gives the results from testing the isolator in forward (not-isolating) and backward (isolating) orientations. The backward orientation was checked to be sure no damage will be caused to the laser by back-reflected light. According to the 50:50 coupler connection in the measurement setup, we need to determine the transfer functions listed in Table 4.1. The setup scheme for the measurement of the 50:50 coupler transfer function is in Figure 4.4.

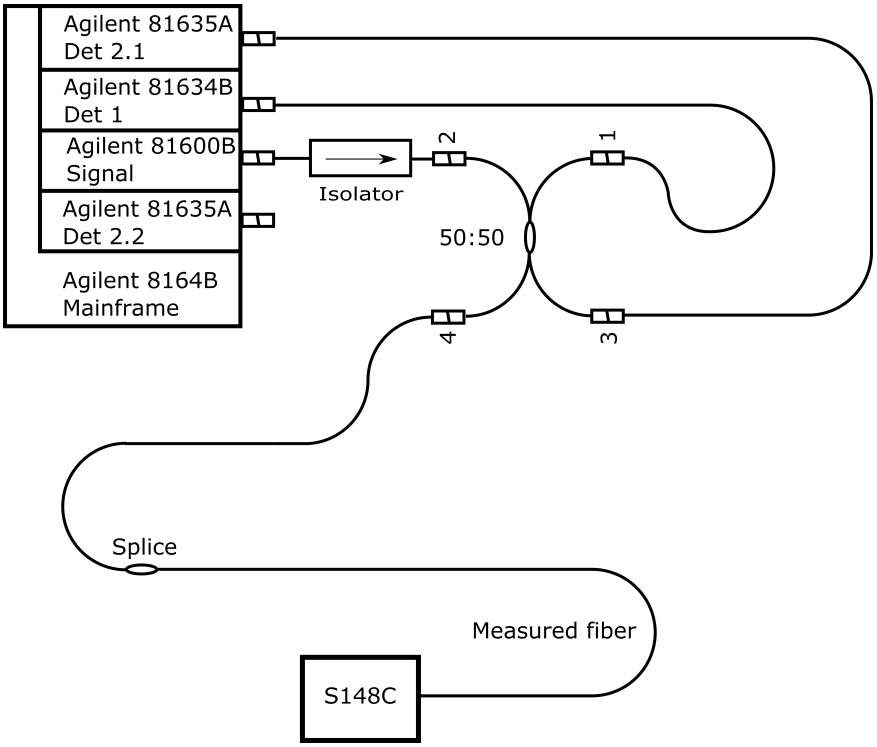

Figure 4.1: The AR test setup. Agilent 8164B lightwave measurement consists of tunable laser (Agilent 81600B 1495–1640 nm) source and three detectors (81634B - det 1, 81635A - det 2.1). 50:50 coupler with ports numbered 1-4 and isolator are connected. The measured fiber is connected to the port 4 of 50:50 coupler. Transmitted power is measured by a Thorlabs integration sphere S148C with PM100A laser power meter console.

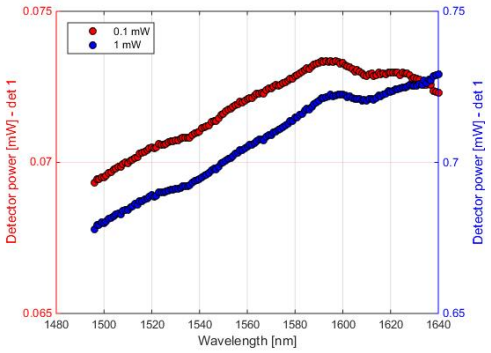

Figure 4.2: Laser power test over the range 1496 nm to 1640 nm.

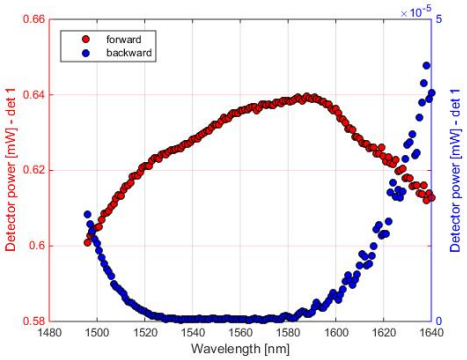

Figure 4.3: Isolator test in forward and backward directions.

For the measurement of the sample reflection transfer function, the setup was reconnected and the laser source was connected to port 4 and det 1 to port 1. The results from this measurement are in Figure 4.5. The setup was calibrated using a Thorlabs integration sphere S148C, which was calibrated by the manufacturer.

Table 4.1: Identifications and directions of the characterized transfer functions of the 50:50 coupler.

Name	Input	Output
Power monitor	2	3
Sample probe	2	4
Sample reflection	4	1

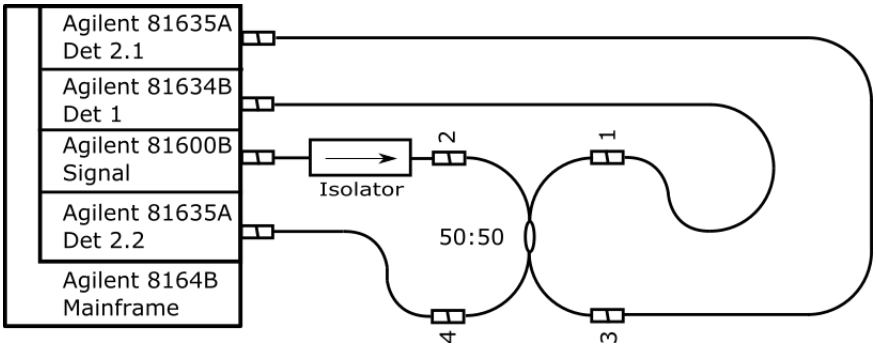

Figure 4.4: Test setup for measuring transfer functions of the 50:50 coupler for sample probe and power monitor. Agilent 8164B lightwave measurement consists of tunable laser (Agilent 81600B 1495–1640 nm) source and three detectors (81634B - det 1, 81635A - det 2.1 and set 2.2). 50:50 coupler with ports numbered 1-4 and isolator are connected.

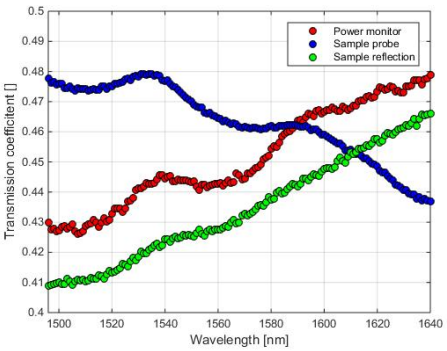

Figure 4.5: Transfer function of the 50:50 coupler in power monitor, sample probe and sample reflection directions.

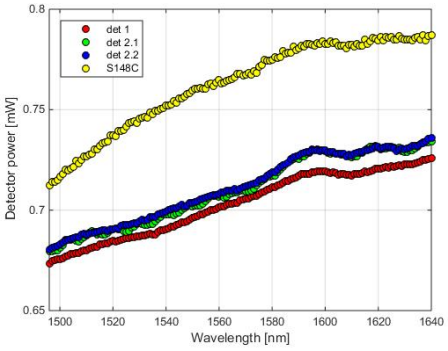

Figure 4.6: Calibration of the detectors in the Agilent 8164B lightwave measurement system. The detectors were 81634B, denoted by det 1, 81635A double channel denoted by det 2.1 and det 2.2 and Thorlabs integration sphere S148C with PM100A laser power meter console.

Figure 4.6 shows the relation between the power detected by det 1 and the integration sphere while measuring the coupler transfer function. We also carried out a repeatability test when connecting and reconnecting the whole setup. The results of the repeatability test are in Figure 4.7 for the power monitor and in Figure 4.8 for the sample probe.

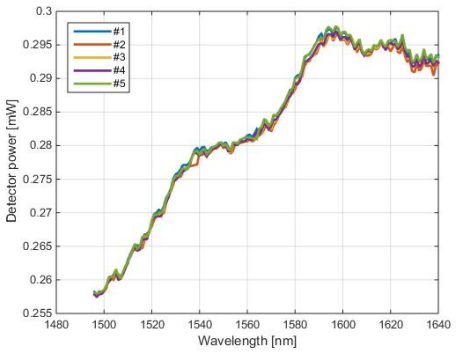

Figure 4.7: Repeatability test of the measurement setup for the power monitor direction.

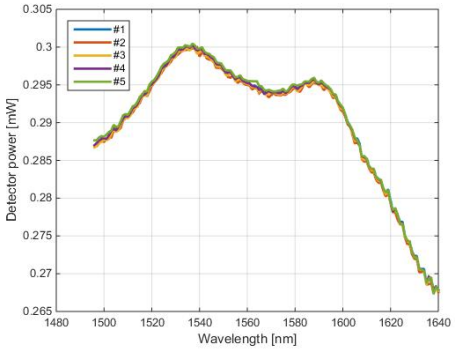

Figure 4.8: Repeatability test of the measurement setup for the sample probe direction.

We measured this for cleaved fibers for the sake of comparison. These results are shown in Figure 4.9. We tested the structure described in subsection 3.4 shown in Figure 3.23 to investigate the influence of the FIB machining process on the fiber facet. From the results shown in Figure 4.10, we can see that it was possible that there was damage which decreased the transmission. From Figure 3.23 we can see that the surface of the fabricated hole is rough, which could be the root of this problem.

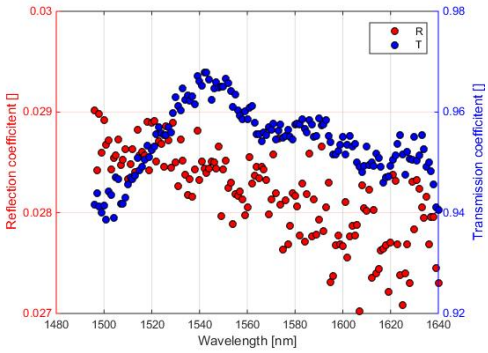

Figure 4.9: Reflection and transmission coefficient of cleaved smf28 fiber.

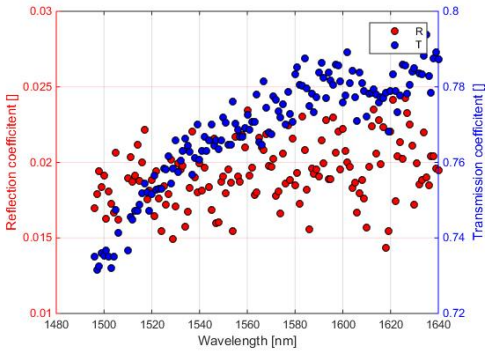

Figure 4.10: Reflection and transmission coefficient of FIB induced damage to the testing structure fabricated on the smf28 fiber facet.

We needed to etch the Cr layer to achieve the transmission and reflection which was expected from the Ar structure. We tried various etchants, such as KOH and HCl, with high etching times up to one hour. We had no success with these etchants. The etchant which actually works is Chromium etchant 651826 from Sigma Aldrich.

The evolution of the transmission and reflection coefficient while increasing the etching time with Chromium etchant 651826 is shown in Figures 4.11 and 4.12 respectively.

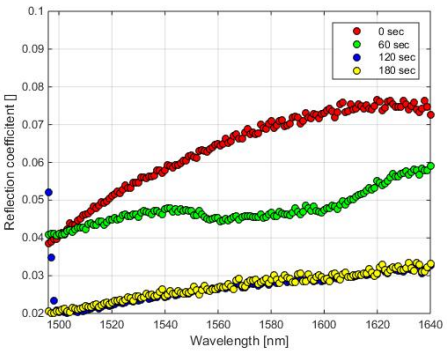

Figure 4.11: Reflection coefficient of FIB induced damage testing structure evolution while increasing etching time.

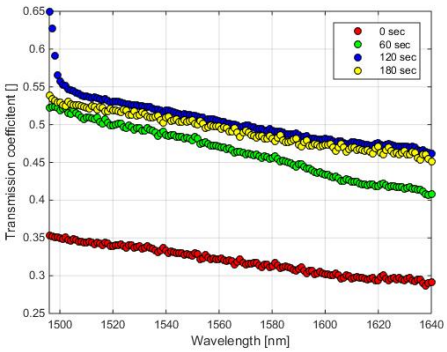

Figure 4.12: Transmission coefficient of FIB induced damage testing structure evolution while increasing etching time.

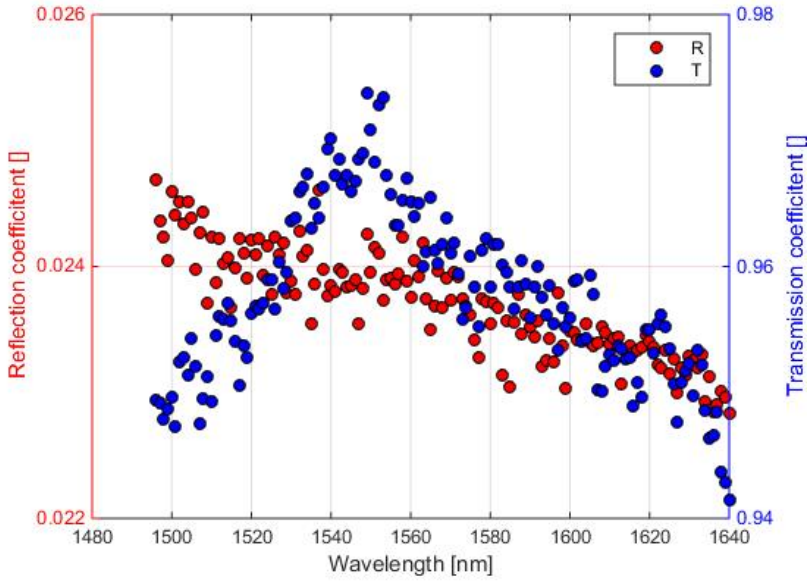

Figure 4.13: Transmission and reflection coefficient for the fiber facet with etched chromium layer.

After the etching, the fiber facet was rinsed with deionized water to remove any residues. We also cleaned the fiber tip before each measurement, with isopropyl alcohol using an ultrasound cleaning machine, to ensure that no contamination is present while measuring. This test was run on the FIB-induced damage testing structure shown in Figure 4.10 because it was suspected that there might be some residual chromium present. From the results we can see that this hypothesis was

confirmed. While the reflection coefficient of this structure settled to be close to that of the cleaved fiber facet, the transmission coefficient remained lower. These losses can be explained by the absorption at the damaged surface together with the scattering of the light back to the fiber where it is not coupled to the core but radiated out. We also investigated the cleaved fiber with the sputtered chromium layer. The test showed that after 10 min of etching, all chromium is removed from the fiber facet. To ensure the correct results, the fiber from this test went through the same procedure as the fibers with the fabricated structures. It was in the same holder since the start of the process till its end. The results after the removal of the chromium layer are shown in Figure 4.13.

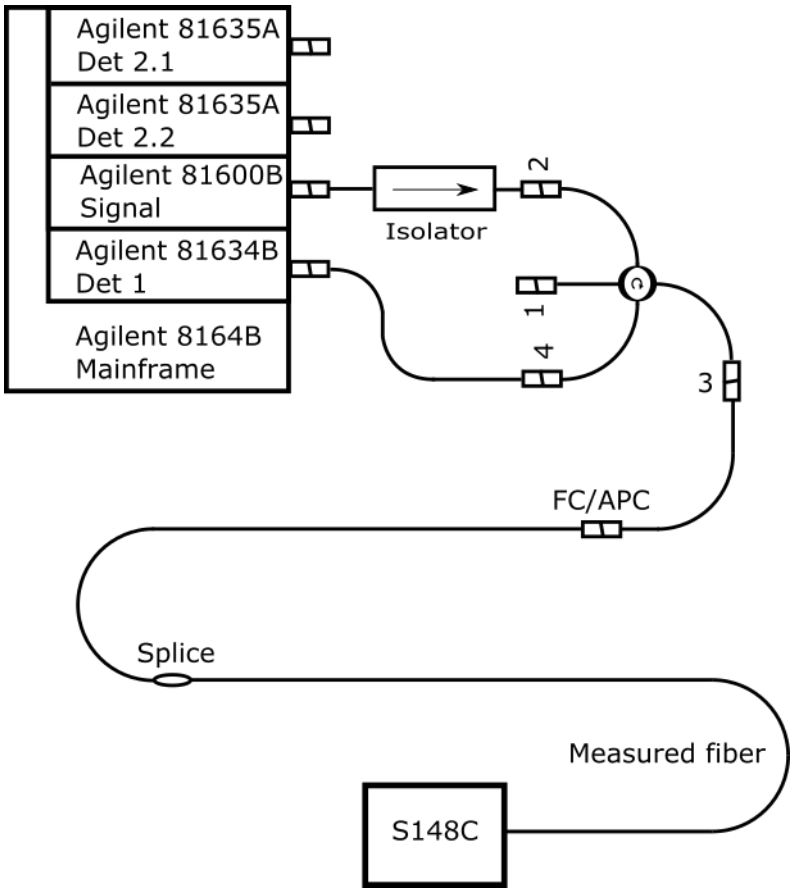

Figure 4.14: Measurement setup for the reflection and transmission with circulator. Agilent 8164B lightwave measurement consists of tunable laser (Agilent 81600B 1495–1640 nm) source and three detectors (here used only the 81634B - det 1). Transmission of the measured fiber was measured by Thorlabs integration sphere S148C with PM100A laser power meter console.

We tested the AR diffraction grating optimized as in subsection 1.2.1. The difference from the previous process is in the measurement setup. The setup is shown in Figure 4.14. The notation of the ports is the same as the manufacturer's. The logic behind this is that when we connect port 1 as input the output will be in port 2, etc. This setup has better sensitivity for the backreflected light than the setup with the 50:50 coupler but also has the drawback that we can not monitor the

output power of the signal laser. Therefore we have only a comparative measurement with the cleaved fiber. A comparison of the reflected and transmitted power is shown in Figures 4.15 and 4.16 respectively.

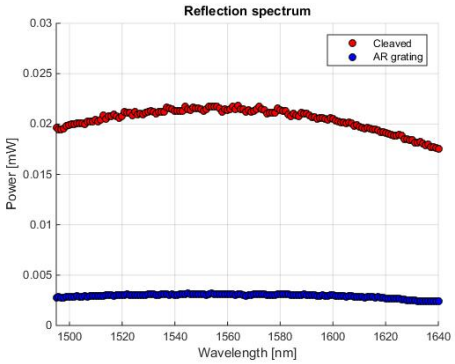

Figure 4.15: Experimental results of reflection coefficient spectra of AR grating.

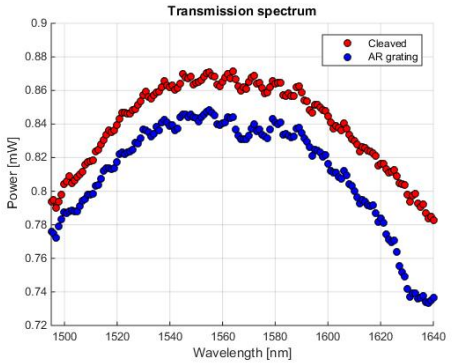

Figure 4.16: Experimental results of transmission coefficient spectra of AR grating.

4.2 Low reflecting structures

The low reflectivity polarization sensitive diffraction gratings were tested in a thulium-doped fiber laser. The fiber laser only involves PM fibers and PM pig-tailed optical components. The laser scheme is shown in Figure 4.17.

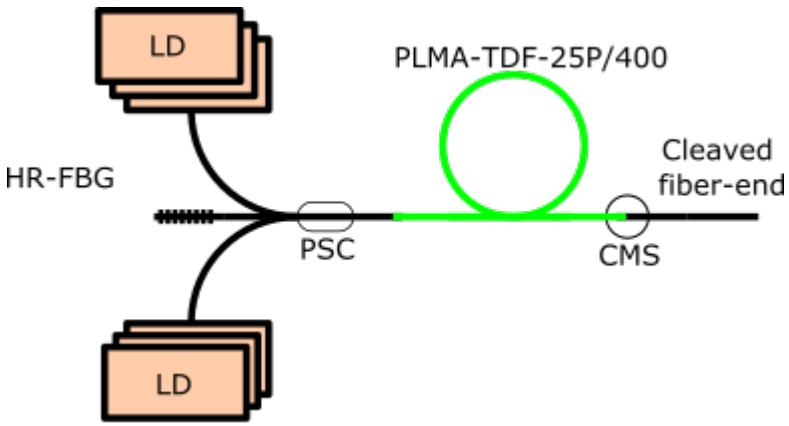

Figure 4.17: The thulium fiber laser setup. Highly reflective fiber Bragg grating (HR-FBG), pump signal combiner (PSC), active fiber (PLMA-TDF-25P/400), cladding mode stripper (CMS) and pump laser diodes (LD) were used to form thulium fiber laser setup.

The resonator consists of an active fiber (PLMA-TDF), pump–signal combiner (PSC), and high-reflectivity fiber Bragg grating (HR-FBG). The 35-W, 793-nm wavelength laser diodes from LIMO coupled to 220/280 μm multimode pigtails with numerical aperture of 0.22 were used as the pump source. In all, 6 pump diodes

were used. A double-clad thulium-doped PM fiber (PLMA-TDF-25P/400-HE from Nufern) with a large mode area and length of 5 m was used as an active fiber. The fiber has the following dimensions: core diameter = 25 μm, cladding diameter = 400 μm and coating diameter = 550 μm. The polymer coating has a lower refractive index than the fiber cladding, which means that pump light is guided in the fiber's inner cladding. The numerical apertures of the core and of the inner cladding are 0.09 and 0.46, respectively. The multimode pump absorption is 12 dB for a 5-m long fiber. The unabsorbed pump power is trapped in a cladding mode stripper. The CMS is splice covered with UV curable polymer with a higher refractive index than the fiber cladding itself. The pump–signal combiner has to be cooled to dissipate the heat from the pump not coupled to the resonator. A laser resonator is created between the high-reflectivity fiber Bragg grating spliced to the pump–signal combiner and a low reflectivity mirror in the form of a perpendicularly cleaved output fiber. The high-reflectivity fiber Bragg grating has a reflectivity of 99.6% at a wavelength of 2039 nm and reflection bandwidth of 1 nm. The output mirror has a reflectivity of 3.5%, as given by Fresnel's equations.

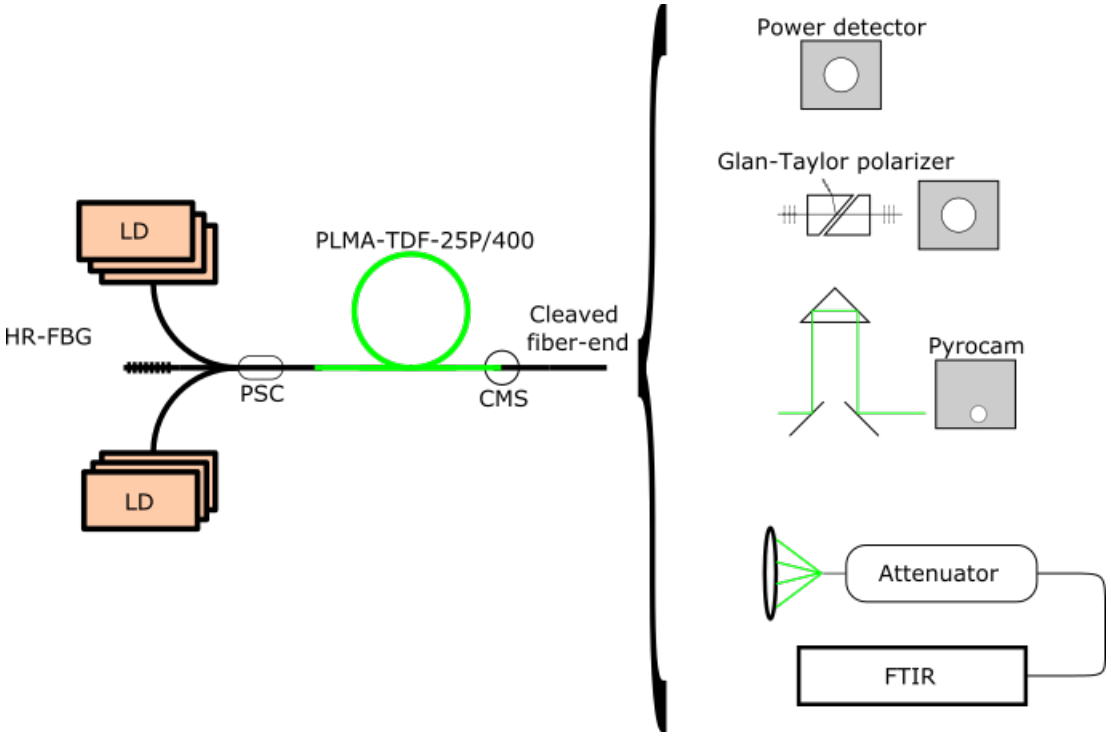

Figure 4.18: The scheme of the measurement setup for the characterization of the thulium fiber laser.

The output laser power was measured with a power meter from Gentec, which is suitable up to 100 W range. The polarization extinction ratio of the laser was determined using a Glan–Taylor polarizer and the beam quality factor was assessed by a pyro-electric camera (Pyrocam III) combined with a linear kinematic stage driven by a computer. The optical spectrum was recorded by a Fourier transform infra-red spectrometer (Nicolet 8700). The measurement scheme is shown in Figure 4.18. The pump power launched into the active fiber was measured at the output of

the pump–signal combiner as a function of the pump laser diodes' current during the construction of the laser before splicing the pump–signal combiner with the active fiber. The dependence of the laser output power on the absorbed pump power is shown in Figure 4.19.

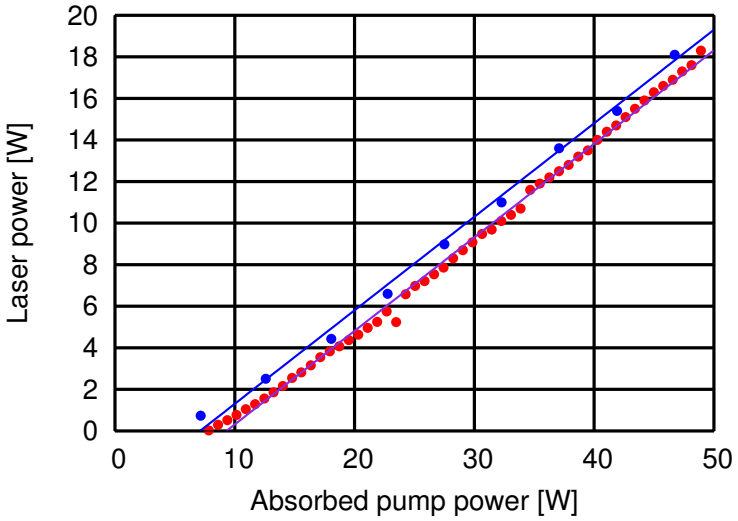

Figure 4.19: The laser power output. Red points: output of the laser with low reflecting grating. Blue points and line: output power of the laser with cleaved output.

The laser has a maximum output power of 18 W, threshold of 7.4 W, and slope efficiency of 42%. The slope efficiency is lower than the slope efficiency of lasers pumped directly through a high-reflectivity fiber Bragg grating [42]. We assume that this is due to the additional insertion loss of the pump–signal combiner. The M^2 beam quality parameter was determined using the setup described in Figure 4.18. Its value is 1.4, which means that higher order modes are present in the large mode area fiber used for the laser setup. The polarization extinction ratio of the laser beam was close to 1, which reflects the fact that no elements with significant polarization-dependent losses were included in the resonator.

After the characterization of the fiber laser with perpendicularly cleaved output fiber, we spliced the laser output fiber with a short (20 cm long) piece of the fiber, at the facet of which had been fabricated the diffraction grating which is shown in Figure 4.20. Figure 4.19 shows that the threshold slightly increased from 7.4 W to 9.9 W while the slope efficiency remained the same at 42%. These results correspond with the numerical simulations, where only a low diffraction loss is caused by the diffraction grating. The reflection from the grating for TE polarization corresponds with the reflection from the cleaved fiber facet while the reflection of the TM polarization is significantly suppressed. The polarization extinction ratio is defined by

$$\mathrm{PER} = 10log(P_{max}/P_{min}), \tag{4.1}$$

and was measured using a Glan–Taylor polarizer. Glan–Taylor polarizer transmits the p-polarized light while it reflects the s-polarized light. By rotating it along the

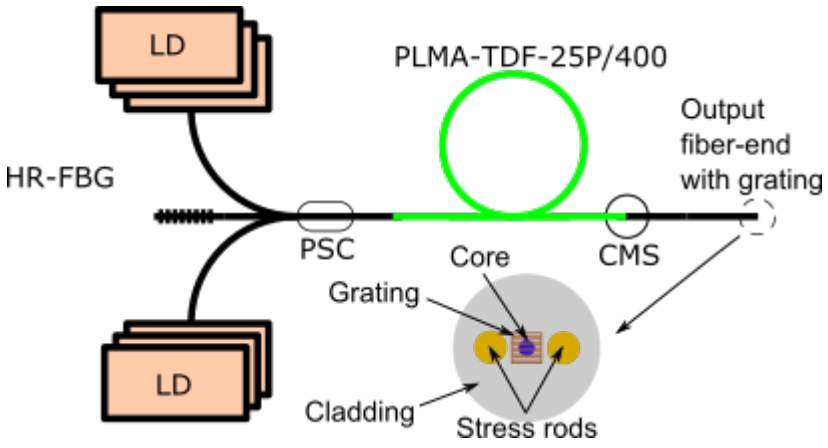

Figure 4.20: The thulium fiber laser with low reflecting polarization sensitive fiber facet grating.

optical axis we can measure the polarization of the output beam. The minimum and maximum power measured behind the polarizer are shown in Figure 4.21. The PER was about 20 dB at low powers and decreased to 10 dB for the output power of 18 W. These results are shown in Figure 4.22.

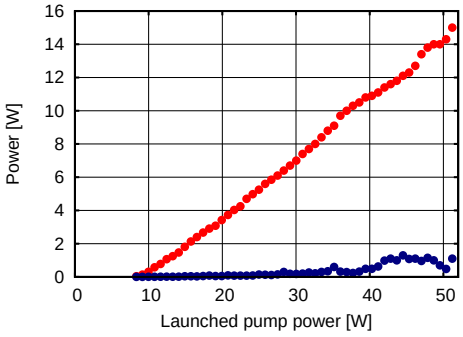

Figure 4.21: The minimum and maximum output power behind the Glan–Taylor polarizer.

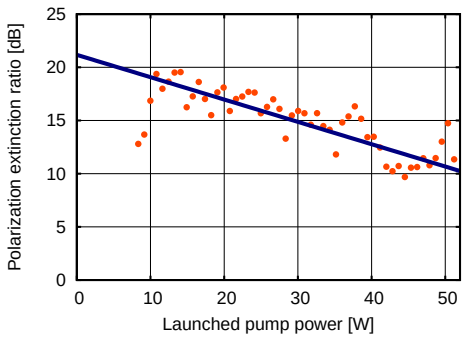

Figure 4.22: The polarization extinction ratio.

A possible explanation of the decrease in the PER is the excitation of the fast-axis mode in the laser. There can be a redistribution of the power between these two existing modes because the ratio of the reflectivity for them is only little higher than 3 dB. An improvement in the ratio can be made by using a deeper diffraction grating structure with higher polarization selectivity by using parameters of higher FOM maxima (Figure 1.11 and Equation (1.1)). The minimum and maximum output powers behind the polarizer are shown in Figure 4.21. The beam quality factor M^2 measured at maximum power was 1.4, which is the same value obtained for the perpendicularly cleaved output fiber end. The measured beam diameter as a function of the camera position is shown in Figure 4.23 for the cleaved output fiber facet and the fiber facet with grating, respectively. The output optical spectrum of the laser at maximum output power is shown in Figure 4.24.

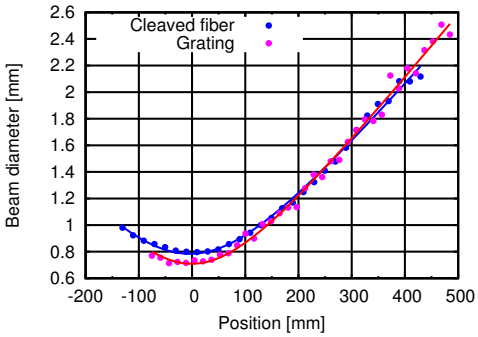

Figure 4.23: The beam diameter as a function of the camera position.

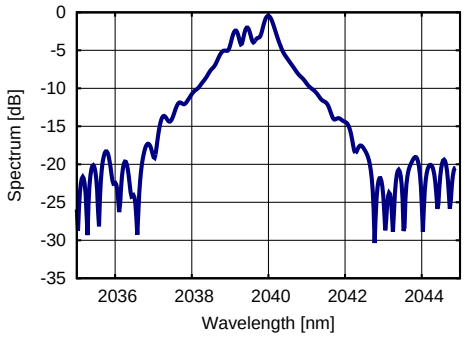

Figure 4.24: The spectrum of the laser output.

4.3 High reflecting structures

The grating HighR 25P/400 fabricated by the process described in the subsection 3.6 was tested in the same thulium fiber laser described in Section 4.2. The high reflection fiber Bragg grating was replaced by the fabricated grating and the output end was cleaved. The laser setup is shown in Figure 4.25.

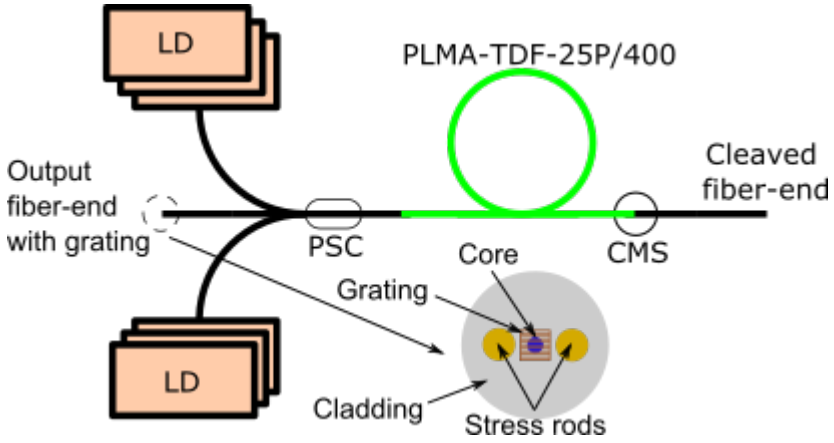

Figure 4.25: The thulium fiber laser with high reflecting polarization sensitive grating.

The output power was measured at both ends of the laser. Figure 4.26 shows the output power as a function of the current of the pump diodes. At the end of the plot the grating was destroyed. The destroyed grating is shown in Figures 4.28 and 4.29 from the top and the side, respectively. We cans see that the Ta_2O_5 layer is cracked from the center where is the fiber core and the fabricated grating. Side view of the fiber end show us that crack went in the fiber volume approximately 250 μm. Figure 4.27 shows the output power from both ends of the laser for comparison. The grating behaved like an element with a reflectance lower than the cleaved fiber facet. The reason for the destruction of the grating could be the lower damage threshold for the interconnect between the fiber facet and the high refractive index dielectric material [40]. This phenomena is investigated by research groups focused

on the high power laser systems. The Ta_2O_5 and HfO_2 materials are used to form multi-layer dielectric mirrors used in these systems [43, 44].

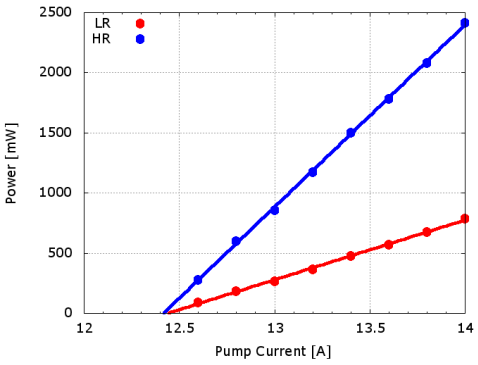

Figure 4.26: The output power of both ends of the thulium doped fiber laser with high reflectivity grating at one end and cleaved output end.

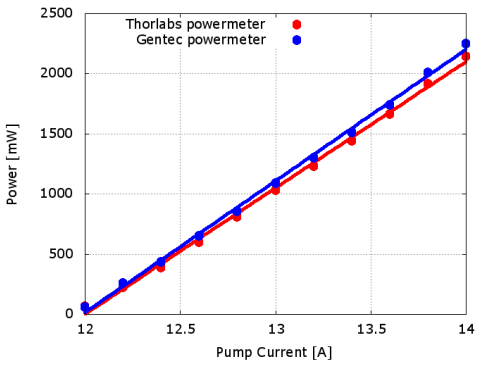

Figure 4.27: The output power of the both ends of the thulium doped fiber laser with both ends cleaved.

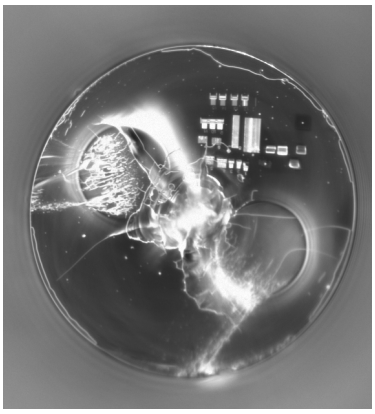

Figure 4.28: Burned high reflectivity grating, top view.

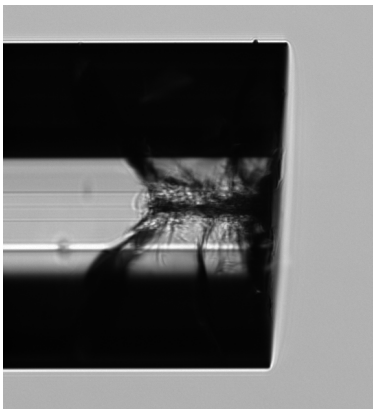

Figure 4.29: Burned high reflectivity grating, side view.

In this chapter we introduced the results from testing the fabricated structures. Anti-reflection structures were measured using a wavelength of 1550 nm to discover their reflectivity and transmission. Also, the technical steps of etching the chromium cover layer were investigated. Different etchants and etching times were tested. The low reflecting polarization sensitive grating was tested in the thulium fiber laser setup. The laser was run with cleaved fiber as output mirror to know its parameters and be able to make a comparison when we exchanged the cleaved output for the fabricated low reflecting polarization sensitive structure. The M^2, output laser power, threshold, slope efficiency and optical spectrum of the setup were measured and compared for both configurations with cleaved fiber facet end and with fabricated grating end. High reflective polarization sensitive structures were tested in a same laser setup similarly to the case of the low reflecting polarization sensitive structures except that now the Bragg grating was exchanged.

Conclusion

This section summarizes the aims of the this dissertation work and their fulfillment. It presents the results and new approaches to the area of fiber lasers.

Chapter 1 introduced the numerical modeling methods used to compute the behavior of the fiber facet gratings. The numerical simulation results for the anti-reflecting, low reflecting polarization sensitive and high reflecting polarization sensitive gratings were presented. Also, the geometry of the fiber facet grating was presented.

Chapter 2 presented and explained the prefabrication and fabrication procedures used in the process of inscribing the fiber facet gratings. The cleaving and cleaning of the fiber were explained. The preparation of the fiber holder and the process of positioning and gluing the fiber into the holder were described. The sputtering of the high refractive index layer needed for the high reflecting grating was introduced. The charging problem was resolved, three approaches to overcoming this problem having been tested.

Chapter 3 introduced the focused ion beam scanning electron microscopy employed. The final step, which is the direct inscription of the grating by the focused-ion beam, was explained there. First the optimization procedure using a silicone wafer was presented. Then we obtained the optimal procedure parameters and inscribed the gratings onto the optical fiber facet. This was done onto a cleaved fiber facet for the anti-reflection or low reflecting polarization sensitive grating, and onto a sputtered high refractive index layer for the high reflecting polarization sensitive diffraction grating. In the end, more complex 2D structures were fabricated to extend our knowledge of the fabrication process.

Chapter 4 presented the testing of the fabricated fiber facet diffraction gratings. The testing of the low reflecting polarization sensitive grating in a high power thulium doped fiber laser was presented. The grating acts as an output mirror and we achieved operation up to 18 W and a polarization extinction ratio around 20 dB for low power and around 10 dB for moderate power of 18 W. The high reflecting polarization sensitive grating was tested in the same setup but the results were the destruction of the grating. The investigation of this phenomena was out of scope of this dissertation thesis. The improvements in this area mean the research of the materials and their laser induced damage thresholds (LIDT). The other point of this investigation is LIDT of the interface between optical fiber and sputtered material.

The achievements of this dissertation work can be summarized in the points:

- Numerical modeling of the diffraction grating structure onto a cleaved fiber facet
  - Insight and understanding of behaviour of these structures

  - Optimization of the parameters of selected structures (anti-reflection grating, low reflecting polarization sensitive grating and high reflecting polarization sensitive grating)

- Development of the prefabrication procedure
  - Fiber preparation (cleaving, fiber facet cleaning and insertion of the fibers to the holder)
  - Sputtering process optimization and oxide layer characterization
- Grating fabrication process
  - Optimization of the FIB technique
  - Investigation and development of the charging mitigation
  - Fabrication of the diffraction structures onto the fiber facet (anti-reflection grating, low reflecting polarization sensitive grating, high reflecting polarization sensitive grating and 2D structures)
- Testing of fabricated structures
  - Anti-reflection structures were tested using tunable laser source (1496–1640 nm) and measurement setup developed for this purpose.
  - Low reflecting polarization sensitive grating and high reflecting polarization sensitive grating were tested in high power thulium fiber laser setup

The work presented in this thesis demonstrated numerical modeling, fabrication and testing of the 1D diffraction fiber facets structures. However there are open points to be investigated and improved. The LIDT of the thin films and interfaces between high index oxide material and substrate can be investigated. More complex structures could be simulated, fabricated and measured. By more complex structures are meant 2D or even 3D structures. Various methods and approaches could be used to affect the output of the fiber laser. Wave-front manipulation approach could be used to collimate or focus the output beam of the fiber laser which could be useful for industry applications.

Bibliography

[1] D. George, J. Lutkenhaus, D. Lowell, M. Moazzezi, M. Adewole, U. Philipose, H. Zhang, Z. L. Poole, K. P. Chen, and Y. Lin, "Holographic fabrication of 3d photonic crystals through interference of multi-beams with 4 + 1, 5 + 1 and 6 + 1 configurations," *Opt. Express* **22**(19), pp. 22421–22431, 2014.

[2] K. Kitano, K. Suzuki, K. Ishizaki, and S. Noda, "Three-dimensional photonic crystals fabricated by simultaneous multidirectional etching," *Phys. Rev. B* **91**, p. 155308, 2015.

[3] L. E. Busse, J. A. Frantz, L. B. Shaw, I. D. Aggarwal, and J. S. Sanghera, "Review of antireflective surface structures on laser optics and windows," *Appl. Opt.* **54**(31), pp. F303–F310, 2015.

[4] J. S. Choi, J. H. An, J.-K. Lee, J. Y. Lee, and S. M. Kang, "Optimization of shapes and sizes of moth-eye-inspired structures for the enhancement of their antireflective properties," *Polymers* **12**(2), 2020.

[5] A. P. Eckart, *Optical Performance of Random Antireflection Structured Surfaces on Non-Vitreous Substrates and Fused Silica Microlens Arrays*. PhD thesis, The University of North Carolina at Charlotte, 2018.

[6] A. Koshelev, G. Calafiore, C. Pina-Hernandez, F. I. Allen, S. Dhuey, S. Sassolini, E. Wong, P. Lum, S. Cabrini, and K. Munechika, "Photonics on a fiber for wavefront manipulation," in *Advanced Fabrication Technologies for Micro/Nano Optics and Photonics XI*, G. von Freymann, W. V. Schoenfeld, and R. C. Rumpf, eds., **10544**, pp. 7 – 15, International Society for Optics and Photonics, SPIE, 2018.

[7] F. Schiappelli, R. Kumar, M. Prasciolu, D. Cojoc, S. Cabrini, M. D. Vittorio, G. Visimberga, A. Gerardino, V. Degiorgio, and E. D. Fabrizio, "Efficient fiber-to-waveguide coupling by a lens on the end of the optical fiber fabricated by focused ion beam milling," *Microelectronic Engineering* **73-74**, pp. 397 – 404, 2004. Micro and Nano Engineering 2003.

[8] S. Cabrini, C. Liberale, D. Cojoc, A. Carpentiero, M. Prasciolu, S. Mora, V. Degiorgio, F. De Angelis, and E. Di Fabrizio, "Axicon lens on optical fiber forming optical tweezers, made by focused ion beam milling," *Microelectronic Engineering* **83**(4), pp. 804–807, 2006. Micro- and Nano-Engineering MNE 2005.

[9] J. Wu, M. jie Yin, K. Seefeldt, A. Dani, R. Guterman, J. Yuan, A. P. Zhang, and H.-Y. Tam, "In situ μ-printed optical fiber-tip co2 sensor using a photocrosslinkable poly(ionic liquid)," *Sensors and Actuators B: Chemical* **259**, pp. 833–839, 2018.

[10] V. G. Niziev and A. V. Nesterov, "Influence of beam polarization on laser cutting efficiency," *Journal of Physics D: Applied Physics* **32**(13), p. 1455, 1999.

[11] J. Mazumder, "Laser welding: State of the art review," *JOM* **34**, pp. 16–24, Jul 1982.

[12] V. N. N. Vaibhav Y. Javale, "A review on laser marking by nd-yag laser and fiber laser," *IJSRD - International Journal for Scientific Research & Development/* **1**(9), 2013.

[13] G. K. Samanta, S. C. Kumar, M. Mathew, C. Canalias, V. Pasiskevicius, F. Laurell, and M. Ebrahim-Zadeh, "High-power, continuous-wave, second-harmonic generation at 532 nm in periodically poled KTiOPO4," *Opt. Lett.* **33**(24), pp. 2955–2957, 2008.

[14] G. K. Samanta, S. C. Kumar, A. Aadhi, and M. Ebrahim-Zadeh, "Yb-fiber-laser-pumped, high-repetition-rate picosecond optical parametric oscillator tunable in the ultraviolet," *Opt. Express* **22**(10), pp. 11476–11487, 2014.

[15] K. Devi, S. C. Kumar, and M. Ebrahim-Zadeh, "High-power, continuous-wave, single-frequency, all-periodically-poled, near-infrared source," *Opt. Lett.* **37**(24), pp. 5049–5051, 2012.

[16] A. Liem, J. Limpert, T. Schreiber, M. Reich, H. Zellmer, A. Tünnermann, A. Carter, and K. Tankala, "High power linearly polarized fiber laser," *Conference on Lasers and Electro-Optics/International Quantum Electronics Conference and Photonic Applications Systems Technologies* , p. CMS4, Optical Society of America, 2004.

[17] K. Zhou, G. Simpson, X. Chen, L. Zhang, and I. Bennion, "High extinction ratio in-fiber polarizers based on 45° tilted fiber bragg gratings," *Opt. Lett.* **30**(11), pp. 1285–1287, 2005.

[18] J. Wang, J. Hu, L. Zhang, X. Gu, J. Chen, and Y. Feng, "A 100 W all-fiber linearly-polarized Yb-doped single-mode fiber laser at 1120 nm," *Opt. Express* **20**(27), pp. 28373–28378, 2012.

[19] U. H. Manyam, B. Samson, V. Khitrov, D. P. Machewirth, N. Jacobson, J. Farroni, D. Guertin, J. Abrmczyk, A. Carter, and K. Tankala, "Laser fibers designed for single polarization output," in *Advanced Solid-State Photonics*, *Advanced Solid-State Photonics* , p. MA6, Optical Society of America, 2004.

[20] P. Honzatko, P. Peterka, and J. Kanka, "Modulational-instability σ-resonator fiber laser," *Opt. Lett.* **26**(11), pp. 810–812, 2001.

[21] M. Vanek, J. Vanis, Y. Baravets, F. Todorov, J. Ctyroky, and P. Honzatko, "High-power fiber laser with a polarizing diffraction grating milled on the facet of an optical fiber," *Opt. Express* **24**(26), pp. 30225–30233, 2016.

[22] M. Vanek, J. Vanis, Y. Baravets, F. Todorov, J. Ctyroky, and P. Honzatko, "Anti-reflection and polarizing photonic structures for high-power fiber applications," in *Proc. SPIE 10232, Micro-structured and Specialty Optical Fibres V*, Proceedings of SPIE The International Society for Optical Engineering, 2017.

[23] H. E. Williams, D. J. Freppon, S. M. Kuebler, R. C. Rumpf, and M. A. Melino, "Fabrication of three-dimensional micro-photonic structures on the tip of optical fibers using su-8," *Opt. Express* **19**(23), pp. 22910–22922, 2011.

[24] T. Gissibl, S. Thiele, A. Herkommer, and H. Giessen, "Sub-micrometre accurate free-form optics by three-dimensional printing on single-mode fibres," *Nature Communications* **7**, pp. 11763–, 2016.

[25] T. Gissibl, M. Schmid, and H. Giessen, "Spatial beam intensity shaping using phase masks on single-mode optical fibers fabricated by femtosecond direct laser writing," *Optica* **3**(4), pp. 448–451, 2016.

[26] M. Prasciolu, D. Cojoc, S. Cabrini, L. Businaro, P. Candeloro, M. Tormen, R. Kumar, C. Liberale, V. Degiorgio, A. Gerardino, G. Gigli, D. Pisignano, E. D. Fabrizio, and R. Cingolani, "Design and fabrication of on-fiber diffractive elements for fiber-waveguide coupling by means of e-beam lithography," *Microelectronic Engineering* **67-68**, pp. 169 – 174, 2003. Proceedings of the 28th International Conference on Micro- and Nano-Engineering.

[27] E. G. Johnson, J. Stack, T. J. Suleski, C. Koehler, and W. Delaney, "Fabrication of micro optics on coreless fiber segments," *Appl. Opt.* **42**(5), pp. 785–791, 2003.

[28] X. Yang, N. Ileri, C. C. Larson, T. C. Carlson, J. A. Britten, A. S. P. Chang, C. Gu, and T. C. Bond, "Nanopillar array on a fiber facet for highly sensitive surface-enhanced raman scattering," *Opt. Express* **20**(22), pp. 24819–24826, 2012.

[29] G. Kostovski, D. White, A. Mitchell, M. Austin, and P. Stoddart, "Nanoimprinted optical fibres: Biotemplated nanostructures for {SERS} sensing," *Biosensors and Bioelectronics* **24**(5), pp. 1531 – 1535, 2009. Selected Papers from the Tenth World Congress on Biosensors Shangai, China, May 14-16, 2008.

[30] G. Kostovski, U. Chinnasamy, S. Jayawardhana, P. R. Stoddart, and A. Mitchell, "Sub-15nm optical fiber nanoimprint lithography: A parallel, self-aligned and portable approach," *Advanced Materials* **23**(4), pp. 531–535, 2011.

[31] M. L. David Pallares-Aldeiturriaga, Luis Rodriguez-Cobo and J. M. Lopez-Higuera, "Diffractive elements inscribed at end-fiber surface by femtosecond laser," *Journal of Lightwave Technology* **37**(18), 2019.

[32] P. Kwiecien, I. Richter, and J. Ctyroky, "Rcwa/arcwa - an efficient and diligent workhorse for nanophotonic/nanoplasmonic simulations - can it work even better?," pp. 1–8, 2015.

[33] A. F. Oskooi, D. Roundy, M. Ibanescu, P. Bermel, J. D. Joannopoulos, and S. G. Johnson, "MEEP: A flexible free-software package for electromagnetic simulations by the FDTD method," *Computer Physics Communications* **181**, pp. 687–702, 2010.

[34] J. Čtyroký, "3-d bidirectional propagation algorithm based on fourier series," *J. Lightwave Technol.* **30**(23), pp. 3699–3708, 2012.

[35] Corning, *Corning SMF-28 Ultra Optical Fiber*.

[36] Nufern, *FUD-3716, Revision: CPLMA-GDF-25/400-10FA OpticalFiber*.

[37] K. Yee, "Numerical solution of initial boundary value problems involving maxwell's equations in isotropic media," *IEEE Transactions on Antennas and Propagation* **14**(3), pp. 302–307, 1966.

[38] P. Lalanne and J.-P. Hugonin, "High-order effective-medium theory of subwavelength gratings in classical mounting: application to volume holograms," *J. Opt. Soc. Am. A* **15**(7), pp. 1843–1851, 1998.

[39] T. Czyszanowski, "Monolithic high contrast grating vcsel," in *SMMO2015 Conference & COST MP1204 Conference, Prague*, 2015.

[40] L. Gallais and M. Commandre, "Laser-induced damage thresholds of bulk and coating optical materials at 1030 nm, 500 fs," *Appl. Opt.* **53**(4), pp. A186–A196, 2014.

[41] S. Shimizu, T. Saitoh, M. Uzawa, M. Yuasa, K. Yano, T. Maruyama, and K. Watanabe, "Synthesis and applications of sulfonated polyaniline," *Synthetic Metals* **85**(1), pp. 1337–1338, 1997.

[42] P. Honzatko, Y. Baravets, F. Todorov, P. Peterka, and M. Becker, "Coherently combined power of 20 w at 2000 nm from a pair of thulium-doped fiber lasers," *Laser Physics Letters* **10**(9), p. 095104, 2013.

[43] Y. Zhang, Y. Wang, H. He, R. Chen, Z. Wang, D. Li, M. Zhu, Y. Zhao, Y. Jin, K. Yi, Y. Shao, Y. Leng, R. Li, and J. Shao, "Effect of electric field regulation on laser damage of composite low-dispersion mirrors," *Coatings* **11**(1), 2021.

[44] D. Schiltz, D. Patel, C. Baumgarten, B. A. Reagan, J. J. Rocca, and C. S. Menoni, "Strategies to increase laser damage performance of ta2o5/sio2 mirrors by modifications of the top layer design," *Appl. Opt.* **56**(4), pp. C136–C139, 2017.

List of publications

Articles

[1] M. Vanek, J. Vanis, Y. Baravets, F. Todorov, J. Ctyroky, and P. Honzatko, "High-power fiber laser with a polarizing diffraction grating milled on the facet of an optical fiber," *Opt. Express* **24**, pp. 30225-30233, Dec 2016.

[2] M. Vanek M., et. al., "Leaky-mode resonant gratings on fibre facet," *Optical and Quantum Electronics* **50**, pp. 50, 2018.

Conferences

[1] M. Vanek, P. Honzatko, F. Todorov, and J. Vanis, "Focused Ion Beam Micromachining of Fiber Facet Photonic Structures", *20th Slovak - Czech - Polish Optical Conference On Wave and Quantum Aspects of Contemporary Optics*, Jasna, Slovakia, 2016.

[2] M. Vanek, J. Vanis, Y. Baravets, F. Todorov, J. Ctyroky, and P. Honzatko, "Anti-reflection and polarizing photonic structures for high power fiber applications," in *Proc. SPIE 10232, Micro-structured and Specialty Optical Fibres V*, Proceedings of SPIE The International Society for Optical Engineering, May 2017.

[3] M. Vanek, J. Ctyroky, and P. Honzatko, "Leaky-mode resonant gratings on a fiber facet", *Optical Wave and Waveguide Theory and Numerical Modelling workshop*, Proceedings of the 25th International Workshop on Optical Wave & Waveguide Theory and Numerical Modelling, ISBN: 978-90-386-4318-2.

[4] M. Vanek, J. Vanis, Y. Baravets, F. Todorov, J. Ctyroky, and P. Honzatko, "Fiber facet gratings for use in high-power fiber lasers," *Proceedings WSOF2017*, 2017

[5] M. Vanek, and P. Honzatko, "Polarizing Fibre Facet Grating with High Modal Reflectance," *The 21st Czech-Polish-Slovak Optical Conference On Wave and Quantum Aspects of Contemporary Optics*, 2018, Lednice, Czech Republic, 2018.

[6] M. Vanek, J. Vanis, Y. Baravets, F. Todorov, J. Ctyroky, and P. Honzatko, "Fiber facet gratings for high power fiber lasers," *Proc. SPIE 10603, Photonics, Devices, and Systems VII*, Dec 2017, https://doi.org/10.1117/12.2293605.

Others

[1] M. Vanek, J. Tomko and P. Honzatko, "Design, fabrication and testing of polarization insensitive diffraction grating for high power fiber laser application at 2 μm wavelength," *Siegman International School on Lasers*, Amberg, Germany, 2015.

[2] M. Vanek, Y. Baravets, P. Honzatko, and P. Gladkov, "Narrow band CW MIR generator based on the difference frequency generation in KTP crystal," *Summer school of silicon photonics*, Gent, Belgium, 2014.

Appendix - Journal publications

Research Article | Vol. 24, No. 26 | 26 Dec 2016 | OPTICS EXPRESS 30225

Optics EXPRESS

High-power fiber laser with a polarizing diffraction grating milled on the facet of an optical fiber

MARTIN VANEK, JAN VANIS, YAUHEN BARAVETS, FILIP TODOROV, JIRI CTYROKY, AND PAVEL HONZATKO*

Institute of Photonics and Electronics, CAS, Chaberska 57, 182 51 Prague, Czech Republic
**honzatko@ufe.cz*

Abstract: We milled a sub-wavelength diffraction grating on the facet of a large mode area fiber. The diffraction grating had different reflectivities for TE and TM polarized light. It was tested in a thulium-doped fiber laser where it functioned as a low reflectivity output mirror integrated with an intracavity polarizer. Compared to the laser with a perpendicularly cleaved output fiber, the laser with a diffraction grating had a slightly increased threshold power and the same slope efficiency. The beam quality factor M^2 was not impaired. Polarization extinction ratios of about 20 dB that were observed at low laser powers dropped to 10 dB at high powers.

OCIS codes: (140.3510) Lasers, fiber; (060.2420) Fibers, polarization-maintaining; (050.1950) Diffraction gratings.

References and links

1. K. Devi, S. C. Kumar, and M. Ebrahim-Zadeh, "High-power, continuous-wave, single-frequency, all-periodically-poled, near-infrared source," Opt. Lett. **37**, 5049–5051 (2012).
2. G. K. Samanta, S. C. Kumar, A. Aadhi, and M. Ebrahim-Zadeh, "Yb-fiber-laser-pumped, high-repetition-rate picosecond optical parametric oscillator tunable in the ultraviolet," Opt. Express **22**, 11476–11487 (2014).
3. G. K. Samanta, S. C. Kumar, M. Mathew, C. Canalias, V. Pasiskevicius, F. Laurell, and M. Ebrahim-Zadeh, "High-power, continuous-wave, second-harmonic generation at 532 nm in periodically poled KTiOPO4," Opt. Lett. **33**, 2955–2957 (2008).
4. V. G. Niziev and A. V. Nesterov, "Influence of beam polarization on laser cutting efficiency," Journal of Physics D: Applied Physics **32**, 1455 (1999).
5. R. L. Harzic, D. Dörr, D. Sauer, M. Neumeier, M. Epple, H. Zimmermann, and F. Stracke, "Large-area, uniform, high-spatial-frequency ripples generated on silicon using a nanojoule-femtosecond laser at high repetition rate," Opt. Lett. **36**, 229–231 (2011).
6. T. Y. Fan, "Laser beam combining for high-power, high-radiance sources," IEEE Journal of Selected Topics in Quantum Electronics **11**, 567–577 (2005).
7. P. Honzatko, P. Peterka, and J. Kanka, "Modulational-instability σ-resonator fiber laser," Opt. Lett. **26**, 810–812 (2001).
8. A. Liem, J. Limpert, T. Schreiber, M. Reich, H. Zellmer, A. Tünnermann, A. Carter, and K. Tankala, "High power linearly polarized fiber laser," in "Conference on Lasers and Electro-Optics/International Quantum Electronics Conference and Photonic Applications Systems Technologies," (Optical Society of America, 2004), p. CMS4.
9. J. Wang, J. Hu, L. Zhang, X. Gu, J. Chen, and Y. Feng, "A 100 W all-fiber linearly-polarized Yb-doped single-mode fiber laser at 1120 nm," Opt. Express **20**, 28373–28378 (2012).
10. U. H. Manyam, B. Samson, V. Khitrov, D. P. Machewirth, N. Jacobson, J. Farroni, D. Guertin, J. Abrmczyk, A. Carter, and K. Tankala, "Laser fibers designed for single polarization output," in "Advanced Solid-State Photonics," (Optical Society of America, 2004), p. MA6.
11. X. Yang, N. Ileri, C. C. Larson, T. C. Carlson, J. A. Britten, A. S. P. Chang, C. Gu, and T. C. Bond, "Nanopillar array on a fiber facet for highly sensitive surface-enhanced raman scattering," Opt. Express **20**, 24819–24826 (2012).
12. E. G. Johnson, J. Stack, T. J. Suleski, C. Koehler, and W. Delaney, "Fabrication of micro optics on coreless fiber segments," Appl. Opt. **42**, 785–791 (2003).
13. M. Prasciolu, D. Cojoc, S. Cabrini, L. Businaro, P. Candeloro, M. Tormen, R. Kumar, C. Liberale, V. Degiorgio, A. Gerardino, G. Gigli, D. Pisignano, E. D. Fabrizio, and R. Cingolani, "Design and fabrication of on-fiber diffractive elements for fiber-waveguide coupling by means of e-beam lithography," Microelectronic Engineering **67–68**, 169–174 (2003). Proceedings of the 28th International Conference on Micro- and Nano-Engineering.
14. F. Schiappelli, R. Kumar, M. Prasciolu, D. Cojoc, S. Cabrini, M. D. Vittorio, G. Visimberga, A. Gerardino, V. Degiorgio, and E. D. Fabrizio, "Efficient fiber-to-waveguide coupling by a lens on the end of the optical fiber fabricated by focused ion beam milling," Microelectronic Engineering **73–74**, 397–404 (2004). Micro and Nano Engineering 2003.

#279686 http://dx.doi.org/10.1364/OE.24.030225
Journal © 2016 Received 28 Oct 2016; revised 7 Dec 2016; accepted 12 Dec 2016; published 21 Dec 2016

Optics EXPRESS

15. G. Kostovski, D. White, A. Mitchell, M. Austin, and P. Stoddart, "Nanoimprinted optical fibres: Biotemplated nanostructures for SERS sensing," Biosensors and Bioelectronics **24**, 1531–1535 (2009). Selected Papers from the Tenth World Congress on Biosensors Shangai, China, May 14-16, 2008.
16. G. Kostovski, U. Chinnasamy, S. Jayawardhana, P. R. Stoddart, and A. Mitchell, "Sub-15nm optical fiber nanoimprint lithography: A parallel, self-aligned and portable approach," Advanced Materials **23**, 531–535 (2011).
17. H. E. Williams, D. J. Freppon, S. M. Kuebler, R. C. Rumpf, and M. A. Melino, "Fabrication of three-dimensional micro-photonic structures on the tip of optical fibers using SU-8," Opt. Express **19**, 22910–22922 (2011).
18. T. Gissibl, S. Thiele, A. Herkommer, and H. Giessen, "Sub-micrometre accurate free-form optics by three-dimensional printing on single-mode fibres," Nature Communications **7**, 11763 (2016).
19. T. Gissibl, M. Schmid, and H. Giessen, "Spatial beam intensity shaping using phase masks on single-mode optical fibers fabricated by femtosecond direct laser writing," Optica **3**, 448–451 (2016).
20. A. F. Oskooi, D. Roundy, M. Ibanescu, P. Bermel, J. D. Joannopoulos, and S. G. Johnson, "MEEP: A flexible free-software package for electromagnetic simulations by the FDTD method," Computer Physics Communications **181**, 687–702 (2010).
21. J. Čtyroký, "3-D bidirectional propagation algorithm based on fourier series," J. Lightwave Technol. **30**, 3699–3708 (2012).
22. P. Lalanne and J.-P. Hugonin, "High-order effective-medium theory of subwavelength gratings in classical mounting: application to volume holograms," J. Opt. Soc. Am. A **15**, 1843–1851 (1998).
23. P. Honzatko, Y. Baravets, F. Todorov, P. Peterka, and M. Becker, "Coherently combined power of 20 W at 2000 nm from a pair of thulium-doped fiber lasers," Laser Physics Letters **10**, 095104 (2013).
24. M. Michalska, W. Brojek, Z. Rybak, P. Sznelewski, M. Mamajek, and J. Swiderski, "Highly stable, efficient Tm-doped fiber laser – a potential scalpel for low invasive surgery," Laser Physics Letters **13**, 115101 (2016).

1. Introduction

High-power polarized laser beams are needed in nonlinear optics to pump optical parametric oscillators [1, 2], generators of second harmonics [3], etc. In materials processing, the polarization dependence of laser cutting efficiency was discussed by Niziev and Nesterov [4]. Polarization-dependent, laser-induced periodic surface structures are formed on the laser-treated surfaces as a result of interference between the incident laser beam and surface scattered waves [5]. Polarization multiplexing is used to scale the power of fiber lasers [6].

Several approaches are used to achieve a stable and defined polarization state at the output of fiber lasers. Polarizing isolators, polarizers, and other hybrid elements are included into low-power fiber lasers made from polarization-maintaining (PM) fibers. The σ-laser configuration is used to mix PM and non-PM elements in resonators with defined output polarization [7].

Any passive intracavity element negatively influences the threshold, slope efficiency, reliability and cost of high-power fiber lasers. Active PM fibers were combined with a bulk polarization beam splitter in the resonator of a 300-watt ytterbium-doped fiber laser [8]. Cross-axis wavelength-matched fiber Bragg gratings were used to define the wavelength and linear polarization in a 100-watt ytterbium-doped fiber laser [9]. A linearly polarized output was achieved by inducing differential bending loss between the light polarized along the slow axis and fast axis of the PM fiber. Due to a lower effective index of refraction, light polarized along the fast axis of the fiber has higher bending loss when the fiber is wound into a coil of appropriate diameter. The technique was demonstrated for a 100-watt ytterbium-doped fiber laser [10].

One of the emerging technologies in fiber optics is the fabrication of microoptical elements directly on cleaved or polished end fiber facets through etching, milling or additive manufacturing. To date, interference lithography [11], photolithography [12], electron-beam lithography [13], focused ion-beam milling [14], nano-imprint technology [15, 16], two-photon polymerization 3D printing [17–19], and laser micromachining were demonstrated as tools for fiber-facet patterning. The polymers are not yet suited for high-power applications and their exploitations is tricky due to polymerization inhomogeneities and nonuniform deformations occurring during the exposition and development processes [18]. The best suited technique of micro-patterning for high-power applications is etching or milling the microstructures directly on silica fiber facets.

In this paper, we present a polarizing diffraction grating etched directly on the fiber facet

Optics EXPRESS

serving as a laser output reflector. We assume that light propagates in the fiber core towards the perpendicularly cleaved fiber end, which serves as a low-reflectivity mirror. The diffraction grating milled on the surface of the fiber facet modifies the reflection coefficient of the mirror. A focused ion beam was used to mill the grating grooves perpendicularly to the slow axis of the PM fiber. The grating parameters were optimized in a way ensuring that difference in reflections between the TE and TM modes was achieved, the reflection of the TE mode was close to optimum, and loss caused by diffraction into higher modes was low. The grating was tested in a thulium-doped fiber laser with a wavelength of 2040 nm at moderate powers.

Design and fabrication of diffraction gratings are described in Section 2 and 3, respectively. The grating performance in the laser at moderate powers is given in Section 4.

2. Diffraction grating design

The diffraction gratings properties were analyzed and optimized by means of a rigorous coupled-wave analysis (RCWA), finite-difference time-domain (FDTD) method, and Fourier modal method (FMM). The RSoft DiffractMOD, MIT MEEP [20], and UFE FMM [21] simulation software were used for RCWA, FDTD, and FMM analysis, respectively. The RCWA method allows fast optimization of grating parameters. The FDTD and FMM methods were used to evaluate the reflectivity of optimized gratings for guided mode, and the FDTD method additionally provided estimation of the modal loss.

Light diffraction is limited to zero order in sub-wavelength diffraction gratings. Optical properties of such gratings can be explained by the effective-medium theory [22]. The sub-wavelength grating behaves roughly as a homogeneous birefringent layer. Its reflectivity varies periodically with grating thickness with period depending on the polarization of incident light. The maximum reflectivity can not exceed a value given by Fresnel's equations for an unstructured fiber facet in the effective-medium model.

Gratings with longer periods allow achieving zeroth order diffraction efficiencies beyond the Fresnel reflection limit at the expense of introducing loss due to the diffraction into higher reflected orders. In this work we optimized the grating with the aims as follows: a) achieving the reflectivity of the fundamental fiber mode close to the Fresnel reflection for unstructured fiber facet and avoiding diffraction into higher reflected modes in order to keep the laser threshold sufficiently low and slope efficiency high, b) designing the grating as shallow as possible to facilitate its fabrication, c) maximizing the difference between the grating reflectivity for TE and TM polarizations. The oscillation direction of electric field vector is parallel to the direction of grating grooves for TE polarization, and perpendicular for TM polarization. Our gratings were designed for a wavelength of 2040 nm. The product $(R_0^{\mathrm{TE}} - R_0^{\mathrm{TM}})R_0^{\mathrm{TE}}$, where R_0^{TE} and R_0^{TM} are zeroth order reflectivities for TE and TM polarized light, respectively, was adopted as a figure-of-merit (FOM).

The results of the RCWA optimization are shown in Fig. 1. The zeroth order reflectivity for TE-mode has oscillatory character as expected from the effective-medium model. The reflectivity is given by Fresnel's equations for zero depth of the diffraction grating. The reflectivity decreases with increasing grating depth until the quarter depth is achieved. Almost complete suppression of the reflection is possible for appropriately chosen fill factor, which is approximately 0.3 for silica/air interface. Then the reflectivity grows again until the first maximum is achieved and the whole process repeats. The FOM closely follows oscillations of the zeroth order reflectivity with amplitude growing as a result of increasing difference in the zeroth order reflectivity of TE and TM modes. The FOM achieves its first maximum for a grating depth of 590 nm and fill factor of 0.6, and the second maximum at a grating depth of 1415 nm and fill factor of 0.55. The results of optimization are summarized in Table 1. The RCWA results were obtained for plane wave diffraction and were verified by 2D FDTD method for the diffraction of the guided mode of a slab waveguide with a thickness and numerical aperture matched to the

Optics EXPRESS

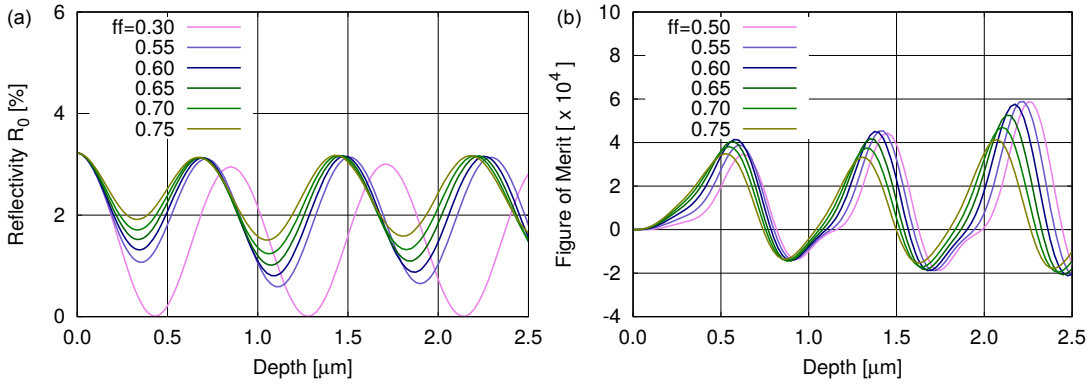

Fig. 1. (a) Zeroth order reflectivity of the grating R_0^{TE} as a function of the grating depth and grating fill factor, and (b) figure-of-merit defined as the product $(R_0^{\mathrm{TE}} - R_0^{\mathrm{TM}})R_0^{\mathrm{TE}}$.

Table 1. **Parameters of optimized diffraction grating**

Grating parameters			RCWA results		MEEP results	
Period [nm]	Fill factor	Grating depth [nm]	FOM	R_0^{TE} [%]	FOM	R_0^{TE} [%]
1400	0.6	590	3.8×10^{-4}	2.71	5.2×10^{-4}	3.06

fiber (Fig. 2). To complete the optimization, a 3D analysis of fundamental fiber mode reflection was performed by using FMM. Similar results are obtained by the FDTD and FMM methods, while the RCWA method allows interpretation of loss as a diffraction of light into ±1 orders. The ±1 reflected diffraction orders have angles that are far away beyond the total internal reflection angle of the weakly guiding core of single mode fiber and are source of loss. The FDTD simulations reveal a smoother onset of modal loss resulting from the onset of higher order diffraction in reflected light, as can be seen in Fig. 2b. The dashed curves in Fig 2b are obtained as a sum of diffraction efficiencies into the ±1 orders in reflection calculated by RCWA. Smoother onset results from low spectral resolution of the grating caused by low number of grooves irradiated by fiber mode. Further evidence of the source of loss is shown in Fig. 3, where ±1 orders are clearly visible in the diffraction pattern calculated by FDTD method.

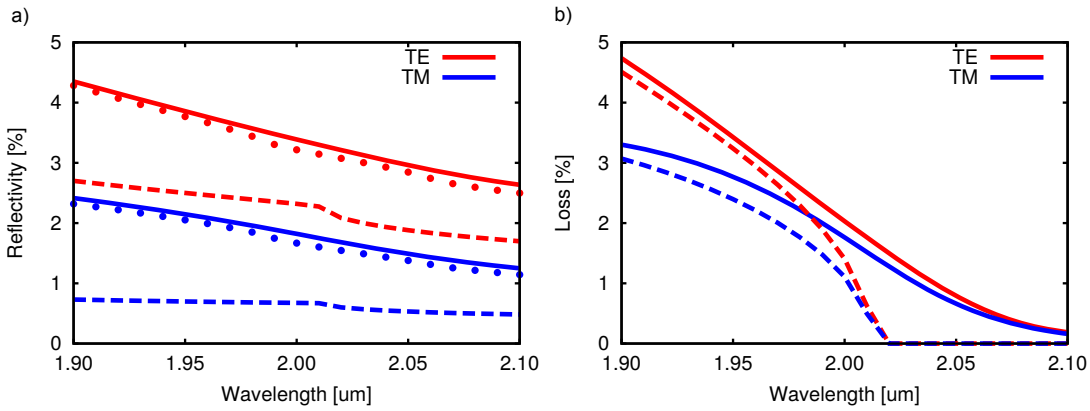

Fig. 2. (a) Zero-order diffraction efficiency in reflection of TE and TM polarized light from diffraction grating numerically predicted by RCWA (dashed), FMM (dotted), and FDTD (solid) methods. (b) Loss by diffraction into higher orders predicted by RCWA technique (dashed) and modal loss predicted by FDTD method (solid).

Optics EXPRESS

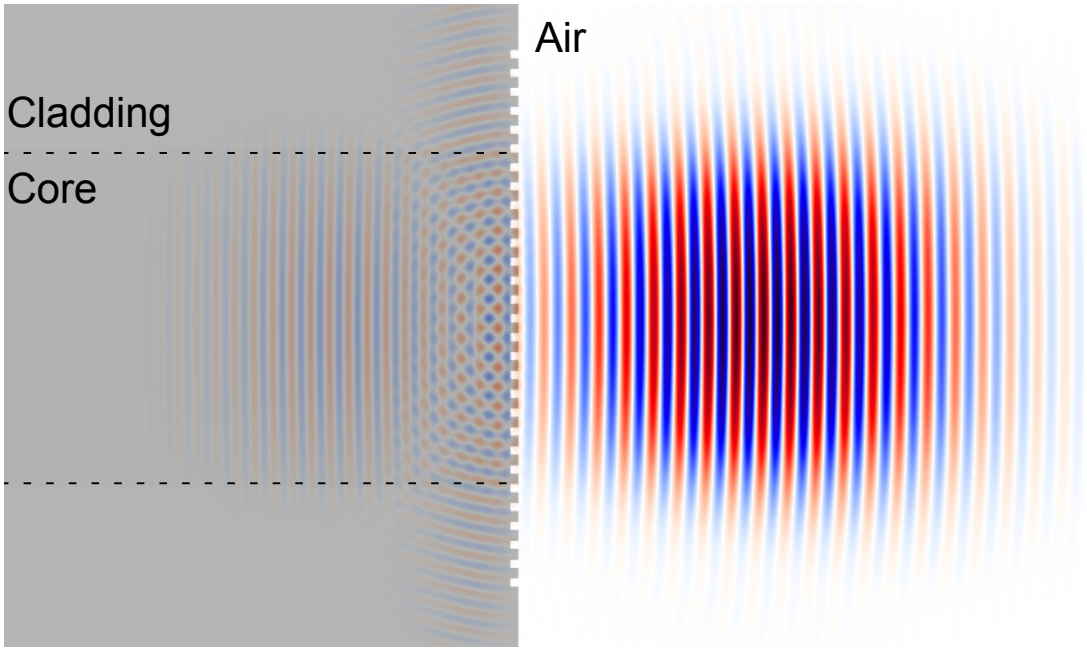

Fig. 3. E_z component (parallel to grating grooves) of the field calculated by the FDTD method short after the reflection of the pulse propagating in the slab waveguide from the grating. The slab waveguide represents the fiber core in 2D simulations. The light pulse was emited from the fiber to right while the reflected pulse propagates in the fiber core to left and part of the incident pulse energy is lost in the cladding through diffraction into ±1 orders in reflection.

3. Fabrication of the diffraction grating

The designed grating was fabricated using the focused ion beam (FIB) milling. This single-step and maskless process is a very convenient technique for rapid prototyping. The milling was carried out using our FIB machine (Tescan LYRA3) with an ion source of liquid gallium, integrated with a scanning electron microscope (SEM), gas injection system (GIS), and secondary ion mass spectroscope (SIMS). The ion beam spot size of our FIB device for fine milling is about 70 nm. The limitations of our device are in the transversal dimensions of the structure 400 μm × 400 μm, the aspect ratio of the holes or trenches because the beam should be focused onto the bottom of the structure, and accumulation of the electric charge on the surface of the dielectric, which repels ions. In situ calibration was performed sufficiently far from the fiber core before inscribing the grating. A small-size test grating was milled close to the perimeter of the fiber, platinum strip was deposited across the grating grooves using GIS, and finally, a trench was etched to measure grating's depth and fill factor. Based on the calibration data, a grating with dimensions of approximately 35 μm × 35 μm was fabricated centered at the fiber axis with grooves oriented along the fast axis of the PM fiber. The fiber facet with the diffraction and test gratings is shown in Fig. 4. The fabricated grating has a groove depth of approximately 550 nm and a fill factor of 0.7 which differs slightly from designed parameters. The difference from optimum parameters should have small effect on results as can be seen from Fig. 1.

4. Test of the diffraction grating as a polarizer and output mirror in a fiber laser

The diffraction grating was tested in a thulium-doped fiber laser. The fiber laser only involves PM fibers and PM pigtailed optical components. The laser scheme is shown in Fig. 5. The resonator consists of an active fiber (PLMA-TDF), pump-signal combiner (PSC), and high-

Optics EXPRESS

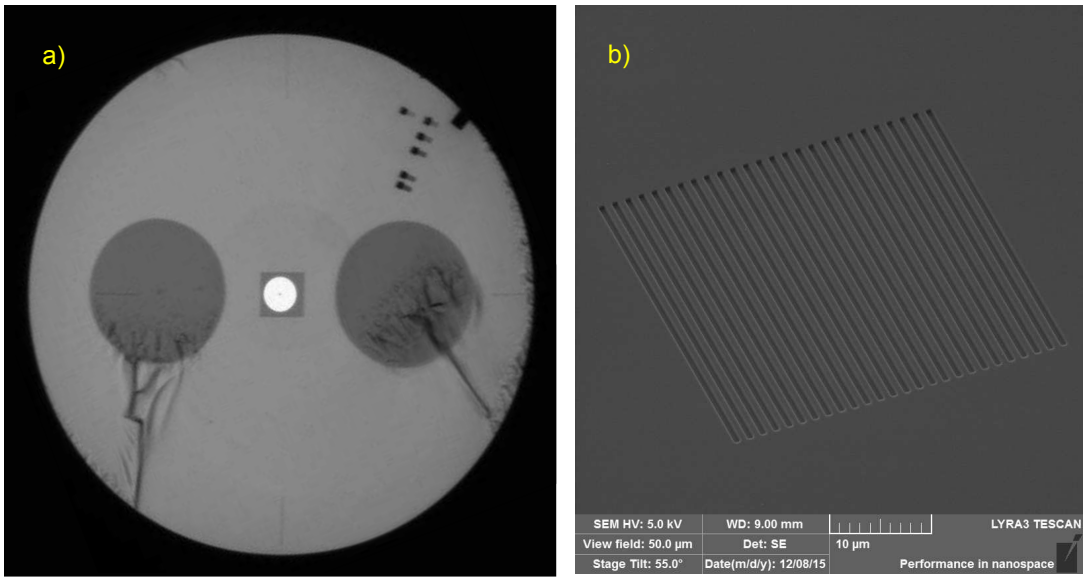

Fig. 4. (a) Diffraction grating fabricated on the fiber facet. It is seen as a rectangle on backlit fiber core. The grating grooves are vertical. Stress elements of the PM fiber are seen as dark circles in the cladding. Test gratings are situated in the upper right part of the figure. (b) SEM image of the milled diffraction grating.

reflectivity fiber Bragg grating (HR-FBG). We used 35-watt 793-nanometer laser diodes from LIMO coupled to 220/280 µm multimode pigtails with a numerical aperture of 0.22 as pump sources. A double-clad thulium-doped PM fiber (PLMA-TDF-25P/400-HE from Nufern) with a large mode area and length of five meters was used as an active fiber. The fiber has a core diameter of 25 µm and an inner cladding diameter of 400 µm. It is coated with a low-index polymer with an outer diameter of 550 µm. The numerical apertures of the core and of the inner cladding are 0.09 and 0.46, respectively. The multimode pump absorption is 12 dB for a five-meters long fiber. The unabsorbed pump power is trapped in a cladding mode stripper (CMS). A laser resonator is created between the HR-FBG spliced to PSC and a low reflectivity mirror in the form of a perpendicularly cleaved output fiber. The HR-FBG has a reflectivity of 99.6% at a wavelength of 2039 nm and reflection bandwidth of 1 nm. The output mirror has a reflectivity of 3.5% given by Fresnel's equations. The output laser power was measured with a power meter from Gentec. The polarization extinction ratio of the laser was determined using a Glan-Taylor polarizer and the beam quality factor was assessed by pyroelectric camera (Pyrocam III) combined with a linear kinematic stage. The optical spectrum was recorded by a Fourier transform infrared spectrometer (Nicolet 8700). The dependence of the laser output power on the launched pump power is shown in Fig. 6. The power launched into the active fiber was measured at the output of the pump-signal combiner as a function of pump laser diode currents during the construction of the laser before splicing with the active fiber. The laser has a maximum output power of 18 W, threshold of 7.4 W, and slope efficiency of 42%. The slope efficiency is lower than the slope efficiency of lasers pumped directly through the HR-FBG [23, 24], which we attribute to additional insertion loss of pump-signal combiner. We determined the M^2 beam quality factor to be about 1.4, which indicates that higher-order modes are present in the large mode area fiber. The polarization extinction ratio of the laser beam was close to 1, which reflects the fact that no elements with significant polarization-dependent loss were included in the resonator.

Once the fiber laser with a perpendicularly cleaved output fiber was characterized, we spliced

Optics EXPRESS

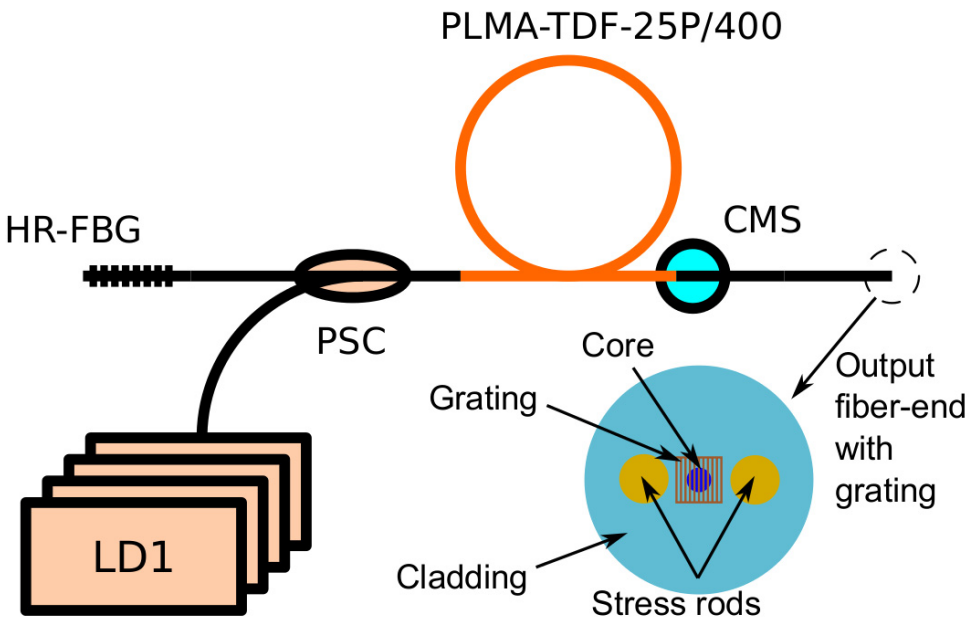

Fig. 5. Thulium-doped fiber laser.

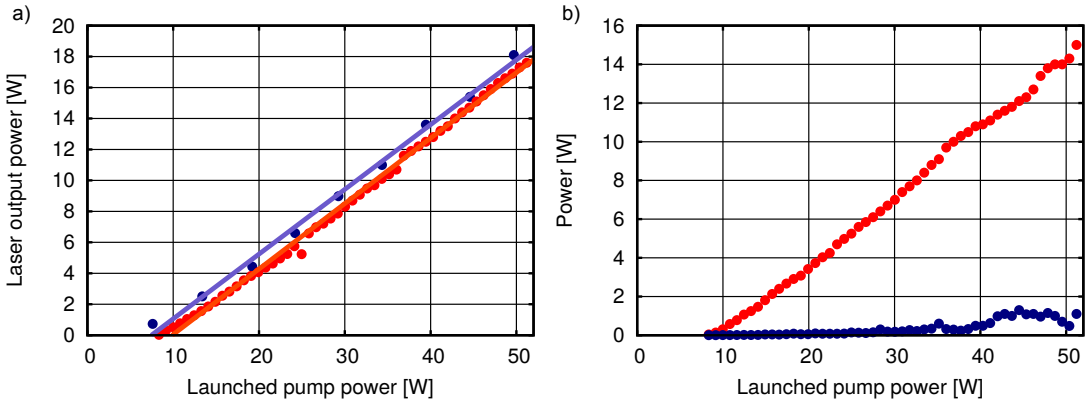

Fig. 6. (a) Dependence of the laser output power on the launched pump power for the perpendicularly cleaved fiber (blue) and fiber with difraction grating (red). (b) The maximum (red) and minimum (blue) power behind the external polarizer.

Optics EXPRESS

the laser output fiber with the piece of the fiber where the diffraction grating was fabricated. We observed that the threshold slightly increased from 7.4 W to 9.9 W while the slope efficiency remained at 42% (Fig. 6a). This is in agreement with results of simulations where low diffraction loss is imposed by the grating, while the transmission coefficient of the grating is close to that of perpendicularly cleaved fiber. The measured polarization extinction ratio defined as $PER = 10\log(P_{max}/P_{min})$ was about 20 dB at low powers and decreased to 10 dB for the output power of 18 W (Fig. 7). The most probable reason of the PER degradation is excitation of the fast-axis mode in the laser and redistribution of the power between two existing modes because the reflectivity ratio between the TE and TM polarization of the grating is only slightly higher than 3dB. Higher extinction ratio could be expected for deeper output gratings with larger polarization selectivity operating in third or even higher FOM maximum (Fig. 1).

The minimum and maximum powers measured behind the polarizer are shown in Fig. 6b. The measured beam quality factor M^2 measured at maximum power was 1.4, which is the same value obtained for the perpendicularly cleaved output fiber end. The measured beam diameter as a function of the camera position is shown in Fig. 8a) for both cases. The optical spectrum of the laser at maximum power is shown in Fig. 8b).

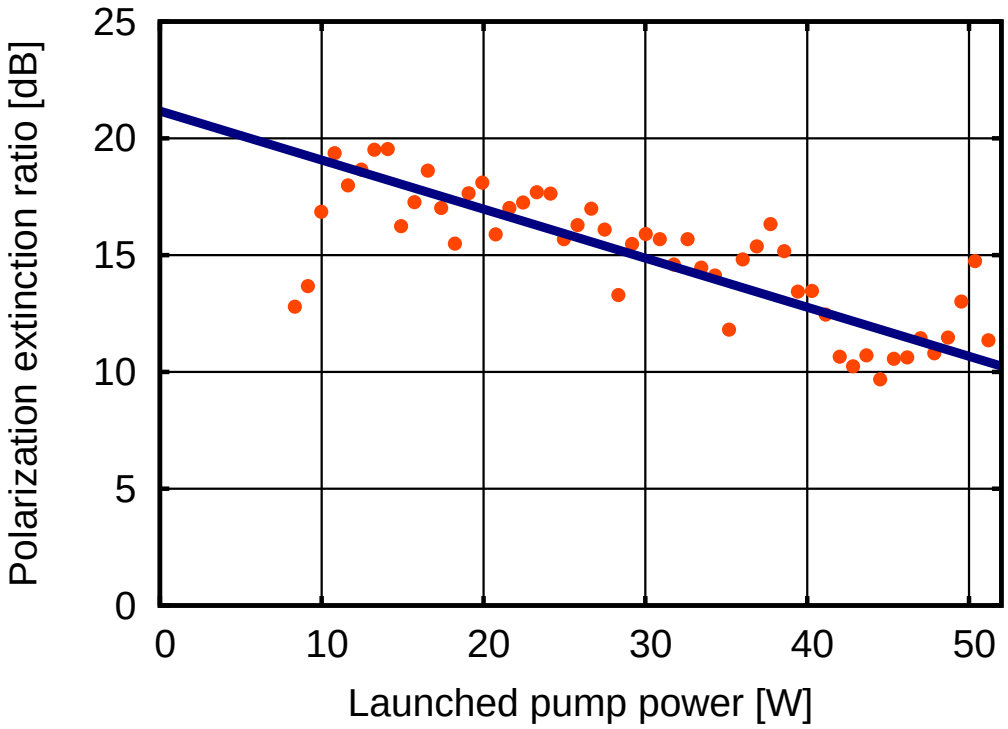

Fig. 7. Dependence of the laser output polarization extinction ratio on the launched pump power.

5. Conclusion

Transmission properties of optical fibers can be modified by nanostructuring of the fiber end. In this paper, we modified the fiber facet reflection properties by milling a sub-wavelength diffraction grating on the facet of a perpendicularly cleaved fiber. The diffraction grating has different reflectivities for TE and TM polarized light and can act as a polarizer in a fiber laser. We tested the grating as an output low-reflection mirror in the moderate-power, thulium-doped

Optics EXPRESS

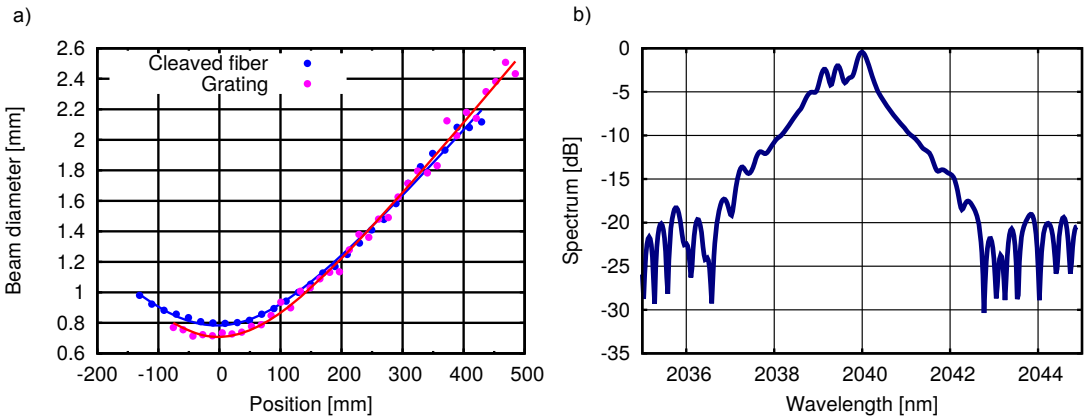

Fig. 8. (a) Dependence of the beam diameter on the camera position for the laser with a perpendicularly cleaved output fiber (blue) and with difraction grating (red). (b) The optical spectrum of the laser with diffraction grating.

fiber laser. The beam quality parameter M^2 and slope efficiency were preserved while the laser threshold slightly increased. The output beam was polarized with a polarization extinction ratio of about 20 dB at low powers and 10 dB at high powers. No grating damage was observed up to 18 W of output power limited by experiment setup.

Funding

Czech Science Foundation, grant GAP15-07908S.

Opt Quant Electron (2018) 50:50
https://doi.org/10.1007/s11082-017-1293-z

Leaky-mode resonant gratings on a fibre facet

Martin Vanek[1] · Jiri Ctyroky[1] · Pavel Honzatko[1]

Received: 24 June 2017 / Accepted: 19 December 2017 / Published online: 13 January 2018

Abstract Numerical investigation shows that an optimised leaky-mode resonant diffraction gratings fabricated in Ta_2O_5 layer deposited on the facet of an optical fibre can have a modal reflectance peak of more than 95%, 3 dB spectral bandwidth of about 50 nm and polarization extinction ratio of almost 18 dB. The grating is intended to be employed as a high-reflectance, wavelength- and polarization-dependent mirror in a fibre laser. We compare results of 2D and 3D modelling, investigate influence of grating parameters on spectral shape of modal reflectance and discuss fabrication tolerances.

Keywords Leaky-mode resonant gratings · Large mode area fibres · Finite-difference time-domain method

The authors acknowledge funding of this work by the Czech Science Foundation, Grant GAP15-07908S.

This article is part of the Topical Collection on Optical Wave and Waveguide Theory and Numerical Modelling, OQTNM 2017.

Guest Edited by Bastiaan Pieter de Hon, Sander Johannes Floris, Manfred Hammer, Dirk Schulz, Anne-Laure Fehrembach.

✉ Pavel Honzatko
honzatko@ufe.cz

Martin Vanek
vanek@ufe.cz

Jiri Ctyroky
ctyroky@ufe.cz

[1] Institute of Photonics and Electronics, CAS, Chaberska 57, 182 51 Prague, Czech Republic

1 Introduction

In this paper we investigate leaky-mode resonant diffraction gratings (LMRG) used as a wavelength- and polarization-selective element in fibre lasers. Resonant leaky-mode diffraction gratings are phase-matching gratings allowing us to excite and simultaneously extract a guided mode of the adjacent waveguide. Their zero-order diffraction efficiency can be close to 100% in reflection. Leaky-wave resonance was recognized in some of Wood's diffraction anomalies by Hessel and Oliner (1965). Neviére et al. theoretically studied these anomalies in dielectric gratings combined with waveguides and related them to the existence of waveguide modes (Neviere et al. 1973). In 1985, Mashev and Popov experimentally demonstrated a resonance anomaly in the reflected zero diffraction order caused by the excitation of guided waves in a corrugated waveguide, which significantly increased the reflectance of the structure in a narrow wavelength band (Mashev and Popov 1985). Diffraction of a monochromatic plane wave by a surface-corrugated waveguide and by a substrate-corrugated waveguide was studied by Golubenko et al. (1985). A multiple interference model related to an intuitive ray picture and a second-order perturbation approach with a Green's function formulation were developed for thin dielectric waveguides by Sharon et al. (1997).

LMRGs were used as wavelength-selective elements in erbium-doped ZBLAN fluoride fibres operating in a spectral range of 2700–2900 nm (Johnson et al. 2012), in erbium-doped silica fibre laser at a wavelength of 1541 nm (Mehta et al. 2007), and in thulium-doped silica fibre lasers at a wavelength of about 2000 nm (Sims et al. 2011). A collimating optics was used in all these laser experiments in order to couple light from the optical fibre to the LMRG. Any of such intracavity elements negatively influences the threshold, slope efficiency, reliability and cost of high-power fibre lasers. It is therefore tempting to fabricate the LMRG directly on cleaved or polished fibre facets. Several technologies were examined for micromachining of fibre facets such as interference lithography (Yang et al. 2012), photolithography (Johnson et al. 2003), electron-beam lithography (Prasciolu et al. 2003), focused ion-beam milling (Schiappelli et al. 2004; Vanek et al. 2016), stamping (Sanghera et al. 2010; MacLeod et al. 2011), nano-imprint technology (Kostovski et al. 2009; Kanamori et al. 2013), two-photon polymerization 3D printing (Williams et al. 2011; Gissibl et al. 2016a, b), direct laser writing (Kowalczyk et al. 2014).

Here we report on a leaky-mode resonant diffraction grating that is intended to be employed as a high-reflectance, wavelength- and polarization-dependent mirror in a fibre laser. The grating is supposed to be milled into an oxide layer with high refractive index deposited on the fibre facet. The design of the diffraction grating is described in Sect. 2, optimization of the grating in Sect. 3, tolerance analysis in Sect. 4.

2 Leaky-mode resonant grating design

We design the LMRG for a specific use in high-power, thulium-doped fibre lasers such as shown in Fig. 1a. The resonator of the laser consists of a large mode area, double-clad, polarization maintaining thulium-doped fibre (PLMA-TDF), pump-signal combiner (PSC), and two mirrors. Laser diodes with multimode pigtails are used for pumping the double-clad active fibre over the PSC. The low-reflectance mirror is formed by a perpendicularly cleaved output fibre of which the reflectance is 3.5% in accordance with Fresnel equations.

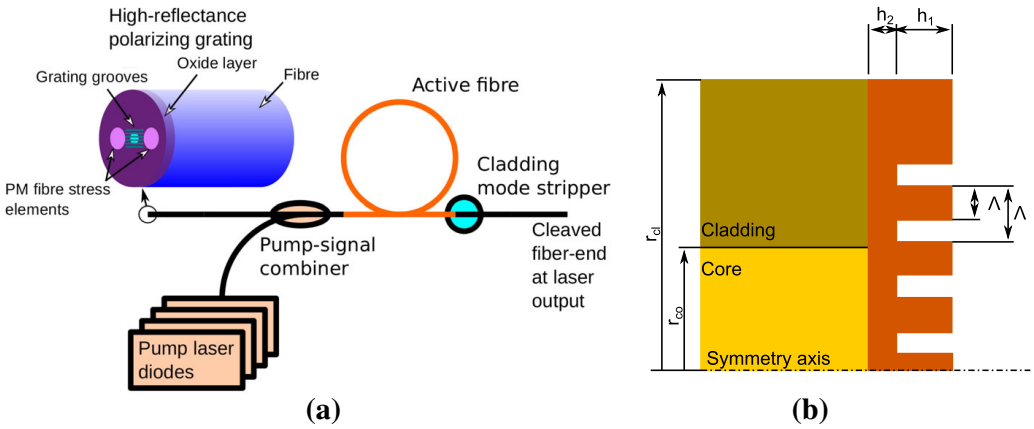

Fig. 1 **a** Idea of LMRG application in a laser setup. **b** Optical fibre with resonant diffraction grating

The high-reflectance wavelength- and polarization-selective mirror is fabricated on the perpendicularly cleaved pigtail of the PSC in the form of an LMRG. We design the high-reflectance mirror so that it will have a resonance wavelength of 2000 nm, modal reflectance close to 100%, high polarization extinction ratio, and reasonably narrow bandwidth.

The fibre with the LMRG is shown in Fig. 1b. The single mode fibre has a core with radius r_{co} and refractive index n_{co}, cladding with radius r_{cl} and refractive index n_{cl}. An oxide layer with high refractive index n_{ox} and thickness h is deposited on the fibre facet. Finally, grating grooves with depth h_1 are etched into the deposited layer. The subwavelength grating has period Λ and fill factor f. Throughout the paper, we assume parameters shown in Table 1. We neglect dielectric losses by setting extinction coefficients to zero.

Since the corrugated high-index layer is surrounded from both sides with lower-index media, it can be considered as a double-layer planar waveguide: a homogeneous layer with the thickness h_2, and a "segmented" layer with the thickness h_1 and with somewhat lower polarization dependent refractive index according to the effective-medium theory (Lalanne and Hugonin 1998). This bi-layer can be thus considered as a planar leaky-wave waveguide perpendicular to the fibre. Light incident from the fibre is coupled in the 1-st diffraction orders of the grating into the waveguide in opposite directions. Light guided in the waveguide is back-reflected in the 2-nd diffraction orders of the grating and partially coupled out of the guiding layer in the 1-st diffraction orders. By proper adjustment of grating parameters the transmitted zeroth order can be suppressed by the destructive interference with the light coupled out of the guiding layer while the back-reflected zeroth order light is enhanced by constructive interference with the light coupled out of the layer in the backward direction. As a result, high spectrally selective back-reflection is achieved (Neviere et al. 1973; Golubenko et al. 1985).

Because of relatively high refractive index contrast of the structure, deep etch and only weakly subwavelength character of the grating, application of "rigorous" full-wave numerical modelling methods is required for the proper design of the grating.

Table 1 Refractive indices and core radius used in the calculations

n_{co}	1.4428	n_{cl}	1.44	n_{ox}	1.906	r_{co}	12.5 μm

The resonant wavelengths differ for TE and TM modes. We design the LMRG so that only TE mode resonance falls in the gain band of thulium-doped fibre. High extinction ratio of TE to TM polarization will allow laser operation with defined wavelength and polarization.

3 Leaky-mode resonance simulation

The finite-difference time-domain (FDTD) method is used to design and optimise the LMRG. We simulate propagation of a short optical pulse with finite bandwidth centred at a specific wavelength in the fibre using the open-source computer software MEEP (Oskooi et al. 2010). Only the fundamental fibre mode is excited in simulations. The pulse excites the leaky-mode resonance in the microstructure fabricated on the fibre facet. It should be noted that we analyse the excitation of the leaky mode by a short optical pulse just for convenience. The laser shown in Fig. 1a is assumed to operate in CW mode.

We calculate the transmission and reflection spectra by taking harmonic transforms of the time-domain fluxes through the measurement planes F_{g1} and F_{g2} situated before and behind the LMRG (Fig. 2). The plane F_{g1} is relatively far from the LMRG so that the diffracted light that is not coupled back to the fibre core can be absorbed in the perfectly matched layers (PML) surrounding the simulated area. The flux spectrum F_{1g} recorded in the simulations is, in fact, the difference of forward F_F and reflected F_R flux spectra,

$$F_{1g} = F_F - F_R. \tag{1}$$

We use a reference model of a fibre without any grating to find the forward flux spectrum $F_F = F_{1f}$. The reflected flux spectrum is

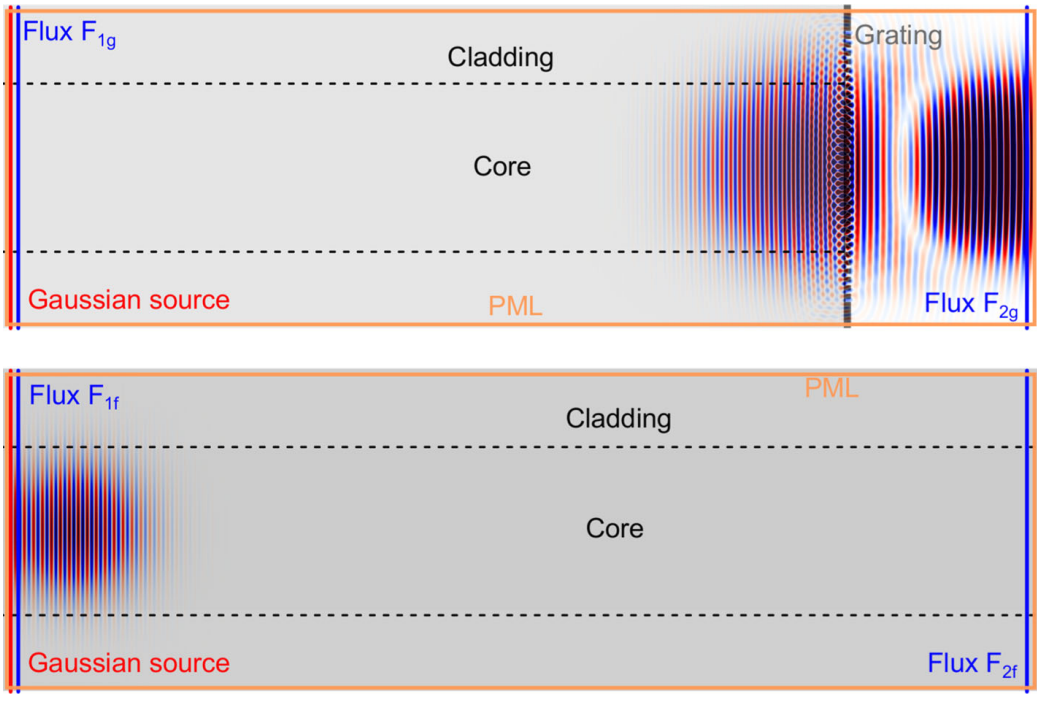

Fig. 2 Model of the fibre with LMRG (top) and reference fibre (bottom) as used in the FDTD method. Perfectly matched layers (PML), source and flux planes are shown

$$F_R = F_{1f} - F_{1g}, \tag{2}$$

and the modal reflectance R_g, transmittance T_g and loss of the LMRG L_g are calculated as

$$R_g = F_R / F_{1f}, \tag{3}$$

$$T_g = F_{2g} / F_{2f}, \tag{4}$$

$$L_g = 1 - T_g - R_g. \tag{5}$$

In order to optimize gratings with limited computational resources, we resort to 2D-FDTD method for a 1D grating on the facet of a slab waveguide with the thickness equal to the diameter of the fibre. The simulations are performed with a resolution of 30 points/μm which corresponds to 60 points per wavelength in vacuum and roughly 30 points per wavelength in high refractive index oxide layer. The simulated area is 128 μm × 50 μm with PML thickness 1.5 μm. The flux measurement planes are placed at a distance of 5 μm from the left and right border. The source has Gaussian distribution both in time and space and is placed at a distance of 4 μm from the left side of the simulated area. The modal width is estimated to be 10.8 μm FWHM by minimizing loss in the reference waveguide without any grating. We assume a truncated periodic structure with N grooves, centered on the fibre axis. The number of grooves is set to 33 if not stated otherwise. Influence of the number of grating grooves on the modal reflectance is discussed in Sect. 4

We compare the 2D simulation results with full 3D simulations performed by Fourier modal method (3D-FMM) (Čtyroký 2012) in order to justify the use of such a simplified model. Very good agreement between modal reflectances calculated with 2D and 3D models was found (Fig. 3a). The whole modal reflectance curve calculated by 3D FMM is shifted by 2.0 nm to shorter wavelength compared to the curve calculated by the 2D-FDTD method. Both reflectance curves agree within 2.0% over the whole wavelength interval 1.9–2.1 nm, when this wavelength shift is taken into account. The peak reflectances, which are important for the laser performance, differ by 1.1%. Such a small uncertainty in the reflectance peak value will be negligible in experiment taking the fabrication tolerances into account.

We also compared modal reflectances calculated by the 2D-FDTD method with those calculated by the 2D-FMM and found that they are almost undistinguishable (Fig. 3b).

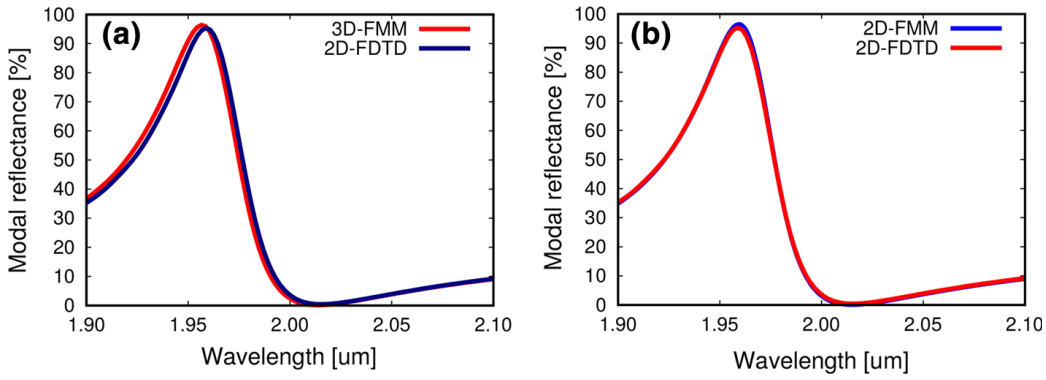

Fig. 3 **a** Modal reflectances calculated by 2D FMM and 3D FMM for LMRG with resonance at 1960 nm. **b** Modal reflectances calculated by 2D FMM and 2D FDTD method. LMRG has period $\Lambda = 1290$ nm, $f = 0.7$, $h_1 = 200$ nm and $h_2 = 710$ nm

Both reflectance curves agree within 1.8% over the whole wavelength interval 1.9–2.1 nm without any wavelength shift.

4 Leaky-mode resonant grating optimization

We maximized the peak modal reflectance at a wavelength of 2000 nm using the 2D-FDTD method by varying the grating period Λ, groove depth h_1, waveguide layer thickness h_2, and fill factor f. Figure 4 shows how the spectral shape of modal reflectance is affected by parameters of the LMRG. The period Λ determines the wavelength at which the resonant coupling between the incident wave and the guided mode occurs. Variations in the period are manifested by almost pure resonant wavelength shifts. The groove depth variation h_1 is related to the coupling strength. A substantial groove depth is necessary to achieve modal reflectances close to 100%. When close to the optimum point, the groove depth influences the reflectance peak shape. The thickness of the waveguide layer h_2 has a direct impact on the guided mode. The fill factor determines the superstrate effective index and has a major impact on the properties of the waveguide as well. Variations in both these parameters have strong influence on the resonance wavelength and peak modal reflectance. Figure 5 shows effects which the fill factor has on the modal reflectance peak height, wavelength, and width. The modal reflectance reaches a maximum value of 96% for a fill factor of 0.62. The full width at half maximum (FWHM) of the modal reflectance peak decreases with increasing fill factor, while the resonance wavelength increases. Further, the influence of the number of grating grooves on the peak modal reflectance is shown in

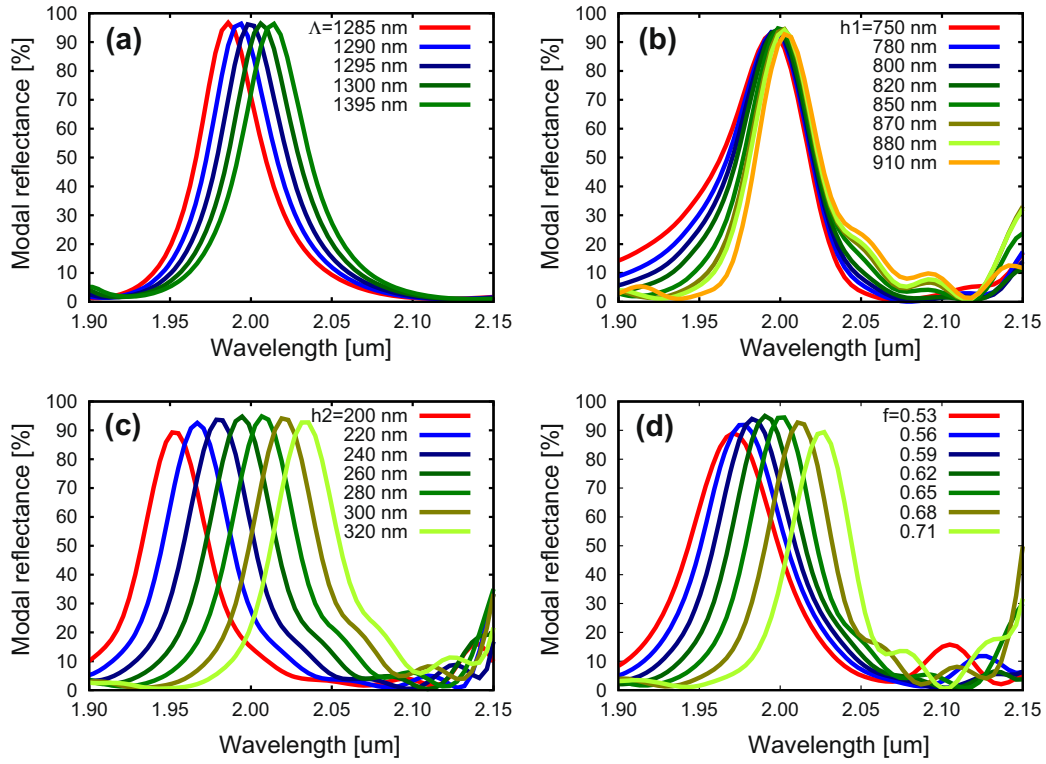

Fig. 4 Dependence of the spectral shape of modal reflectivity on **a** grating period Λ, **b** grating groove depth h_1, **c** guiding layer thickness h_2, **d** grating fill factor f

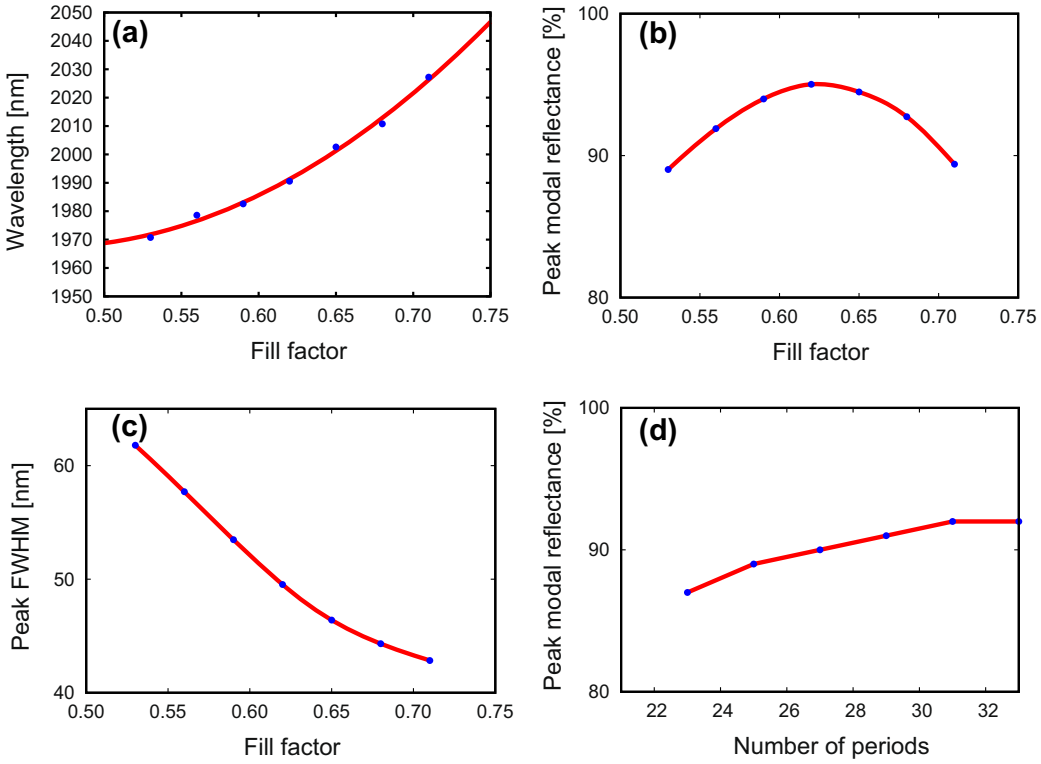

Fig. 5 Dependence of the modal reflectance peak **a** wavelength, **b** height, **c** width on the fill factor f. **d** Dependence of the peak modal reflectance on the number of grooves of the truncated grating

Fig. 5d. It shows that the grating size should be much larger than the fibre core diameter, at least 40 μm × 40 μm for a fibre with a 25-μm core diameter. The optimum parameters are summarised in the Table 2. The modal reflectance reaches a value of 96% for TE mode, while it remains as low as 1.6% for TM mode. The polarization extinction ratio achieves a value of 17.8 dB.

5 Fabrication tolerance analysis

In the previous section we focused on the search for optimum LMRG parameters. We also showed how the modal reflectance is influenced by deviations of various parameters from their optimum values. Now we will examine imperfections that may arise in diffraction gratings made by the FIB technique. We assume that the groove depth and fill factor have the normal distribution about their mean values with standard deviation σ. Ten realizations of the LMRG with random groove depths and constant fill factor were generated for each standard deviation shown in Fig. 6a. The spectral dependence of modal reflectance was

Table 2 Optimum parameters of the LMRG

Λ (nm)	1295	h_1 (nm)	860	h_2 (nm)	270	f	0.62

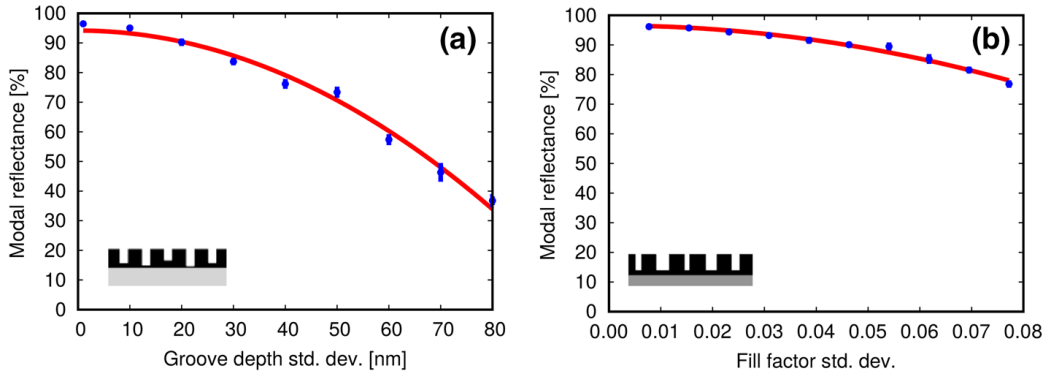

Fig. 6 Effects of the **a** groove depth h_1 and **b** fill factor f variance on the modal reflectance peak

calculated for each of these random gratings by the 2D-FDTD method. The same process was repeated with random fill factors and constant groove depth. Averaged peak modal reflectances are shown together with error bars in Fig. 6 for various standard deviations of corresponding parameters. We can conclude that standard deviations of the fill factor equal to 0.075, or of groove depth equal to 38 nm cause a decrease in the modal reflectance from 96 to 80%. The peak modal reflectance is expected to be 64% when both parameters change randomly with such standard deviations. We analysed also influence of rounded upper edges and trapezoidal shape of the grating grooves on the modal reflectance. We found these imperfections to be far less important compared to the groove depth and fill factor. These results should be taken into account when selecting the FIB milling parameters.

6 Conclusions

High-reflectance polarization-sensitive wavelength filters based on leaky-mode resonant gratings designed for the fabrication on the facet of optical fibres were numerically investigated. Such structures can be milled by focused ion beam in a high-refractive-index layer deposited on the fibre facet. In simulations, we used the 2D FDTD method, 2D FMM and 3D FMM. All these methods yielded almost identical results. We predicted that a modal reflectance peak height of 96% and bandwidth of about 50 nm for gratings centred at 2000 nm can be obtained for an optimised leaky-mode resonant diffraction grating fabricated in a tantala layer. The polarization extinction ratio of 17.8 dB is sufficiently high to maintain the well-defined linear polarization of the laser. It was found that the grating size should be larger than 40 μm × 40 μm for a fibre core diameter of 25 μm to get such high reflectance. We analysed the influence of systematic errors in the layer thickness, grating fill factor, and groove depth. Examination of the effects of the variance of the fill factor and groove depth on the modal reflectance was also carried out. Based on this analysis we can conclude that the fabrication of such leaky-mode gratings is feasible. Experimental work is under way, however it is beyond the scope of the present paper.

Acknowledgements The authors gratefully acknowledge support from the Czech Science Foundation under Grant No. GAP15-07908S. They also thank to Ardavan F. Oskooi, David Roundy, Mihai Ibanescu, Peter Bermel, J. D. Joannopoulos, and Steven G. Johnson for copylefting the Meep software under the GNU General Public Licence.

References

Čtyroký, J.: 3-D bidirectional propagation algorithm based on Fourier series. J. Lightwave Technol. **30**(23), 3699–3708 (2012). https://jlt.osa.org/abstract.cfm?URI=jlt-30-23-3699

Gissibl, T., Schmid, M., Giessen, H.: Spatial beam intensity shaping using phase masks on single-mode optical fibers fabricated by femtosecond direct laser writing. Optica **3**(4), 448–451 (2016a). https://doi.org/10.1364/OPTICA.3.000448

Gissibl, T., Thiele, S., Herkommer, A., Giessen, H.: Sub-micrometre accurate free-form optics by three-dimensional printing on single-mode fibres. Nat. Commun. **7**, 11763, 1–9 (2016b). https://doi.org/10.1038/ncomms11763

Golubenko, G.A., Svakhin, A.S., Sychugov, V.A., Tishchenko, A.V.: Total reflection of light from a corrugated surface of a dielectric waveguide. Sov. J. Quant. Electron. **15**(7), 886–887 (1985). http://stacks.iop.org/0049-1748/15/i=7/a=L02

Hessel, A., Oliner, A.A.: A new theory of wood's anomalies on optical gratings. Appl. Opt. **4**(10), 1275–1297 (1965). https://doi.org/10.1364/AO.4.001275

Johnson, E.G., Stack, J., Suleski, T.J., Koehler, C., Delaney, W.: Fabrication of micro optics on coreless fiber segments. Appl. Opt. **42**(5), 785–791 (2003). https://doi.org/10.1364/AO.42.000785

Johnson, E.G., Li, Y., Woodward, R., Poutous, M., Raghu, I., Shori, R.: Guided mode resonance filter as wavelength selecting element in er: ZBLAN fiber laser. In: Advanced Photonics Congress, Optical Society of America, p STu3F.1 (2012). https://doi.org/10.1364/SOF.2012.STu3F.1

Kanamori, Y., Okochi, M., Hane, K.: Fabrication of antireflection subwavelength gratings at the tips of optical fibers using UV nanoimprint lithography. Opt. Express **21**(1), 322–328 (2013). https://doi.org/10.1364/OE.21.000322

Kostovski, G., White, D., Mitchell, A., Austin, M., Stoddart, P.: Nanoimprinted optical fibres: Biotemplated nanostructures for SERS sensing. Biosensors and Bioelectronics **24**(5), 1531–1535 (2009). https://doi.org/10.1016/j.bios.2008.10.016. (selected Papers from the Tenth World Congress on Biosensors Shangai, China, May 14–16, 2008)

Kowalczyk, M., Haberko, J., Wasylczyk, P.: Microstructured gradient-index antireflective coating fabricated on a fiber tip with direct laser writing. Opt. Express **22**(10), 12545–12550 (2014). https://doi.org/10.1364/OE.22.012545

Lalanne, P., Hugonin, J.P.: High-order effective-medium theory of subwavelength gratings in classical mounting: application to volume holograms. J. Opt. Soc. Am. A **15**(7), 1843–1851 (1998). https://doi.org/10.1364/JOSAA.15.001843

MacLeod, B.D., Hobbs, D.S., Sabatino III, E.: Moldable AR microstructures for improved laser transmission and damage resistance in CIRCM fiber optic beam delivery systems. **8016**, 80160Q, 1–14 (2011). https://doi.org/10.1117/12.883281

Mashev, L., Popov, E.: Zero order anomaly of dielectric coated gratings. Opt. Commun. **55**(6), 377–380 (1985). https://doi.org/10.1016/0030-4018(85)90134-8

Mehta, A.A., Rumpf, R.C., Roth, Z.A., Johnson, E.G.: Guided mode resonance filter as a spectrally selective feedback element in a double-cladding optical fiber laser. IEEE Photonics Technol. Lett. **19**(24), 2030–2032 (2007)

Neviere, M., Petit, R., Cadilhac, M.: About the theory of optical grating coupler-waveguide systems. Opt. Commun. **8**(2), 113–117 (1973). https://doi.org/10.1016/0030-4018(73)90150-8

Oskooi, A.F., Roundy, D., Ibanescu, M., Bermel, P., Joannopoulos, J.D., Johnson, S.G.: MEEP: a flexible free-software package for electromagnetic simulations by the FDTD method. Comput. Phys. Commun. **181**, 687–702 (2010). https://doi.org/10.1016/j.cpc.2009.11.008

Prasciolu, M., Cojoc, D., Cabrini, S., Businaro, L., Candeloro, P., Tormen, M., Kumar, R., Liberale, C., Degiorgio, V., Gerardino, A., Gigli, G., Pisignano, D., Fabrizio, E.D., Cingolani, R.: Design and fabrication of on-fiber diffractive elements for fiber-waveguide coupling by means of e-beam lithography. Microelectron. Eng. **67–68**, 169–174 (2003). https://doi.org/10.1016/S0167-9317(03)00068-6. (proceedings of the 28th International Conference on Micro- and Nano-Engineering)

Sanghera, J., Florea, C., Busse, L., Shaw, B., Miklos, F., Aggarwal, I.: Reduced fresnel losses in chalcogenide fibers by using anti-reflective surface structures on fiber end faces. Opt. Express **18**(25), 26760–26768 (2010). https://doi.org/10.1364/OE.18.026760

Schiappelli, F., Kumar, R., Prasciolu, M., Cojoc, D., Cabrini, S., Vittorio, M.D., Visimberga, G., Gerardino, A., Degiorgio, V., Fabrizio, E.D.: Efficient fiber-to-waveguide coupling by a lens on the end of the optical fiber fabricated by focused ion beam milling. Microelectron Eng. **73–74**, 397–404 (2004). https://doi.org/10.1016/j.mee.2004.02.077. (micro and Nano Engineering 2003)

Sharon, A., Rosenblatt, D., Friesem, A.A.: Resonant grating-waveguide structures for visible and near-infrared radiation. J. Opt. Soc. Am. A **14**(11), 2985–2993 (1997). https://doi.org/10.1364/JOSAA.14.002985

Sims, R.A., Roth, Z.A., Willis, C.C.C., Kadwani, P., McComb, T.S., Shah, L., Sudesh, V., Poutous, M., Johnson, E.G., Richardson, M.: Spectral narrowing and stabilization of thulium fiber lasers using guided-mode resonance filters. Opt. Lett. **36**(5), 737–739 (2011). https://doi.org/10.1364/OL.36.000737

Vanek, M., Vanis, J., Baravets, Y., Todorov, F., Ctyroky, J., Honzatko, P.: High-power fiber laser with a polarizing diffraction grating milled on the facet of an optical fiber. Opt. Express **24**(26), 30225–30233 (2016). https://doi.org/10.1364/OE.24.030225

Williams, H.E., Freppon, D.J., Kuebler, S.M., Rumpf, R.C., Melino, M.A.: Fabrication of three-dimensional micro-photonic structures on the tip of optical fibers using SU-8. Opt. Express **19**(23), 22910–22922 (2011). https://doi.org/10.1364/OE.19.022910

Yang, X., Ileri, N., Larson, C.C., Carlson, T.C., Britten, J.A., Chang, A.S.P., Gu, C., Bond, T.C.: Nanopillar array on a fiber facet for highly sensitive surface-enhanced raman scattering. Opt. Express **20**(22), 24819–24826 (2012). https://doi.org/10.1364/OE.20.024819